Justus-Liebig-Universität Gießen
I. Physikalisches Institut

Characterization of
Group III–Nitride Nanowires
for Bio–Electrochemical Sensors

Inauguraldissertation zur Erlangung des akademischen Grades eines

Doktors der Naturwissenschaften
(Doctor rerum naturalium)

vorgelegt dem Fachbereich

Mathematik und Informatik, Physik, Geographie

von

Jens Matthias Emil Wallys

angefertigt bei

Univ.-Prof. Dr. Martin Eickhoff

Zusammenfassung

Thema der vorliegenden Arbeit ist die Charakterisierung von Gruppe III–Nitrid Nanostrukturen für eine mögliche Anwendung als nanophotonische Sonden in der biochemischen Sensorik.

Konkret handelt es sich dabei um Nanodrähte (NW) bestehend aus Gallium Nitrid (GaN) bzw. Indium–Gallium Nitrid (InGaN). Die NW wurden mittels *plasma– unterstützter Molekularstrahlepitaxie* (PAMBE) auf hoch leitfähigen Silizium(111) Substraten in einem selbstassemblierten Wachstumsprozess hergestellt.

Die elektrochemische Charakterisierung der NW wurde mittels Impedanzspektroskopie und zyklischer Voltammetrie durchgeführt. In allen Experimenten, die im Elektrolyten durchgeführt wurden, war die NW–Probe in einer Drei–Elektroden– Konfiguration als Arbeitselektrode beschaltet. Als Standardelektrolyt diente eine physiologische Salzlösung (10 mM PBS). Die Extraktion der elektrochemischen Grenzflächenparameter Oberflächenwiderstand R_S und Oberflächenkapazität C_S wurde durch den Vergleich mit *elektrischen Ersatzschaltbildern* (EEC) möglich.

In einem weiteren Schritt wurden die n.i.d. NW mit NW, die mit Silizium bzw. Magnesium dotiert waren, verglichen. Dabei zeigte sich, dass die Dotierung mit Silizium eine Erhöhung der Oberflächenkapazität C_S um mehr als eine Größenordnung bewirkt, während der Wert für R_S kontinuierlich absinkt.

Die Dotierung mit Magnesium führte lediglich zu einer geringen Erhöhung des Oberflächenwiderstands kombiniert mit einer minimalen Verringerung der Oberflächenkapazität. Aus dem beobachteten Verhalten konnte der Übergang zur vollständigen p–typ Leitung im ND ausgeschlossen werden. Messungen der offenen Klemmspannung hingegen zeigten, dass es vor allem bei NW mit hoher Magnesium– Konzentration ([Mg] > 10^{20} cm^{-3}) zur Ausbildung von Bereichen kommt, die p–typ charakteristisches Verhalten aufweisen.

Eine Unterteilung der NW gemäß ihrer elektrochemischen Parameter (C_S, R_S) erfolgt in zwei Gruppen: Die erste Gruppe, als "conductive" bezeichnet, zeichnet sich durch einen großen Wert C_S (> 10^{-5} F cm^{-2}) und einen niedrigen Wert R_S (< 10^{-7} Ω cm^2) aus. Die zweite Gruppe, welche als "resistive" bezeichnet wird, wird

repräsentiert von erniedrigten Werten für C_S und erhöhten Werten für R_S.

Physikalisch bedeutet dies, dass die NW der "resitive" Gruppe komplett von freien Ladungsträgern verarmt sind. Die von den Oberflächenzuständen hervorgerufene Raumladungszone schließt in diesem Fall das komplette Drahtvolumen ein. In NWs der Gruppe "conductive" findet sich im Zentrum ein Bereich, in dem Leitungs– und Valenzband ihr Bulkniveau erreichen. Dieser Bereich (leitender Kanal) ist feldfrei und bewirkt, dass größere Volumina des NW zur Bildung der Oberflächenkapazität beitragen. Dieser Effekt kann entweder durch eine Erhöhung der n–Typ Dotierung oder durch eine Vergrößerung des NW–Durchmessers erreicht werden. In beiden Gruppen von NW ist zudem aufgrund der inhomogenen Dotierkonzentration und der lateralen Aufweitung der Drähte von einem sich axial verändernden Bandprofil auszugehen.

Das präsentierte Modell wurde durch die Messung des Ladungstransfers in das Redoxpaar (Fe^{2+}/Fe^{3+}) mittel zyklischer Voltammetrie, welcher nur bei NW aus der Gruppe "conductive" beobachtet werden konnte, unterstützt.

Eine weitere Bestätigung der Bandprofilinterpretation wurde durch Anlegen einer externen Spannung und deren Einfluss auf die elektrochemischen Parameter erreicht. Es zeigte sich, dass für alle untersuchten NW der "resistive" Gruppe eine Erhöhung von C_S und eine Verringerung von R_S durch Anlegen einer kathodischen Spannung erreicht werden konnte. Beides ist mit einer Verkleinerung der Raumladungszone durch die Spannung zu erklären. An der NW Probe mit der höchsten Silizium–Konzentration konnte bei Anlegen einer anodischen Spannung der umgekehrte Effekt, nämlich eine Verringerung von C_S und einer Erhöhung von R_S, gezeigt werden.

Des Weiteren wurde die Photolumineszenz (PL) der Nanodrähte im Elektrolyten bei Raumtemperatur untersucht. Dabei zeigte sich, dass die Intensität der von den NW herrührenden PL auf extern angelegte Spannungen und den pH–Wert des Elektrolyten reagiert, wobei die energetische Position und die Halbwertsbreite (FWHM) konstant blieben. Eine Erhöhung des an den NW vorliegenden Potenzials in kathodischer Polarität führte zu einer Erhöhung der PL–Intensität bei konstantem pH. Durch das Absenken des pH Wertes in den sauren Bereich bei konstant gehaltener Spannung wurde ebenfalls eine Erhöhung der Intensität erreicht. Es zeigte sich, dass die offene Klemmspannung unter Beleuchtung ein Referenzpotenzial für die stabile PL–Detektion darstellt.

Die Spannungs– und pH–Abhängigkeit der PL–Intensität wurde auf Grundlage des in der Literatur bekannten "Dead Layer Models" für Schichten beschrieben.

Dabei wurde die PL–Intensität als Verhältnis zwischen strahlender Rekombination im Bulk und nicht strahlender Rekombination an der Oberfläche bezeichnet. Das Anlegen einer kathodischen Spannung führt zu einer Verringerung der Oberflächenbandverbiegung und erhöht damit die strahlende Rekombinationsrate. Um das Modell an die veränderten Bedingungen bei den im Rahmen dieser Arbeit untersuchten NW anzupassen, wurde eine sich entlang der NW Wachstumsachse verändernde Oberflächenbandverbiegung in Form einer sich exponentiell verringernden Flachbandspannung U_{fb}, berücksichtigt. Durch die Erweiterungen des Modells konnten die Messdaten deutlich besser wiedergegeben werden. Die in diesem Rahmen ebenfalls untersuchten Auswirkungen der Siliziumdotierung auf die PL können als Folge des Models mittels einer insgesamt kleineren Breite der Raumladungszone verstanden werden.

Einer der vorgeschlagenen Mechanismen für nicht strahlende Rekombination, der Grenzflächentransfer eines photogenerierten Loches in das Redoxpaar $OH^-/OH\cdot$ des Wassers, wurde in weiteren PL–Messungen in einer ionischen Flüssigkeit blockiert und somit indirekt bestätigt.

Als Ausblick wurden die Auswirkungen der Magnesiumdotierung auf die PL Eigenschaften untersucht. Dabei zeigte sich prinzipiell ähnliches Verhalten der PL auf Änderung der Spannung bzw. des pH–Wertes. Eine zusätzliche, von der Mg–Konzentration abhängige, zweite Lumineszenz konnte einer *Donator Akzeptor Paar Rekombination* (DAP) zugeschrieben werden, die wie die Bandkantenemission des GaN auf Spannungs– und pH–Änderungen reagiert. Das Verhältnis der beiden Emissionsintensitäten hängt dabei stark vom lokalen NW–Durchmesser ab.

Aufbauend auf den Ergebnissen zur pH–abhängigen PL–Intensität von GaN NW wird in dieser Arbeit ein mögliches Sensorkonzept vorgestellt. Hierzu wurde aus den Spannungs– und pH–abhängigen Messungen eine *optische Transkonduktanz* ermittelt, welche die Definition eines Sensorarbeitspunktes in Abhängigkeit des zu erwartenden pH–Intervalls erlaubt. Außerdem wurden die Wiederholbarkeit, die Ansprechzeit sowie die Sensitivität einer möglichen Anwendung als optischer Signalwandler zur pH–Ermittlung untersucht.

In zwei die prinzipielle Funktion prüfenden Untersuchungen "proof of principle" wird die Detektion einer pH–Änderung, hervorgerufen durch enzymatisch umgewandeltes Penicillin–G in Penicillinsäure und deren anschließende Dissoziation, mittels GaN und InGaN/GaN NW vorgestellt.

Contents

Contents

Introduction

In the presented work the electrochemical and photoelectrochemical properties of Gallium Nitride nanowires with respect to possible sensor applications were investigated. In particular the material Gallium Nitride as representative of the group III–nitrides is characterized by chemical inertness. Nanowires are one example for the group of novel nanostructures which gained significant interest during the last decades. Several sources proclaim that nanotechnology, which deals with structures with sizes in the nm regime, is one of the most promising technologies of our century [1].

So far many basic properties of nanostructures in general and nanowires in particular remain unclear, even if specific enhancing factors of such structures e.g. large surface to volume ratio, are exploited in various fields. Kikuchi et al. [2] presented device structures based on nanowires for optoelectronics and light emitters. Although the presented efficiency was very low the optimization potential is believed to be very high. Additionally, great improvements could be reached in nanoelectronics [3] and in the field of photoelectrochemical water–splitting [4], where due to the high surface to volume ratio GaN NWs have been found to show superior performance compared to thin films or submicron dot arrays [5, 6]. Especially the large surface to volume ratio is beneficial for all surface related processes which are of great importance in sensor applications like bio–chemical sensors [7, 8] or, in combination with an optical readout as transducers for gaseous detection [9].

Historically, the growth of semiconductor nanowires goes back to the first reports of freestanding semiconductor nanostructures in 1964 by Wagner and Ellis [10], who reported the growth of silicon nanowires by the *vapor–liquid–solid* (VLS) method with gold seeds as catalyst. Almost 30 years later the group of Calleja et al. [11, 12, 13] established the growth of Gallium Nitride nanowires by *molecular beam epitaxy* (MBE) in a self–assembled process under Nitrogen–rich conditions without any additional catalyst. These nanowires grow fully relaxed [14] and exhibit the same lattice parameters (a, c) as bulk Gallium Nitride crystals [15]. Additionally, the nanowires grow with a high crystalline quality which means that the density of structural defects is very low. This makes them an ideal model system to study the

effect of size reduction on the basic material properties.

The presented thesis focuses on three central issues:

- The electrochemical examination of GaN NWs by impedance spectroscopy and cyclic voltammetry and the subsequent characterization with respect to the extracted electrical parameters according to electrical equivalent circuits

- The photoelectrochemical examination of the photoluminescence response of GaN and InGaN/GaN NWs under controlled bias and pH conditions

- Experiments demonstrating the capability of detecting an enzymatic induced pH change with the three electrode configuration proposed here with the NW ensemble as an optical transducer

A review of the prerequisite theoretical background for the semiconductor GaN NWs with a focus on the band structure description and the electrolyte is provided in chapter 2. At the end of the chapter, ionic liquids as alternative electrolyte are introduced.

At first, in chapter 3 the growth and structural properties of the investigated GaN NWs are introduced before in the main part the specifically designed experimental setups for electrochemical and photoelectrochemical analysis as well as the used characterization techniques are presented and discussed.

In chapter 4, the results of the electrochemical characterization of the GaN NWs are presented and compared to the Si substrate. A model that explains the relation of the electrical parameters to the band structure within the nanowires is presented and discussed in terms of doping and NW diameter.

Chapter 5 deals with the detailed photoelectrochemical characterization of the GaN nanowires. The "dead layer" model for semiconductors is presented and extended for the application to the NW geometry. Further experiments that confirm the "extended dead layer" model are realized in the form of doping–dependent optical measurements and with water–free ionic liquids as electrolyte.

In chapter 6, the mechanism of a bias– and pH–dependent photoluminescence is further discussed in terms of a possible application as pH sensor. Therefore, the sensing mechanism is examined with respect to reproducibility, response time and maximum achievable sensitivity. Finally first detections of an enzymatically produced pH change using the here presented GaN and InGaN/GaN NWs are presented.

Physical Chemistry at the Gallium Nitride/Electrolyte Interface

The systematic analysis of the solid / liquid interface started with Hermann von Helmholtz at the end of the 19. century. He introduced a simple capacitor model for the electrical double–layer forming between the solid surface and the adjacent electrolyte [16]. In the following years Louis Georges Gouy and David Chapman found a diffuse layer of charge present on the electrolyte side of the interface [16]. In 1924, both of these approaches were unified into the Gouy–Chapman–Stern model by Otto Stern [17].

The first part of this chapter (2.1) deals with the semiconductor side of the interface represented by the semiconductor Gallium Nitride. The basic electrical properties of the semiconductor surface will be reviewed briefly in terms of the corresponding band profiles. Also, the optical examination method of photoluminescence spectroscopy is introduced. Special emphasis is put on the luminescence properties of Gallium Nitride in general and on the luminescence of GaN nanowires in particular.

In the second part of this chapter (2.2) the electrolyte consisting of ions and water molecules will be discussed [16, 18]. Also, the special issue of non–aqueous electrolytes will be discussed as possible substitution to water–based electrolytes.

In the final part of this chapter (2.3), the actual interface region with the potential distribution across the semiconductor and adjacent electrolyte is discussed. Special emphasis is put on the influence on the band profile related to an externally applied bias or pH changes. In this context the effects of surface states and specific adsorbates on the potential distribution and charge transfer are discussed.

2.1. Material Properties of Gallium Nitride Nanowires

The semiconductor *Gallium Nitride* (GaN) and the *Gallium Nitride Nanowires* (GaN NWs) crystalize in the hexagonal wurtzite structure [19]. The differences in electronegativity of the Ga–atom (1.6 eV) [19] and N–atom (3.0 eV) [19] in combination with the specific lattice structure lead to a resulting dipole moment in the direction of the c–axis [0001]. As a result of the remaining polarization–induced electrical

charges, strong electric fields are present along the c–axis. These electric fields are of special interest in the context of heterostructures like quantum wells [20, 21], quantum discs [9, 22] or quantum dots [23, 24] but have no impact on the experiments of this work and consequently will not be further addressed here.

2.1.1. Band Structure

The band structure of GaN has been discussed in various textbooks [25, 26]. In the following, a brief review of some fundamental aspects essential for the subsequent discussion is presented. The shape and evolution of the band profile is identified as a determining parameter for the electrical and optical properties of the GaN NWs which will be discussed in the results of chapter 4 and 5.

In the ideal case of an intrinsic semiconductor at T = 0 K all states in the *valence band* (VB) are filled and all states in the *conduction band* (CB) are empty. For GaN the band gap has the value of E_g = 3.41 eV [27]. In this case depicted in Figure 2.1 (ii), the *Fermi energy* (E_F) is at mid–gap. ϕ is the work function and χ the electron affinity. The influence of doping on the band profile is also illustrated in Figure 2.1 for a p–type (i) and a n–type (iii) semiconductor. Due to the presence of donors and acceptors at the respective energy levels E_D and E_A the position of E_F is altered. At T = 0 K these states are not ionized. For elevated temperatures the *Fermi–Dirac distribution* leads to a population of empty states and the ionization of dopants.

The surface of any semiconductor is characterized by the abrupt breaking of lattice symmetry resulting in additional electronic states called *surface states*. These states originate from *dangling bonds* of unfilled valencies of surface atoms, structural defects, or the formation of an oxide layer [28]. Their energy levels generally have a broad distribution on the energetic scale. Of special interest are the surface states that are located in the forbidden energy gap. In an equilibrated state these energetic levels are occupied by majority carriers up to E_F. These states are indicated in Figure 2.1 (iv) and (v).

As a consequence, the band profile at the surface differers significantly from the band profile in the bulk. In case of n–type (v) (p–type (iv)) doping an upward (downward) *surface band bending* (SBB) is the result of majority charge carrier depletion in the vicinity of the surface. This so–called *space charge region* (SCR) with a spacial extension denoted by W_{SCR} is formed due to the filling of surface states up to E_F. The charge separation into majority carriers in surface states and the remaining ionized dopant atoms causes an electric field in this region. The electric field strength in the SCR can amount to values ($> 10^3$ Vcm^{-1}), implying an effective
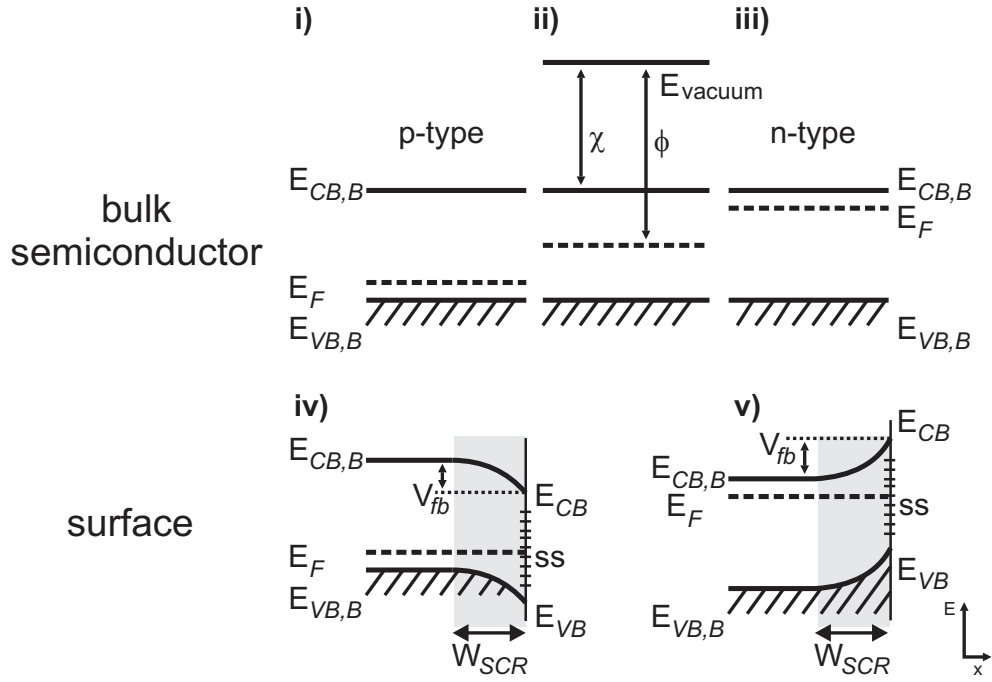
Figure 2.1.: Upper part: Energy levels in the bulk of an undoped semiconductor (ii) a p–type semiconductor (i) and a n–type semiconductor (iii); Lower part: Band bending at the surface of a p–type semiconductor (iv) and a n–type semiconductor (v).

barrier for electrons (holes) to reach the surface of a n–type (p–type) semiconductor. The width of the SCR can be calculated according to [19]

$$W_{SCR} = \sqrt{\frac{2 \cdot \varepsilon_{sc} \cdot \varepsilon_0}{e \cdot N} \cdot V_{fb}} \qquad (2.1)$$

ε_{sc} as the relative static permittivity of the semiconductor, ε_0 the electric constant of the vacuum and N the donor or acceptor impurity concentration N_D (n–type) or N_A (p–type) and V_{fb} is the *flat band* or *built–in potential*. The value of V_{fb} depends on the density and the exact energetic position of the surface states as well as the doping concentration.

Electrons in an n–type or holes in a p–type semiconductor trapped in surface states do not contribute to electric conduction inside the semiconductor [19, 29].

Going to NW geometry transforms a system from a bulk crystal with normal surface into a surface with negligible bulk. Each single NW is characteristically influenced by its SBB arising from its surface states. According to Calarco et al. [30], the diameter d of the NWs is the crucial parameter for the resulting band profile. Depending on the NW diameter, three different classifications with respect to the resulting depletion layer thickness W_{SCR} are possible.
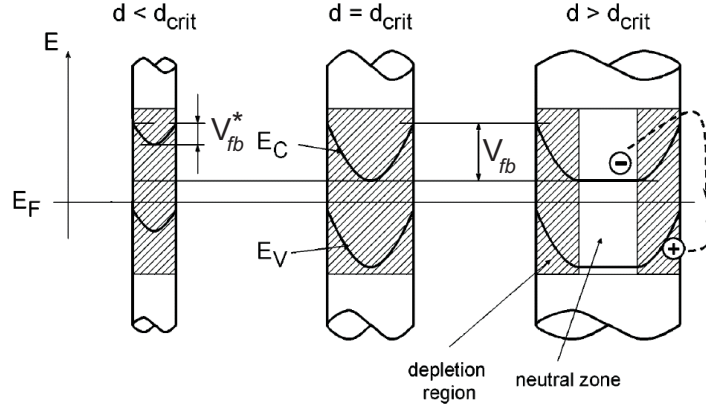
Figure 2.2.: The correlation between NW diameter and corresponding SBB according to [30].

Figure 2.2 shows the dependence of the SBB on the diameter d for three different NWs with an assumed constant n–type doping concentration. In the case of NWs with larger diameters, a "bulk–region" in the center of the nanowire exists. This channel like region extends along the growth axis. A decreasing diameter implies that less material and consequently less donors are available to achieve filling of surface states. When the NW diameter equals the critical diameter $d = d_{\mathrm{crit}}$, the wire is completely depleted with the SBB extending across the complete NW diameter. For an electron located in the center of the wire the barrier height V_{fb} in this case is similar to the one an electron experiences at the surface of a bulk crystal and can be calculated with in one dimension with Eq. 2.2.

$$V_{fb} = eN_D d_{crit}^2 / 16 \cdot \varepsilon_{sc} \cdot \varepsilon_0 \qquad for \quad d > d_{crit} \qquad (2.2)$$

Below a critical diameter d_{crit} the SBB covers the complete wire but the value of V_{fb}^* cannot reach its predicted value V_{fb}. As a consequence, the barrier height for electrons located at the center is lower in this case $V_{fb}^* < V_{fb}$.

$$V_{fb}^* = eN_D d^2 / 16 \cdot \varepsilon_{sc} \cdot \varepsilon_0 \qquad for \quad d < d_{crit} \qquad (2.3)$$

The Fermi–level pinning of bulk c–plane GaN has a value of $V_{\mathrm{fb}} \approx 0.5 - 0.6\,\mathrm{eV}$ [31]. Assuming a background n–type doing concentration of around $10^{17}\,\mathrm{cm}^{-3}$ the extension of W_{SCR} should be between 50 and 100 nm [30]. In [30] the authors extracted $d_{\mathrm{crit}} \approx 80\,\mathrm{nm}$ for n.i.d. NWs with Eq. 2.2 and 2.3.

Another way to influence the band profile of GaN is provided by doping. As doping has already demonstrated to alter the electrical properties of a GaN layer

[19] the successful doping of GaN NWs during the growth process was demonstrated for various materials e.g. Silicon [11, 14, 32], Germanium [33] or Magnesium [14, 32]. Further details how the doping of NWs affects their morphological and optical properties will be discussed in section 3.1 where NWs used in this work are presented.

2.1.2. Photoluminescence Spectroscopy

In photoluminescence measurements the light emission of a semiconductor after optical excitation is used to characterize its band and defect structure. Monochromatic light with energy E_{exc} is irradiated on the sample and after the absorption emitted at lower energies. Figure 2.3 schematically depicts the generation mechanism of electron–hole pairs that occurs within the absorption length of the semiconductor material.
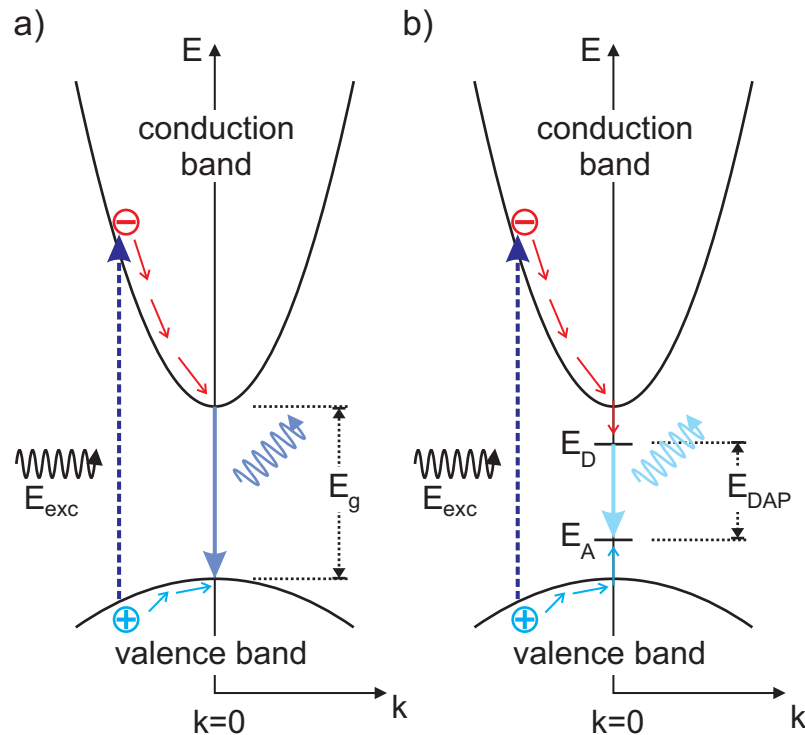
Figure 2.3.: Schematic of an electron–hole pair generation and recombination process in a) a undoped semiconductor b) a semiconductor with impurities.

By absorbtion of an incident photon an electron from the VB is elevated into the CB leaving a hole at its position in the VB. The excited electron consecutively thermalizes by interaction with phonons to the ground state at the *conduction band minimum* CBM. The excited hole also energetically moves towards the *valence band max-*

imum VBM. When they recombine they emit a photon with $E_{\mathrm{PL}} \approx E_{\mathrm{g}}$ as depicted in Figure 2.3a. This recombination at the band extrema results in the band edge recombination. In the case of GaN the *binding energy* E_{B} of the *free exciton* FX ($E_{\mathrm{B}} \approx$ 22 meV [34] or $E_{\mathrm{B}} \approx 27$ meV [35]) is of similar size than the thermal energy at room temperature (≈ 25 meV). Accordingly, several electron–hole pairs are supposed to be coupled by the coulomb interaction and form free excitons. Nevertheless, in the conducted experiments at room temperature these two different recombination lines cannot be discriminated in the Gaussian shaped PL spectrum with a full width at half maximum of ≈ 90 meV.

Figure 2.3b depicts the similar excitation process with the additional energy levels (E_{D} and E_{A}) in the band gap originating from donor and acceptor impurities. The electron at the CBM relaxes further to E_{D} and the hole to E_{A}. The recombination between this two energy level leads to the emission of a photon with lower energy $E_{\mathrm{PL}} > E_{\mathrm{FX}} > E_{\mathrm{DAP}}$ and is called a *donor–acceptor pair* (DAP) recombination.

In the case that photo–generation occurs within the SCR, the electron–hole pairs are separated by the electric field present. For n–type semiconductors the holes are attracted towards the surface while the electrons are drawn in the opposite direction (cf. Figure 2.1). Correlated to the high amount of additionally generated electron–hole pairs, additional effects on the band profile occur.
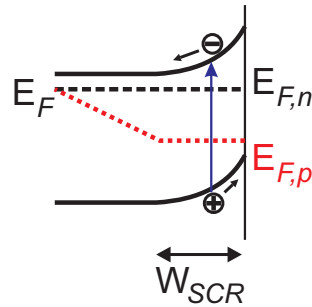
Figure 2.4.: N–type semiconductor under illumination with $E_{\mathrm{exc}} > E_{\mathrm{g}}$. The quasi Fermi level $E_{\mathrm{F,p}}$ for holes is marked red.

Figure 2.4 illustrates the effect of illumination on the band–profile of a n–type semiconductor. The photo–generated holes float toward the surface and increase the hole concentration p, while excess electrons are drawn away from the surface and do not have a significant impact on the overall electron concentration n for n–type. The result is a non–equilibrium state with $n \cdot p > \mathrm{n}_i^2$ which can be described with *quasi Fermi levels* to explain interfacial charge transfer processes not present in the dark state of the semiconductor. In the case of p–type doping the situation for holes and electron is exchanged.

In the following, other luminescence bands of GaN NWs reported in literature are discussed.

Ultra violet luminescence (UVL) & blue luminescence (BL)

These optical luminescence bands are attributed to a *donor acceptor pair recombination* (DAP) in Mg doped GaN layers. Although the hypothesis of a DAP is commonly accepted [36], the assignment of the participating donors and acceptor is controversially discussed [37, 38, 39, 38, 40, 41]. The reported emission energy varies between 2.7 and 3.3 eV with a *full width at half maximum* (FWHM) of several 100 meV. Power dependent measurements of Mg doped GaN layers revealed a blue shift of the emission energy with increasing excitation intensity [38, 40].

Furtmayr et al. [32] found evidence for this luminescence in the here examined MBE grown Mg–doped GaN NWs examined in PL measurements at 4 K. The PL spectra expressed an emission at 3.27 eV and the corresponding first and second order LO phonon replica with respective phonon energy of 92 meV [42]. This peak exhibits a red shift and significant broadening with increasing Mg content in the NW.

Yellow luminescence YL

This luminescence band in GaN layers centered at 2.2 eV [38] is attributed to structural defects. The discussion about the correct assignment to specific defects in the layers is still ongoing [43, 38, 44, 45, 46].

Furtmayr et al. [32] examined the MBE grown NWs at 4 K and found only an insignificant emission intensity for this band. These are the NWs also used in this work which are characterized by $d < 100$ nm and low density of structural defects [14, 32]. Additionally they demonstrated that doping with Si has no measurable effect on the YL while high Mg–doping ($BEP_{Mg} = 6 \cdot 10^{-10}$ mbar) increases the YL at 4 K.

Comparably, Polenta et al. [47] found a detectable YL in single MBE grown GaN NWs with a diameter ($d > 350$ nm) detached from the Si substrate. This luminescence vanishes when the diameter is reduced to a comparable value as the NWs presented in [32].

2.2. Electrolyte

After the discussion of the isolated semiconductor, the electrolyte with focus on the mainly used water–based *phosphate buffered saline solution* (PBS) is now examined. PBS is chosen because of its large application range especially as a bio–compatible buffer. Details about the buffer composition are provided in the appendix E. At the end of this section, non–aqueous electrolytes in the form of ionic liquids will be presented. Both types of electrolytes were used in this work to establish an electrical contact with the surface of the NW electrodes.

2.2.1. Ions as Charge Carriers

The liquid side of the semiconductor/electrolyte interface is represented by an electrolyte which is characterized by its solvent and the dissolved elements which are in general different salts. The solvent is selected due to its dissolving properties and its electrochemical stability. The latter is defined by the voltage range in which the solvent behaves inert. For PBS the potential window for stable operations roughly lies between 1 V and -1 V and depends on different factors, e.g. the pH value.

In contrast to a semiconductor, the dissolved ions of both polarities (e.g. Na^+ or Cl^-) act as charge carriers in an electrolyte. Because of the charge neutrality both ionic polarities exist in equal concentrations which represents another difference to a semiconductor where usually one carrier type dominates (n– or p–type). Nevertheless, theses two system can be described using the same formalisms.

The conductivity σ of a solution can be calculated according to Eq. 2.4 as sum over all participating ions

$$\sigma = F \cdot \sum_i |z_i| \cdot \mu_i \cdot c_i \tag{2.4}$$

with F being the Faraday constant, $|z_i|$ the ion charges, μ_i the mobilities and c_i the concentrations of the corresponding ion species. Typical values for the mobility of ions (e.g. Na^+ or Cl^-) in water are of the order of $\mu_i \approx 10^{-4}\,cm^2\ V^{-1}\ s^{-1}$, which is by orders of magnitude smaller then those of electrons or holes in a semiconductor (e.g. GaN $\approx 440\,cm^2\ V^{-1}\ s^{-1}$ at room temperature [48]). To compensate this differences in mobility and to obtain conductivities that are comparable to those of semiconductors, the corresponding concentration c_i of ions must be at least in the mM regime. The standard PBS electrolyte used for the experiments in this work exhibits a concentration of 10 mM.

In case of the polar solvent water, all ions are surrounded by a sheath of water molecules. Figure 2.5a and b show how a solvation sheath is structured for different ionic charge densities. Directly around the ions the so called *primary region* is located, that consists of highly ordered water dipoles. This inner sphere is loosely surrounded by a second region of partially ordered dipoles representing a smooth transition to the bulk phase of the homogeneous electrolyte. The thickness and binding strength of this solvation sheath depends on the charge density and the net charge of the solvated ion. A high charge density prominent for small ions (e.g. Na^+) results in a thick and strongly bond sheath, while a low charge density typical for larger ions (e.g. Mg^+) results in a thin and weakly bond sheath, even if the ions have the same net charge [16].

Ions can exchange electrons either among each other or with an electrode immersed into the solution. In general, an ion that captures an electron undergoes a reduction i.e. a decrease of the oxidation state (e.g. Fe^{+4}/Fe^{+3}). Complementarily, an ion that releases an electron undergoes an oxidation which is indicated by an increased oxidation state. The combination of one ion that can be oxidized with one that can be reduced is called a *redox couple* which can be described by the simple reaction scheme of Eq. 2.5

$$Red \rightleftharpoons Ox + e^-$$ (2.5)

In the following, only the one electron transfer process is discussed. Further information regarding redox reactions can be found in [16].

2.2.2. Gerischer Model

In the simple redox scheme of Eq. 2.5 the solvation sheath of the ions is neglected. In the following section, the *Gerischer model* that includes the solvation sheath of the ions participating at the redox reaction, will be presented. The model associates the different states with energy levels similarly to semiconductor terminology [49, 50, 51]. It describes the charge transfer in terms of electron exchange between empty and occupied energy states of a redox couple.

In general, four different states of solvated ions are involved in a redox process according to the Gerischer model. These are two oxidized states Ox and Ox* and two reduced states Red and Red*. The * indicates an excited state. Figure 2.5c depicts the reaction scheme of such a reaction starting with a redox couple in its reduced energy state Red. By the release of an electron the ion reaches an excited

oxidized state Ox* which represents a higher energetic position than the regular oxidized state. This energetic difference can be understood in terms of a missmatched solvation sheath that needs time to adept to the new charge density. In the subsequent reorganization of the solvation sheath the *reorganization energy* λ_{ox} is released, while the configuration of solvent molecules relaxes into the equilibrium state Ox. In the reverse process of an electron capture process the excited reduced state Red* is assumed. The equilibrium state Red is reached by release of the reorganization energy λ_{red}. For the reorganization energies the model assumes $\lambda_{red} = \lambda_{ox} = \lambda$. The reorganization time of the solvation sheath is by orders of magnitude larger than the electron transfer time. This is mathematically described by the Franck–Condon principle [51]. According to these differences in reaction time it can be assumed that the processes of electron transfer and reorganization of the solvation sheath occur sequentially.
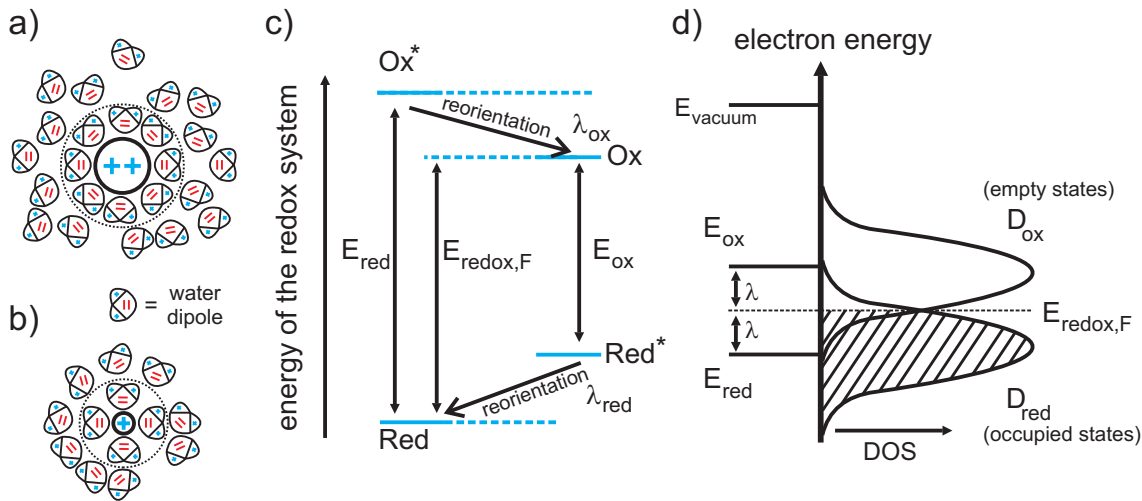

Figure 2.5.: Solvated cations characterized by different charge densities with corresponding solvation sheaths a) and b); c) Energetic reaction scheme of the electron transfer between ions; d) Gerischer diagram of a redox couple.

Part d of Figure 2.5 translates the content of Figure 2.5c into a more familiar band schema with a Gaussian distribution of reduced and oxidized states. The summation of the correlated energies for the redox cycle yields

$$E_{red} - \lambda_{ox} = E_{ox} - \lambda_{red} = E_{redox,F} \tag{2.6}$$

The electrochemical potential μ_{redox} can be calculated according to the Nernst equation (2.7)

$$\mu_{redox} = \mu_{redox}^0 + \frac{R \cdot T}{n \cdot F} \cdot ln\left(\frac{c_{ox}}{c_{red}}\right) \tag{2.7}$$

with the gas constant R, temperature T, the Faraday constant F, c_{ox} and c_{red} representing the concentrations of the oxidized and reduced species, respectively, and μ_{redox}^0 the standard chemical potential of the redox couple. The electrochemical potential described above is equivalent to the Fermi energy of the redox couple

$$\mu_{redox,F} = E_{redox,F}. \tag{2.8}$$

According to semiconductor terminology a Fermi energy of the redox couple $E_{\text{redox,F}}$ can be defined separating the occupied from the unoccupied states. It is sketched at the intersection of the distribution of empty with occupied states (cf. Figure 2.5d).

Due to thermal motion of solvent molecules and the influence on the interactions between oxidized/reduced species with the solvent, the energetic distribution of states has a Gaussian shape [49, 50] which can be described by Eq. 2.9 and 2.10[1] (cf. Figure 2.6).

$$D_{ox} = e^{\left(-\frac{E - E_{redox,F} - \lambda^2}{4 \cdot k \cdot T \cdot \lambda}\right)} \tag{2.9}$$

$$D_{red} = e^{\left(-\frac{E - E_{redox,F} + \lambda^2}{4 \cdot k \cdot T \cdot \lambda}\right)} \tag{2.10}$$

This permanent energetic fluctuation of states implies that in the case of redox couples no photonic excitation from an unoccupied to an occupied state is possible [53].

2.2.3. Energy Scales

To achieve comparability between solid state physics and the electrolyte, a common reference energy has to be defined. While in solid state physics the vacuum–level E_{vac} is used as such a reference, in electrochemistry traditionally the redox potential of the redox couple H^+/H_2 in contact with an inert platinum electrode under standard conditions ($T = 298\,\text{K}$, $p = 1\,\text{bar}$, $c_x = 1\,\text{M}$) is used, defining the *normal hydrogen electrode* (NHE) with potential = $0\,\text{V}$. The exact energetic position on the solid state

---

[1]Mathematically this is realized by a Gaussian distribution according to the Marcus theory based on the assumption that the solvent fluctuations are described by a harmonic oscillator [52].

scale is rather difficult to determine. Several values have been published spanning the range between -4.3 and -4.9 eV [54, 55] on the solid state energy scale. In this work, the most accepted value published by Lohmann et al. [56] at -4.5 eV will be applied as zero for the NHE scale. The measured standard redox potentials E^0 of specific redox couples are related to the NHE. The sign of the energy is positive if the species under study tends to release electrons more easily to the reference platinum electrode than the H^+/H_2 redox couple. In Figure 2.6, the two energy scales are depicted. Additionally the energetic values, which are important for this work are listed.
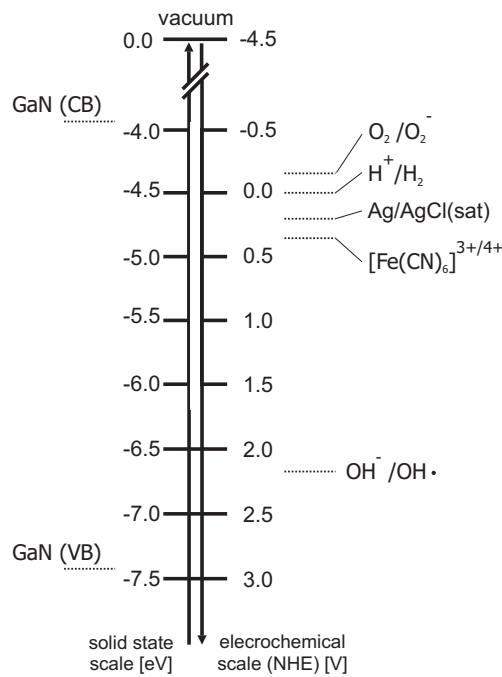

Figure 2.6.: Comparison of energetic positions of different redox couples and the GaN band edges between solid state scale and electrochemical scale at pH 7. Energetic values from [57, 58]

The two energy scales are correlated by Eq. 2.11.

$$E_{\text{redox}}(\text{NHE}) = -4.5\,eV - e \cdot E_{\text{redox}}(\text{solid state}) \qquad (2.11)$$

Because the NHE is experimentally difficult to realize and inconvenient in longer operations, in this work a Ag/AgCl double junction reference electrode is used. Further advantages of the Ag/AgCl electrode arise from the well known behavior of metal ion electrodes. Metal ion electrodes are generally characterized by fast response times and good reproducibility because of a stable potential determined by the activity of Cl^- ions in the saturated solution. Further detailed descriptions can

be found in [18]. The energetic position in relation to the NHE is $E_{Ag/AgCl} = 222\,mV$ [18] and is also indicated in Figure 2.6.

2.2.4. Ionic Liquids

In comparison to electrolytes based on water as solvent, water–free compounds offer several advantages. The class of *ionic liquids* (ILs) which are of purely ionic nature is one representative of such water–free solvents. They consist of a large organic cation with low symmetry and an anion for charge neutrality. There exists a multitude of different composition with different electrochemical properties depending on the used cation and anion [59]. The ILs which are of particular interest here provide a large potential window of stable operation usually between 3 and 4 V, a conductivity that is comparable to that of water–based electrolytes, a hydrophobic character and a melting point below room temperature. Their greatest advantage in comparison to other water–free electrolytes (e.g. acetonitrile) is that they are non–toxic and for specific choices of a hydrophobic IL easier to handle.

In this work the classification of an ionic liquid formulated by John S. Wilkes will be used [60]. He defined ionic liquids as molten salts with a large liquidus range between melting point and boiling point, whereas the melting temperature lies bellow the boiling point of water.

Figure 2.7 depicts the structure formulas of the cation and the anion of the used IL. Figure 2.7a shows the cation, 1-Ethyl-3-Methylimidazolium ([EMIM]$^+$) while in part b) the anion of the non hygroscopic IL Bis(Trifluoromethylsulfonyl) imide ([NTf$_2$]$^-$) is shown.

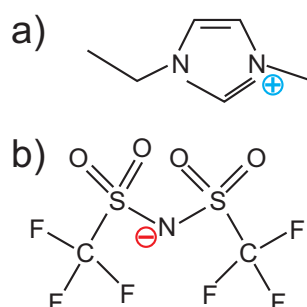Figure 2.7.: Chemical structure formulas of the used ionic liquids components a) cation ([EMIM]$^+$) b) and anion ([NTf$_2$]$^-$).

1-Ethyl-3-Methylimidazolium Bis(Trifluoromethylsulfonyl)imide [EMIM][NTf$_2$]which has a conductivity of $6.6\,mS\,cm^{-2}$ [61] and is highly hydrophobic, implying that it is

not miscible with water. Additionally, the melting point lies below room temperature and the IL is commercially available at IoLiTec GmbH.

Due to the fundamental differences between water and ILs, the concept of pH value is difficult to apply to water–free solutions. Up to now also an exact description for measuring the pH is still missing [62].

In any case an ideal IL is free of pH determining ions, especially OH^-, and consequently could serve as an alternative to water–based electrolytes for application of electric potentials to the NWs.

In literature synonyms like *room temperature molten salts* (RTMS) or *liquid organic salts* (LOS) are also used for the group of ILs. For specific details about synthesis, purification or other physical parameter please refer to textbook e.g. [59].

2.3. The Interface Region

In this section the two systems independently discussed so far, the semiconductor Gallium Nitride (2.1) and the electrolyte (2.2) are brought in contact. The electrical characteristic of this interface can be described in analogy to a *Schottky–contact* [19, 63].

2.3.1. Schottky–Contact

In general, the deposition of a metal contact onto a clean semiconductor surface can either result in ohmic or diode–like (rectifying) behavior. In the latter case this is called a Schottky–contact which is defined by a Schottky–barrier at the interface. What kind of contact is established depends on the material properties (work function, electron affinity etc.) and the deposition method [19]. The electrolyte or more specific the redox couple is described with a Fermi energy (cf. section 2.2) in analogy to a metal.

In contact with the electrolyte the Fermi level of the semiconductor and the Fermi level of the electrolyte containing a redox couple equilibrate [49, 50]. This is achieved by interfacial charge transfer and the rearrangement of the ions on the electrolyte side of the surface. The driving force behind this is purely thermodynamic and in an ideal case fully reversible. A so–called contact potential is established between the semiconductor surface representing the electrode and the electrolyte. As this potential cannot be measured independently a second electrode with a constant and well defined potential is immersed as a reference. The potential difference between

these two electrodes is called the *open circuit potential* or *open circuit voltage* (U_{OCP}) of the semiconductor electrode under examination. In all measurements conducted in this work a Ag/AgCl reference electrode was used. With the addition of one further electrode, the so–called counter electrode, it is possible to apply external voltages to the semiconductor surface.
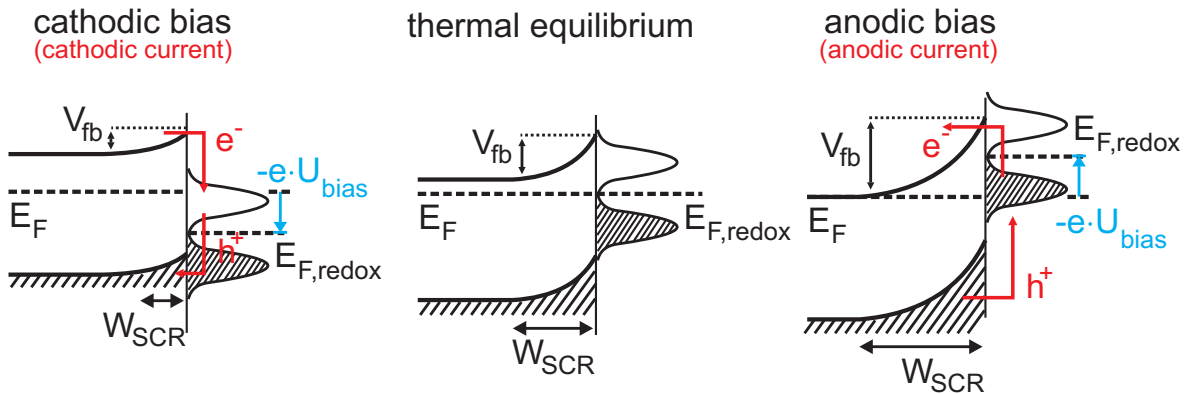

Figure 2.8.: N–type semiconductor with electrolytic Schottky–contact under various applied bias voltages.

According to Memming [51] the electrolyte/semiconductor can be described on the basis of interfacial charge transfer between the electrolyte, especially a *redox couple* (cf. section 2.2.1), and the semiconductor. Figure 2.8 shows the semiconductor energy with the density of states for a redox couple in thermal equilibrium (middle part) in the form of Gerischer diagrams. In general, the x–axis of the Gerischer diagrams is different on both sides of the diagram. On the semiconductor side it represents a spatial coordinate in the nm regime (cf. spatial extension of the SCR in section 2.1.1) while on the electrolytic side it represents a *density of states* (DOS) for the redox couple. The comparison of the real distances reveals that the spacings on the electrolyte side are one order of magnitude smaller then on the semiconductor side.

The application of external bias to the interface impacts the SBB as depicted in Figure 2.8 on the right for cathodic bias and on the left for anodic bias. The width of W_{SCR} and the effective barrier height (V_{fb}) for electrons decrease with cathodic bias while they increase for anodic bias. Interfacial hole transfer from the n–type semiconductor into the redox couple is especially in favor for anodic bias.

Interfacial charge transfer between a semiconductor and electrolyte can only occur isoenergetically via the conduction or valence band. A *cathodic current* is defined for the case that the solutions redox species are reduced by electron (e^-) injection into an empty state of the redox couple. Complementary an *anodic current* is defined

by the injection of a hole (h^+) from the valence band into an occupied state of the redox couple where an oxidation is the consequence. These currents are indicated by red arrows in the illustration of Figure 2.8.

The externally applied bias U_{bias} is also indicated in Figure 2.8. The so–called flat band situation is characterized by compensation of the SBB and is achieved when the $-e \cdot U_{\text{bias}} = V_{\text{fb}}$. With the possibility of bias modulation of the SBB Eq. 2.1 can be extended to Eq. 2.12.

$$W_{SCR} = \sqrt{\frac{2 \cdot \varepsilon_{sc} \cdot \varepsilon_0}{e \cdot N} \cdot (V_{fb} - U_{bias})} \tag{2.12}$$

This implies that the SBB can be controlled by an externally applied bias.

Surface States

For interfacial charge transfer, surface states play an essential role because they can provide energy levels for isoenergetic charge transfer to or from the electrolyte redox couples. Additionally, surface states can act as non–radiative recombination centers for the photo–excited carriers.

Depending on the density of surface states the semiconductor/electrolyte interface must be treated differently compared to the potential distribution across the interface. This will be further discussed in the following section 2.3.2.

2.3.2. Potential Distribution Across the Interface

All theories describing the solid/liquid interface are based on the examinations of the mercury/electrolyte interface extensively studied by Otto Stern [17].

Gouy–Chapman–Stern Model for Semiconductors

As previously discussed, the surface of a semiconductor is characterized by a specifically localized charge density caused by the existence of surface states. The potential difference between the correlated *surface potential* ϕ_S and the potential at the OHP ϕ_{OHP} defines the Helmholtz double layer voltage V_{HH}.

In the following, a semiconductor electrode in contact with an electrolyte is examined under the restriction that the density of surface states is small and that specific adsorption can be neglected. Specific adsorption includes hereby physisorption (Van de Waals forces), chemisorption (covalently bonding) and electrostatic attraction (ionic charges).

Figure 2.9 schematically shows how the solvated ions arrange to compensate ϕ_S. The smallest distance to which a solvated ion can approach from the electrode surface is determined by its solvation sheath. The plane of solvated ions that forms at this minimal distance is called the *outer Helmholtz plane* (OHP), characterized by the potential V_{HH}. With its counterpart at the surface these two fixed charge densities form the so–called *Helmholtz double layer* with the associated *Helmholtz capacitance* C_{HH} [17].

$$C_{HH} = \frac{\varepsilon_0 \, \varepsilon_r}{d} \tag{2.13}$$

The dielectric constant ε_r of the medium, consisting of strongly polarized water molecules is still under discussion. In literature values between 5 and 20 have been reported [53, 51]. Considering the dielectric constant $\varepsilon_r \approx 5.9$ for fully oriented water one can calculate a thickness of the Helmholtz double layer in the lower Ångstroms range. The potential drop occurring in this layer is linear.

Adjacent to this highly localized layer a diffuse charge layer extending from the OHP into the bulk electrolyte exists. The electrostatic forces present in this so–called *Gouy–Chapman layer* with the associated capacitance C_D are counterbalanced by the thermal motion of the ions [18].

The capacitance of the diffuse Gouy–Chapman layer C_D depends strongly on the concentration of the electrolyte. For electrolytes with high concentration (> 0.1 mM) its capacitance can be neglected due to the serial connection with the Helmholtz capacitance C_{HH}. The electrolytes used in this work are characterized by a high concentration so the neglection of the diffuse layer is reasonable. Further details can be found in [16, 18].

Helmholtz layer and Gouy–Chapman layer together form the *Gouy–Chapman–Stern layer* (GCS) as depicted in Figure 2.9. The total capacitance of the Gouy–Chapman–Stern layer C_{GCS} can be described as a series of capacitances.

$$\frac{1}{C_{GCS}} = \frac{1}{C_{HH}} + \frac{1}{C_D} \tag{2.14}$$

The total capacitance of the semiconductor/electrolyte interface can be expressed by a serial connection of the GCS capacitance, C_{GCS}, and the semiconductor space charge region capacitance C_{SCR}, with Equation 2.15.

$$\frac{1}{C_{total}} = \frac{1}{C_{SCR}} + \frac{1}{C_{HH}} + \frac{1}{C_D} \tag{2.15}$$

Charging of the capacitances is assumed to be a reversible process. Faradayic
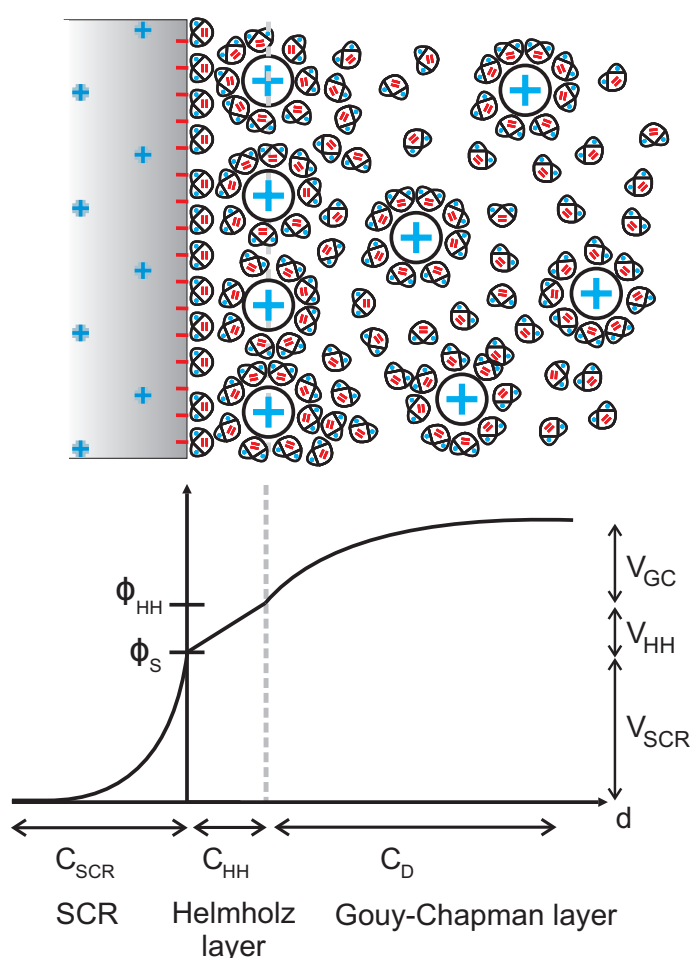
Figure 2.9.: a) Schematic of the Helmholtz double layer and the Gouy–Chapman layer at a semiconductor electrode. b) Potential distribution and the associated capacitances.

currents occur when the capacitor undergoes a dielectric breakdown indicating that electrochemical surface–reactions occur. If the evolving species remains at the surface, the reaction is still reversible. If the products diffuse into the solution the reaction is irreversible.

Semiconductors exhibiting a high density of surface states or a very high degree of specific adsorption show a different potential distribution across the interface. The high amount of charge localized at the surface of the semiconductor grant the interface a character similar to a metal/electrolyte contact [28]. This implies that the potential drop between the semiconductor electrode and the electrolyte occurs almost completely within the Helmholtz capacitance C_{HH} as illustrated in Figure 2.10. In this case no influence of the SCR is detectable.
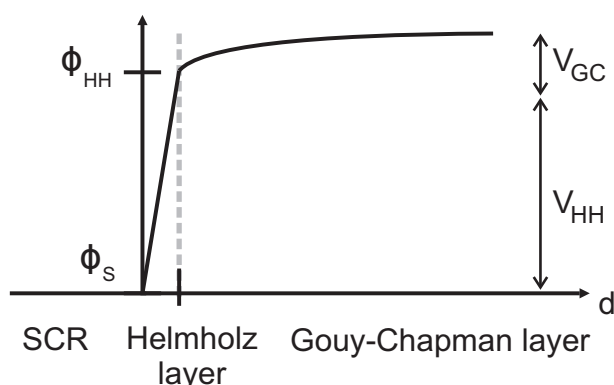
Figure 2.10.: Schematic of the Gouy–Chapman–Stern layer at a semiconductor electrode dominated by surface states and specific adsorption. The potential drop between the semiconductor electrode and the electrolyte occurs within C_{HH}.

2.3.3. Illumination Effects

Illumination with $E_{exc} > E_g$ of the interface has a major impact on the semiconductor in the form of photo–excitation of charge carriers, while in the electrolyte no such effect occurs. These photo–generated charge carriers are separated due to the presence of electric fields as for example in the space charge region resulting in a high hole concentration at the surface of a n–type semiconductor (cf. section 2.1.2). According to these excess minority charge carriers at the surface, the value of the surface potential ϕ_S and the open circuit potential under illumination U_{OCP} differs significantly from measurements in the dark. Furthermore, the adsorbates at the surface are stripped off as consequence to the change of ϕ_S.

The U_{OCP} of a semiconductor electrode under illumination depends only on the specific redox couple which is characterized by its Fermi energy and not on its concentration [64]. It serves as a reference potential for the succeeding bias–dependent PL measurement.

Figure 2.11 illustrates the band profile for a n–type semiconductor under OCP–conditions illuminated with above bandgap light. The resulting non–equilibrium state is characterized by a U_{OCP}. This value also depends on the pH value as explained by the site–binding model [65]. By the application of an external bias this voltage difference can be controlled. The influence of the different polarities is indicated on the semiconductor size. Cathodic bias decreases the SBB while anodic bias increases it for n–type semiconductors.
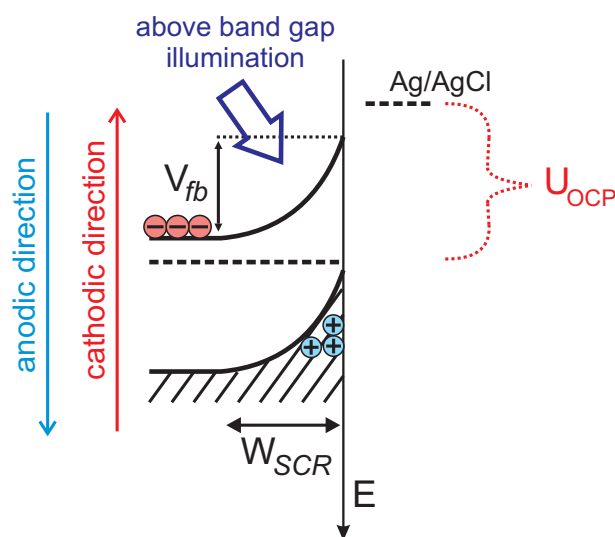
Figure 2.11.: The OCP under illumination with above bandgap light and the effects of bias application on the band profile for a n–type semiconductor.

2.3.4. pH–Sensitivity of Gallium Nitride

For GaN surfaces it is commonly accepted that a native oxide layer is formed when the surface is in contact with ambient atmosphere [66, 67]. The exact formation and structure of this layer are still under discussion and will not be addressed here. Nevertheless, this natural oxide layer has a strong impact on the surface chemistry. In contact with an electrolyte adsorption and desorption of ions strongly influences the surface potential ϕ_S and consequently the band profile. For oxides in contact with water the most important ions are H_3O^+ and OH^-.

Steinhoff et al. [66] showed that native GaN and thermally oxidized GaN layers surface potential show similar behavior towards changes of the electrolytes pH value. They determined an almost Nernstian behavior with an extracted sensitivity of 56 mV/pH for ϕ_S over the pH–range between 2 and 12.

Site–Binding Model

Generally, the pH–dependence of oxide surfaces is described by the site–binding model [65] which will be presented briefly in the following. The site–binding model was formulated by Yates et al. [65] for a metal–oxide surface in aqueous electrolyte, which is assumed to be ideally polarizable with no occurring Faradayic currents. At the surface, ionizable hydroxyl surface groups (Oxide – OH) are formed. The site–binding model is illustrated in Figure 2.12. Figure 2.12b shows the neural state of these groups. These sites express an amphoteric character, i.e. they can be either
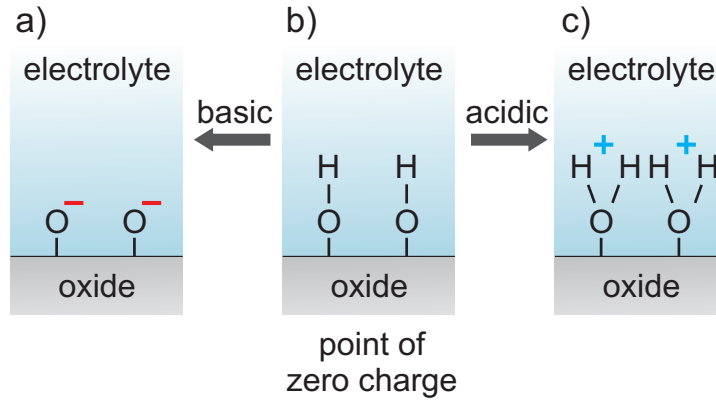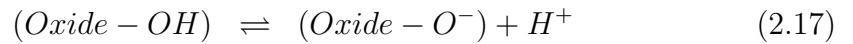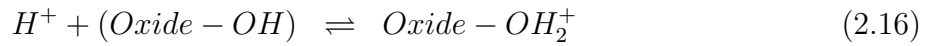
Figure 2.12.: Illustration of the site–binding model with the ionizable hydroxyl surface groups (Oxide – OH) and their a) deprotonated and c) protonated forms and in b) the point of zero charge.

positively charged by protonation (binding of H^+) or negatively charged by deprotonation (release of H^+) described by Eq. 2.16 and 2.17.

$$H^+ + (Oxide - OH) \rightleftharpoons Oxide - OH_2^+ \qquad (2.16)$$

$$(Oxide - OH) \rightleftharpoons (Oxide - O^-) + H^+ \qquad (2.17)$$

The relation between positive (Oxide – OH_2^+), negative (Oxide – O^-) and neutral (Oxide – OH) sites is directly related to the pH value of the electrolyte. The equilibrium between the relative concentrations of negative [(Oxide – O^-)], neutral [(Oxide – OH)], and positive [(Oxide - OH_2^+)] surface groups with the concentration of protons at the surface [H_S^+] is described by two dissociation constants,

$$K_- = \frac{[(Oxide - O^-)] \cdot [H_S^+]}{[(Oxide - OH)]} \qquad (2.18)$$

$$K_+ = \frac{[(Oxide - OH)] \cdot [H_S^+]}{[(Oxide - OH_2^+)]} \qquad (2.19)$$

The so called *Point of Zero Charge* is defined as the pH value at which [Oxide – OH_2^+] and [Oxide – O^-] are equally distributed, resulting in a zero net charge at the surface described by Eq. 2.20 and consequently leading to a surface potential $\phi_S = 0$.

$$\sigma_S = e \cdot ([Oxide - OH_2^+] - [Oxide - O^-]) \qquad (2.20)$$

As discussed in [68] under the assumption that the number of surface states switching polarity (change between protonated and deprotonated state) is small in com-

parison to the overall number of surface states the surface potential follows the linear Nernstian dependence of 59 mV/pH.

For GaN surfaces several values are reported in literature. A value of pH_{PCZ} = 8.47 was reported in [69] while in [70] a theoretical value pH_{PCZ} = 6.8 was calculated for a Ga–face oxide.

When it comes to biological inspired application e.g. the monitoring of the pH change during an enzymatic or cellular reaction, which typically occur in the vicinity of the neutral point (pH $\approx$ 7) a charged surface might still affect the reaction. For the most prominant candidate of semiconductor sensors, silicon dioxide, a pH_{PCZ} of 2.2 was reported by [71]. In contrast to GaN this could introduce a major disadvantage for biological related sensor applications based on Silicon.

Experimental

A major breakthrough concerning the measuring techniques of electrical potentials was achieved by A. Hickling between 1937-42 [72, 73] who introduced the "potentiostat" to measure electrode potentials. Besides new electrical circuit architecture he introduced the so–called three–electrode configuration which effectively overcomes the problem of measuring the electrodes potentials, while a parasitic potential arises from the current flowing across the same electrodes and its resistance.

The systematic analysis of the solid/liquid interface started in the early 1970s triggered by the growing interest in solar energy conversion due to the first oil crisis in 1973. In those years the basic theory which is still the best approximation for the semiconductor/electrolyte interface was formulated by Gerischer et al. [49, 50, 74, 75]. In the following years, mainly possible applications of the photo–electrochemistry founded by Gerischer were pursued, while the theoretical understanding of the system is still dominated by his ideas of energetic levels in the electrolyte.

From the large variety of electrochemical methods two techniques used in this work, namely "Impedance Spectroscopy" (IS) and "Cyclic Voltammetry" (CV), and the related experimental setups will be presented.

Then the focus is put on the "photoelectrochemical" characterization of the NWs. Optical examination methods provide a high spatial and temporal resolution while being non invasive. Here photoluminescence spectroscopy (PL) is used to characterize the semiconductor/electrolyte interface.

Prior to the presentation of the different experimental techniques the sample preparation of GaN NWs will be described in detail.

In the end of this chapter, ionic liquids will briefly be introduced. Due to their specific electrical properties they offer great potential in verifying the proposed theory about the solid / liquid interface.

3.1. Group III–Nitride Nanowires

The GaN NWs examined in this work were grown by plasma–assisted molecular beam epitaxy (PAMBE) using a catalyst–free self–assembled growth process in ni-

trogen rich conditions on highly conductive n– and p–type Si (111) substrates. Details on the growth process are reported in [14, 42]. In the following, only the most important aspects for further analysis are summarized.

N–type Si substrates doped with phosphorus and p–type substrates doped with boron with a specific resistance of $\rho = 0.003 - 0.007\,\Omega$cm were used.

After removal of the native oxide layer with buffered hydrofluoric acid (6%) the samples were introduced into the growth chamber. Prior to NWs growth process the samples were exposed to a nitrogen plasma creating an amorphous nitridation layer. NWs grown without additional supply of doping material (silicon or magnesium) are refereed to as *"non intentionally doped"* (n.i.d.). These NW exhibit an intrinsic n–type background doping like comparable GaN layers [36].

Figure 3.1 shows two *scanning electron microscope* (SEM) images of n.i.d. GaN NW samples. In general, the NW samples used in the experiments were characterized by a density of approx. $200\,\mu$m^{-2}, the range of NW lengths between 400 and 800 nm, and an average NW diameter between 30 and 90 nm. The NWs exhibit N–face polarity as described in [76]. These freestanding NWs exhibit a large *surface to volume ratio* (S/V) which is of crucial importance for the subsequent measurements. Depending on the exact NW geometry (diameter and height) the surface gain factor lies between 10 and 100.
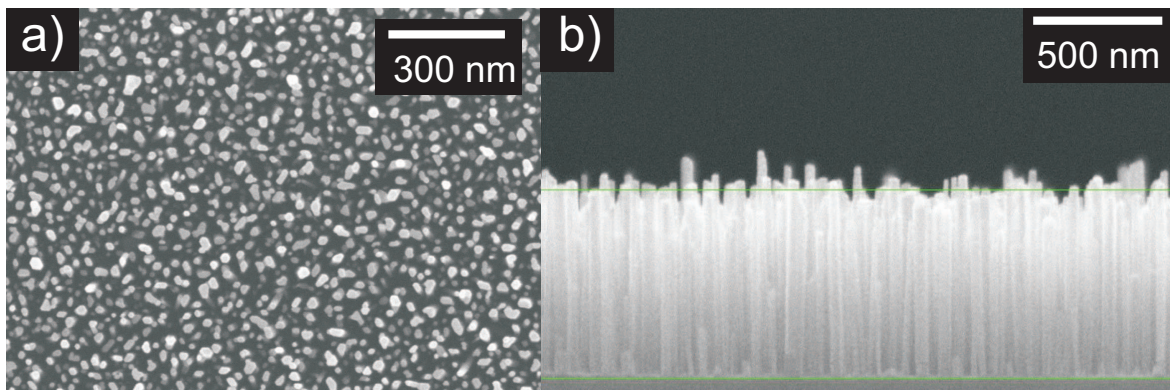

Figure 3.1.: Scanning electron microscope images of n.i.d. GaN NWs a) topview b) sideview.

Additionally to the intrinsic n–type nature of the GaN NWs [77] it is known that the NWs grown on Si substrates receive enhanced background Si–doping due to the diffusion of Si–atoms from the substrate at elevated growth temperatures. This additional background doping is most prominent in the initial stages of the growth process and expresses itself considerably in the foot region of the NW where up to 4 % silicon could be measured by electron energy loss spectroscopy (EELS).

Intentional doping of the NWs with the materials Silicon (Si) and Magnesium (Mg) was achieved by evaporating the desired dopant in thermal effusion–cells. For each dopant the corresponding *"beam equivalent pressures"* (BEPs) related to the effusion cell–temperature T_{cell} was calibrated before NW growth at the sample position and are summarized in Table 4.2.

In general, Si– as well as Mg–doping leads to an increasing average NW diameter. For high Si–concentrations it is further known that the prismatic shape of the NWs transforms into a more conical widening. This is shown in Figure 3.2 in a bright–field image taken with a scanning transmission electron microscope. The examined NW sample was grown at $T_{Si} = 1160\,°C$. In this case the angle formed between two opposing sidewalls was $\approx 7.5\,°$. Magnesium doping in general leads to a broadening of the overall NW diameter which becomes more evident with higher Mg fluxes.
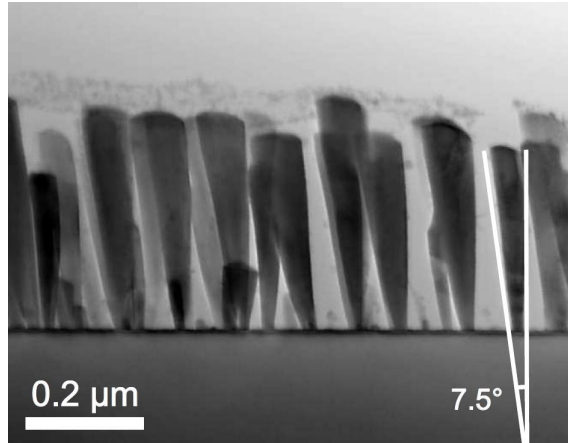

Figure 3.2.: Scanning transmission electron microscopic image in bright–field of highly Si–doped GaN NWs ($T_{Si} = 1160\,°C$) from [42].

3.2. Three Electrode Configuration

Figure 3.3 schematically shows a typical measurement setup. The electrochemical cell consists of three electrodes electrically connected via the electrolyte (marked light blue surrounded by the broken circle). The sample in such a configuration is referred to as working electrode (WE). Its potential is measured against the reference electrode (RE) across a very high resistive pathway (potential measuring half–cell). The disturbing stimulus is applied between the third electrode, the so–called counter electrode (CE) and the WE (current flowing half–cell). This pathway usually has a low resistivity to allow a low–loss conduction. To set the sample to a stable

and well known potential a bias voltage (U_{applied}) can be applied between RE and WE. Commonly the RE is grounded to achieve maximum stability of the applied potential.
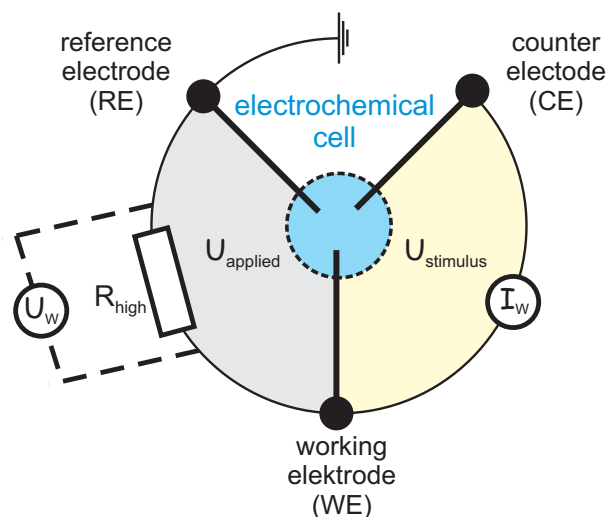

Figure 3.3.: Schematic of the functionality of a three electrode setup. The potential measuring half–cell between WE and RE is displayed in grey, the current flowing half–cell between WE and CE displayed in light yellow. The electrolyte connecting all three electrodes is located in the central broken circle (blue color).

3.3. Electrochemical Characterization

The electrochemical characterization techniques used in this work, Impedance Spectroscopy (IS) and Cyclic Voltammetry (CV) are well suited to characterize the electrical properties of materials and especially their interfaces with electrolytes.

IS has widely been used for real–time monitoring surfaces changes by e.g. etching [78] or oxidation [79] or the deposition/formation of various membrane layers [80, 81, 82].

CV is especially suited to determine charge transfer reactions and the correlated diffusion constants and redox levels. Although it was originally developed for metal electrodes it can also be applied to semiconductors and insulators.

Because it is known from the material GaN that persistent photo–currents have long decay times special care has to be taken for the electrochemical measurements to avoid above bandgap illumination [83]. To achieve this all measurements were performed in an opaque and grounded faraday cage.

For applications in biological related systems these methods represent a possibility to study the systems non–invasively and label–free in their natural environment [84]. In recent years these techniques have been applied to study the interface of many kinds of nano structures as well [8, 85, 86].

3.3.1. Setup

As prerequisite to electrical measurements it was necessary to deposit proper metal contacts on the samples.

For the GaN NWs grown on top of highly conductive, brittle Silicon substrates (cf. section 3.1) the electrical contact has to be on the backside. To avoid damage of the NWs or the nitridated interlayer, the NWs on the frontside are passivated with photo–resist prior to removing the native oxide layer on the substrate backside in buffered hydrofluoric acid solution. In a subsequent thermal evaporation process an Ohmic contact consisting of aluminum/silver ($\approx 50\,\mathrm{nm}$ / $\approx 100\,\mathrm{nm}$) is deposited on the backside of the NW samples. To control the Ohmic behavior over time the contact consists of two independent areas.

Due to the differences in sample sizes a variable specimen holders was constructed. The specimen holder was made out of Polyetheretherketon PEEK and is shown in Figure 3.4a. It was designed to guarantee high reusability of the samples and reliable electrical contacts. Details of the electrical connection are illustrated in the schemes in Figure 3.4b. The samples are mechanically pressed to seal an O–ring either with diameter of $3\,\mathrm{mm}$ ($A_{\mathrm{contact}} \approx 0.07\,\mathrm{cm}^2$) by a copper piston which simultaneously acts as electrical connection, with a negligible resistance. In this case the compression of the O–ring is the most crucial point due to the brittleness of the substrate.

The sample holder is mounted to a beaker consisting of Polyoxymethylen (POM) containing the electrolyte ($\approx 150\,\mathrm{ml}$). To guarantee constant exchange of electrolyte above the sample an electrical stirrer is added (Figure 3.4c).

All electrochemical measurements were performed in the dark using a combined potentiostat/frequency response analyzer (Voltalab 40, Radiometer Analytical SAS, Villeurbanne Cedex, France) in combination with an Ag/AgCl double junction electrode filled with saturated KCl as reference and a Pt–pin counter electrode (Deutsche Metrohm GmbH, Filderstadt, Germany) with the NW sample or GaN layers as working electrode.
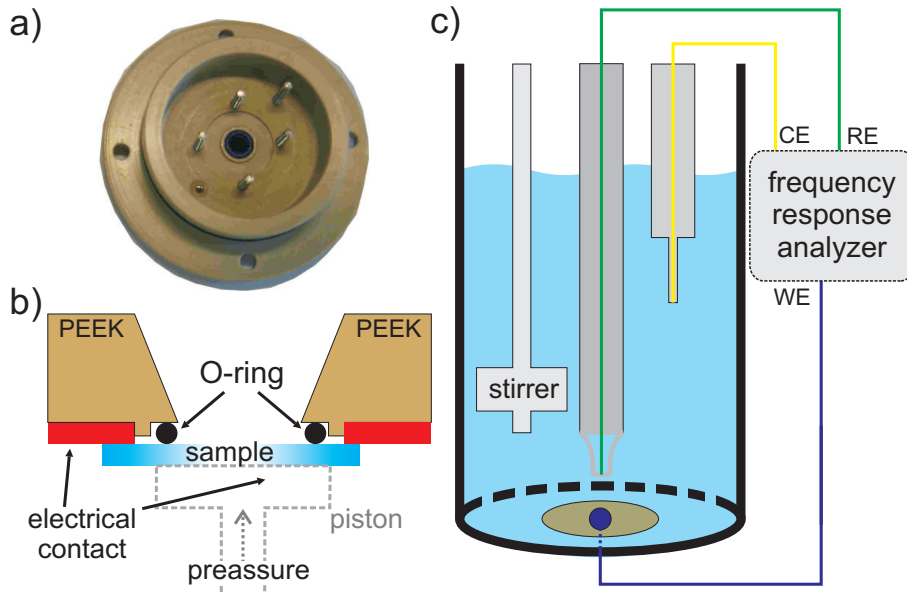
Figure 3.4.: a) Photograph and b) schematic drawing of the holder for GaN NW samples; c) Schematic drawing of the beaker used for electrochemical impedance spectroscopy with stirrer and three electrodes (sample as working electrode, counter electrode and reference electrode) and the external frequency response analyzer.

3.3.2. Impedance Spectroscopy

Using Impedance Spectroscopy (IS), the solid liquid interface can be characterized. Therefor, a small signal single–frequency voltage stimulus $U(t) = U_0 \cdot sin(\omega \cdot t)$ is applied to the system while the phase shift ϕ and amplitude $|Z|$ of the responding current $I(t) = I_0 \cdot sin(\omega \cdot t + \phi(\omega))$ are measured [87, 88]. With respect to the thermal voltage ($\approx 25 \, mV$ at room temperature) the signal amplitude is set to $10 \, mV$ to account for equilibrium conditions.

$$\phi = tan^{-1}\left(\frac{Z''}{Z'}\right) \tag{3.1}$$

$$|Z| = [(Z')^2 + (Z'')^2]^{\frac{1}{2}} \tag{3.2}$$

The derived data were plotted in the so–called *Bode–Plot* where the original time dependence is replaced by the frequency dependence. It shows the logarithmic impedance amplitude $|Z(\omega)|$ and the phase angle $\phi(\omega)$ plotted versus the logarithmic frequency $f = 2\omega \cdot \pi$ of the applied voltage signal. An exemple for a Bode–Plot is shown in Figure 3.7.

Electrical Equivalent Circuits (EECs)

As a detailed physioelectrical description of the macroscopic electrode is impossible, the measured impedance spectra are compared to impedance spectra simulated by *electrical equivalent circuits* (EECs) [87]. Figure 3.5 introduces discrete electrical components which can be combined in an EEC to describe the overall reaction of the system. In such a circuit a resistor represents a conductive path (e.g. bulk conductivity of the sample, electrolyte, or a chemical reaction step at the electrode) while capacitances and inductances are associated to charging space charge regions or specific ad– desorption. These electrical compounds are generally considered as ideal. Due to the spatial extension and non–ideality of the structural properties of real surfaces (e.g. surface defects and dangling bonds) deviations from ideal behavior can be implemented using a *constant phase element* (CPE).
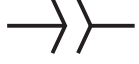
electrical element	symbol	impedance $Z_{i(\omega)}$
resistance **R**		$Z_R(\omega) = R$
capacitance **C**		$Z_C(\omega) = (i\omega C)^{-1}$
inductance **L**		$Z_L(\omega) = i\omega L$
constant phase element **CPE**		$Z_{CPE}(\omega) = Y_0 \cdot (i\omega)^{-\alpha}$
warburg element **W**		$Z_W(\omega) = W \cdot (i\omega)^{-0.5}$

Figure 3.5.: List of discrete electrical circuit elements used in EECs.

With R as the Ohmic resistance, C as the capacitance, L as the inductance, Y_0 the so–called admittance, and α. For a value of $\alpha = 1$ the CPE realizes an ideal capacitor while $\alpha = 0$ represents purely resistive behavior. In the special case of $\alpha = 0.5$ the resulting component is called a *Warburg element* with the characteristic parameter W. This is especially applicable to systems with a dominating influence of diffusion processes.

It is known that due to diffusion restrictions arising from surface roughness the

transition from a capacitor to a CPE with a slight variation of α improves the data fitting considerably [89, 90]. In such cases the corrected capacitance can be calculated according to Hsu et al. [91] from the parameter Y_0 by the expression

$$C = Y_0 \cdot (\omega(max))^{\alpha-1} \tag{3.3}$$

When comparing EECs to measured IS data a multitude of theoretical circuits can always be modeled to fit the experimental data. To choose an adequate model for the system one has to consider additional physical information about the examined system to avoid redundancy. However, any model circuit includes only a finite number of elements and consequently can only be an approximation of the real system. The theoretical IS were adapted to the experimental data using a Levenberg–Marquardt algorithm for complex non–linear curve fitting [90].
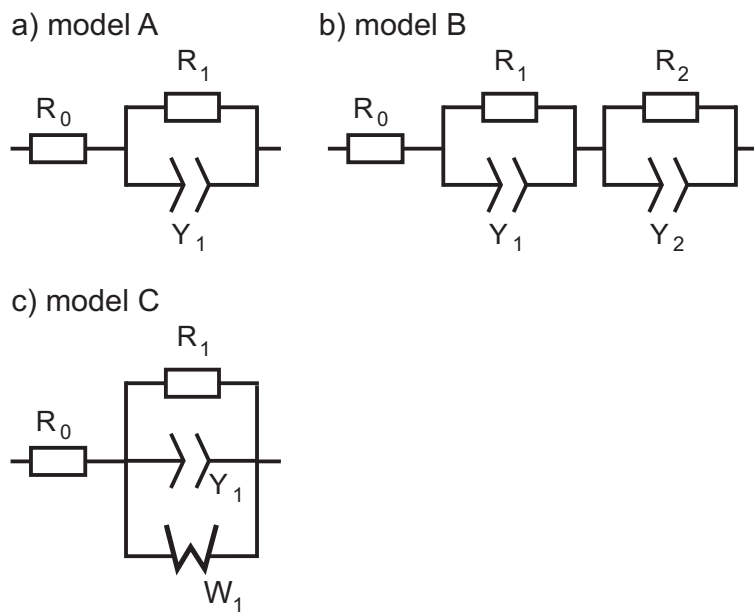
Figure 3.6.: EEC models used for fitting IS data.

Figure 3.6 shows the equivalent circuits used for data fitting in this work. In all three models the resistance R_0 contains the electrolyte, ohmic contacts, cables and parasitic resistances. In model A a resistor R_1 in parallel with an CPE Y_1 is connected in series to R_0. A CPE is chosen because by slight variation of α the fit quality can be increased significantly. A parallel combination of an Ohmic resistor and a capacitor or in general a CPE is called a *RC–element* characterized by a specific time constant $\tau = RC$.

In model B a second RC–element represented by R_2 and C_2 is introduced in series

to model A . In general, it is mathematically impossible to determine the sequence of RC–elements and resistors.

Model C adds a Warburg element W_1 in parallel to model A which accounts for diffusion in the case of rough surfaces.

Figure 3.7 schematically shows an impedance spectrum simulated with model A according to Eq. 3.4. The modifications of the spectrum by the four parameters R_0, R_S, C_S and α are indicated with arrows.

$$Z(\omega) = R_0 + \left(C_S(i\omega)^\alpha + \frac{1}{R_S} \right)^{-1} \tag{3.4}$$
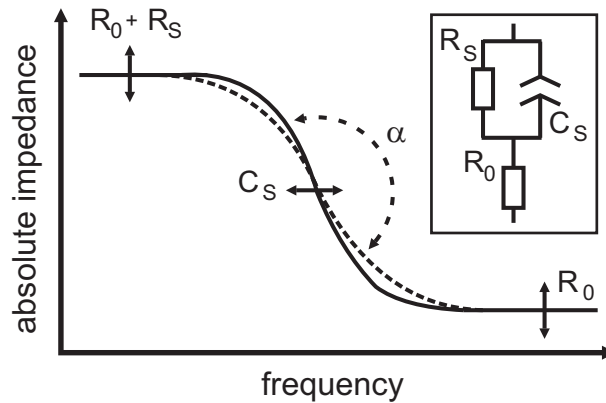
Figure 3.7.: Simulation of a Bode–Plot according to model A.

Generally, two RC–elements in series can be distinguished in IS when two criteria are full filled.

- Their time constants differ by at least one order of magnitude.

- The values for their resistances differ by not more than $10\,\text{k}\Omega\cdot$ cm^2. This restriction is necessary due to the limited accessible frequency range.

For a more detailed description refer to J. Ross Macdonald [87].
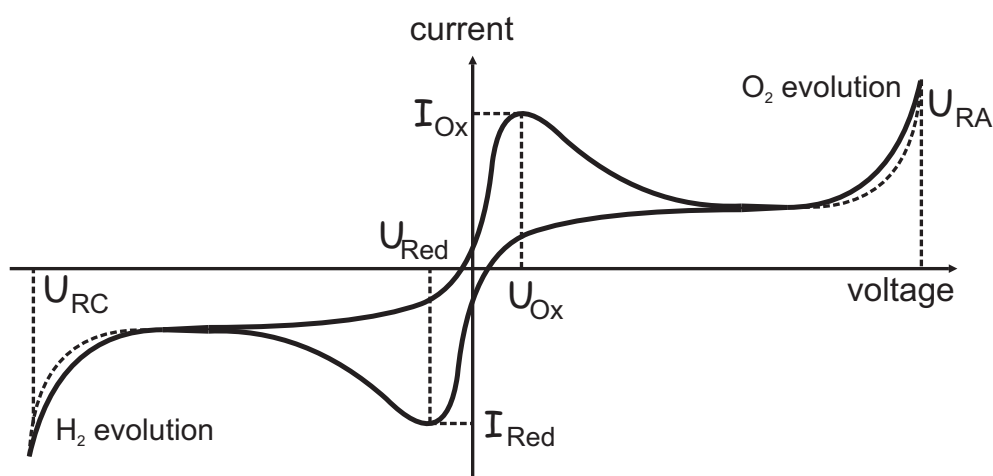
3.3.3. Cyclic Voltammetry

Figure 3.8.: Scheme of a cyclic voltammogram for fully reversible charge transfer. At higher voltages the decomposition of the electrolyte in this case water is starting.

Figure 3.8 shows the schematic of a cyclic voltammogram with fully reversible charge transfer. The voltage between RE and WE is continuously swept between the anodic and cathodic reverse potential (U_{RA}, U_{RC}) with constant scan velocity v_{cv} = $dU_{applied}/dt$ while the current is recorded. Visible are two current peaks that can be attributed to the oxidation and reduction of the redox couple in solution at certain voltages (U_{Ox} and U_{Red}). The value of the corresponding currents (I_{Ox} and I_{Red}) are proportional to the square root of the scan velocity $v_{cv}^{0.5}$ [92, 29] while the peak positions remain unchanged. For optimal experimental conditions each voltammogram recorded in a cycle reproduces exactly its prequel. One has to take care to avoid possible decomposition of the electrolyte as indicated in Figure 3.8 for larger applied potentials in the case of water.

The characteristics for full reversibility of the charge transfer according to [18] are:

- The potential difference between the oxidation (anodic) and reduction (cathodic) peak is $\Delta U = U_{Ox} - U_{Red} = 59\,mV$.

- The peak positions of the anodic and cathodic peak do not change with scan velocity v_{cv}, while the peak currents are proportional to the square root of the scan velocity.

- The ratio of the peak currents is equal to one, i.e. $\frac{|I_{Red}|}{|I_{Ox}|} = 1$.

In general, water–based electrolytes are decomposed into hydrogen and oxygen for high potentials in both polarities. Therefore all measurements are performed within the voltage range (potential window) where no decomposition occurs [18]. For water this is roughly -1 V to 1 V.

In this work, cyclic voltammetry is mainly used to verify the charge transfer into a redox couple across different interfaces.

3.4. Photoelectrochemical Characterization

In addition to the setup for purely electrochemical characterization of GaN NWs presented in the previous section 3.3, a second setup that combines the benefits of a three electrode configuration with simultaneous optical excitation was developed.

3.4.1. Setup

Figure 3.9 shows a schematic of the experiments consisting of the flow chamber with the sample mounted into a three electrode configuration connected with the potentiostat and an attached voltage source, and the peristaltic pump for electrolyte circulation with the adjacent electrolyte reservoir including the pH and conductivity–meter. The PL microscope with the connected spectrometer is used for guiding the excitation and detection light to and from the sample.
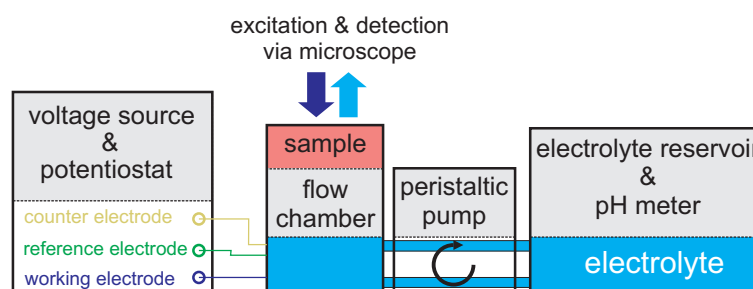

Figure 3.9.: Schematic of the experimental setup for photoelectrochemical PL measurements.

Flow Chamber

The measurements were performed in a specifically designed flow chamber constructed from of inert PEEK, depicted in Figure 3.10. The mounting mechanism is identical to that described in section 3.3.1 for IS measurements on GaN NWs. A

three electrode configuration is realized by an Ag/AgCl micro reference electrode (DriRef 450, World Precision Instruments INC., Sarasota, U.S.A.) and a platinum tube as counter electrode integrated into the drain section as can be seen in the schematic illustration in Figure 3.10b. The excitation as well as the detection light passes through the microscope setup (cf. section 3.4.2), the quartz glass window sealing the top of the chamber, and the electrolyte to the sample surface. To minimize the loss of intensity due to scattering and absorption passing through the electrolyte the distance between window and sample was kept as low as possible ($\approx 4\,\mathrm{mm}$).

PBS in a concentration of $10\,\mathrm{mM}$ was used as electrolyte. Detailed information on the electrolyte constituents and typical values for the conductivity are given in appendix E.
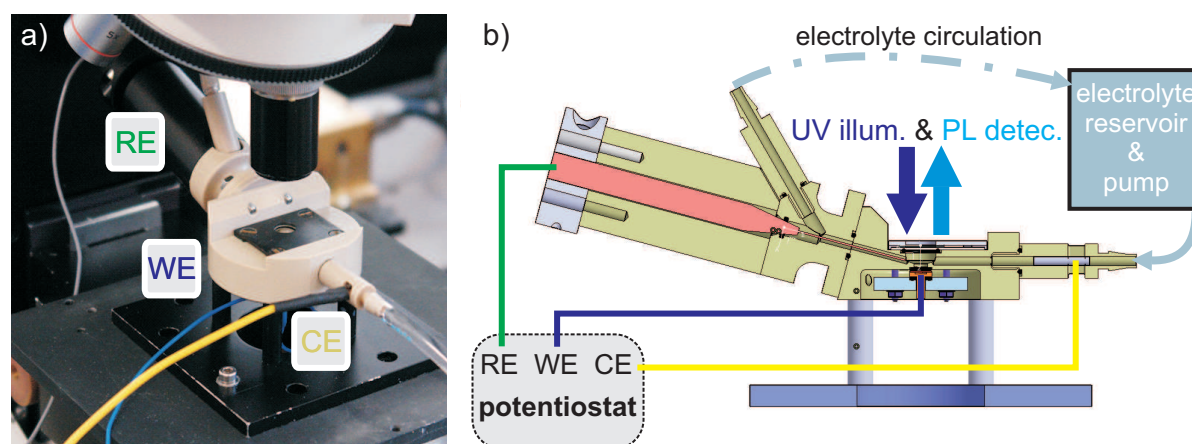
Figure 3.10.: a) Photograph and b) schematic of the flow chamber setup for photoelectrochemical characterization of GaN NWs.

The flow chamber is connected to a potentiostat (Wenking LB 81M, Bank Elektronik GmbH, Giessen, Germany) to control the potential between RE and WE. To be able to automatically control the potential, an external voltage source (Sourcemeter 2400, Keithley Instruments Inc., Cleveland, U.S.A.) is used.

To guarantee that each position within the sample area defined by an O–ring can be measured, the whole flow chamber is attached to a x,y stage below the microscope.

Peristaltic Pump

To achieve fast and continious exchange of the solution inside the measurement chamber a peristaltic pump (Perimax 12, Spetec GmbH, Erding, Germany) with

chemically inert tubes of elastic polymere is used. This setup offers the possibility to arrange a closed cycle circulation system under defined ambient conditions. If not mentioned otherwise the standard pumping velocity was set to 6 ml/min at room temperature and without further control of the ambient atmosphere.

Additionally, the influence of the composition of the electrolyte, especially the pH value and the conductivity can be modified in an external reservoir and inserted without interruption into the measurement chamber using the peristaltic pump.

pH & conductivity Meter in the Electrolyte Reservoir

To adjust or measure the pH value of the electrolyte, a pH meter with a glass electrode filled with saturated KCl solution was used (Seven Multi, Mettler Toledo GmbH, Schwerzenbach, Switzerland). If not mentioned otherwise, the pH and the conductivity of the solution was measured at room temperature before to each measurement.

The pH value was adjusted while the solution was continuously stirred by titration with HCl for acidic values and by NaOH for basic values, respectively. The conductivity of the electrolyte was also monitored with the same setup and adapted by addition of NaCl salt.

3.4.2. Photoluminescence Spectroscopy in an Electrolyte

An introduction to the basics of photoluminescence spectroscopy was already given in section 2.1.2. In the following, the experimental details are presented. PL excitation and signal detection were performed in a combined Raman–PL spectrometer/microscope (inVia Raman Microscope, Renishaw, Birmingham, Great Britain; Leica DM LM/P, Leica Microsysteme GmbH, Wetzlar, Germany) setup.

As excitation sources for the PL signal two different types of lasers have been used:

- A continuous wave HeCd laser (30 mW) at $\lambda = 325$ nm (necessary for above band gap illumination of GaN) referred to as UV–laser. This laser was used with a 10–fold UV objective (numerical aperture of 0.25, effective focal length of 20 mm) with a working distance of ≈ 8 mm. When passing through the quartz window and the electrolyte the laser spot has a diameter of $\approx 100 \, \mu$m on the sample surface.

- A frequency doubled continuous wave Nd:YVO$_4$ laser at $\lambda = 532$ nm (necessary for above band gap illumination of InGaN) referred to as green–laser. This laser was either used in combination with the 10–fold UV objective or a 5–fold objective for visible light (numerical aperture of 0.12, effective focal length of 14 mm)

The spectrometer is equipped with two different gratings of 3600 line/nm for excitation with the UV–laser and 1800 lines/nm for excitation with the green–laser. The laser power at the sample surface can be reduced by neutral density absorbers of different strength. The light emitted from the sample was collected using the assembled objective, guided through the microscope optics and detected with a room temperature CCD camera.

Bias– & pH–dependent PL

With the measuring configuration described above it is possible to measure the luminescence of the sample while it is electrically contacted via an electrolyte. Optical excitation as well as detection of the sample luminescence is performed through the electrolyte. Within the three electrode configuration (cf. Figure 3.2) it is possible to control the surface potential V_S and record the luminescence in dependence of the applied bias. The applicable potentials are only restricted by the decomposition voltage of the used electrolyte which is ± 1 V for water. With the help of the peristaltic pump the PL of the sample could be used to record transient pH changes within the electrolyte.

3.5. Ionic Liquids

For measurements with non–aqueous electrolytes like ionic liquids, a specific chamber was constructed. As the contamination with water significantly influences the measurements specific care concerning the insulation was taken. A schematic of the measurement chamber is depicted in Figure 3.11. The three used electrodes are namely an Ag/AgCl electrode (DriRef 500 ,World Precision Instruments INC., Sarasota, U.S.A.) as reference, and a Pt–stiff electrode as counter electrode, and the sample as working electrode. A quartz glass window is placed directly above the sample for optical excitation and detection through the objective comparable to the setup described in section 3.4.1. To minimize the contamination during the experiments, the whole construction is sealed with O–ring to maintain a minimum of

flexibility concerning the sample size.
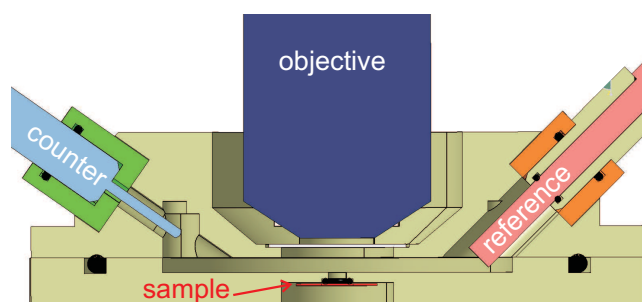
Figure 3.11.: Schematic of the experimental setup used for PL measurements of ILs in a three electrode configuration.

To assure a contamination–free injection of the IL into the chamber, the whole mounting process was performed in inert atmosphere in a glove box. For the actual measurements the reference electrode was immersed just before the measurement was started. The volume of the used IL was ≈ 12 ml. The water fraction was measured to 70 ppm prior to the experiments [93].

It has to be noted, that the application of IL requires much care taken about the purity. The fact that an Ag/AgCl electrode is used as reference is problematic for long term experiments with a water–free IL. Nevertheless for purely qualitative measurements their use is not problematic.

Electrochemical Characterization of Gallium Nitride Nanowires

This chapter deals with the electrochemical characterization of GaN NWs. As a first step in the NW characterization the n– and p–type silicon substrates were evaluated.

N.i.d. GaN NWs were examined by Impedance Spectroscopy (3.3.2). The results were compared to those obtained for different Si– (n–type) and Mg (p–type) doped NWs (4.2.2) on the basis of their extracted electrical properties. According to these data the NW diameter in relation to the doping level is discussed as a crucial factor in determination of the electrical properties (4.2.3).

In the following, a model is presented that allows a discrimination of the NWs in two classes namely resistive and conductive. It is supported by the evaluation of bias dependent measurements (4.3.2) and cyclic voltammetry measurements which indicate the occurrence of charge transfer processes (4.3.1).

4.1. Reference Measurements with Silicon Substrates

All measurements presented in the following were performed in the three electrode measuring geometry described in chapter 3.2 with appropriate sample mounts in an opaque faraday cage. The electrolyte was $10\,\text{mM}$ PBS if not mentioned otherwise. For clarity only the absolute impedance vs frequency part of the Bode–plots (cf. Figure 4.1) are shown and discussed.

As a first step, the electrochemical properties of GaN thin films are analyzed. Then, the Silicon substrates and the interstitial step of nitridation (cf. section 3.1) are examined to be able to discriminate the influence from the substrate and the NWs.

The simple EEC model (model A) presented in section 3.3.2 is applied for the evaluation of the measurements. The value of R_0 is assigned to all parasitic resistances which is in the measurements dominated by an $1\,\text{k}\Omega$ resistor placed externally in series to the measuring cell to stabilize the spectrum in the high frequency domain ($> 10^4\,\text{Hz}$). The connected RC–element is interpreted in terms of surface capacitance

(C_S) and surface resistance (R_S).

In the initial steps of the GaN NW growth a thin layer of silicon nitride is formed on the silicon substrates (cf. section 3.1). To examine the influence of this nitridated interlayer n–type and p–type Si–substrates are measured before and after nitridation. The resulting IS recorded at $U_C = 0\,\text{mV}$ are almost identical exemplarily depicted for the n–type substrate in Figure 4.1 with the extracted electrical parameters denoted in Table 4.1. Due to the limited frequency range, the value of R_S is a lower approximation.
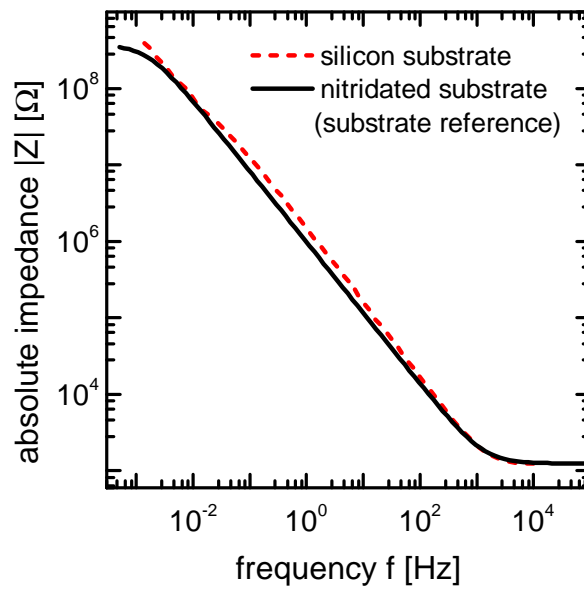
Figure 4.1.: IS of n–type Si substrate before and after nitridation.

sample type	R_S [MΩ cm^2]	C_S [μF cm^{-2}]	α	R_0 [kΩ]
n–Si	> 41	1.3 ± 0.2	0.99 ± 0.01	1.2 ± 0.1
p–Si	> 35	2.9 ± 0.2	0.99 ± 0.01	1.1 ± 0.1
nit. n–Si	29.1 ± 12.1	2.4 ± 0.5	0.97 ± 0.02	1.2 ± 0.1
nit. p–Si	15.8 ± 8.2	3.2 ± 0.3	0.97 ± 0.02	1.1 ± 0.1

Table 4.1.: Electrical parameter for differently doped Silicon substrates according to model A. The IS were recorded at $U_C = 0\,\text{mV}$.

For both substrates it is obvious that due to nitridation no significant changes occur. The slight decrease of R_S can be attributed to the removal of the native SiO$_2$ layer by etching in HF prior to the growth respectively the nitridation process. The slight increase of C_S can also be explained by the exchange of the dielectric layer

from SiO_2 to an amorphous nitride layer in analogy to a plate capacitor. This is in accordance with the increased permittivity of silicon nitride compared to SiO_2 [94].

The bias–dependent evolution of the electrochemical parameters R_S and C_S is presented and discussed in section 4.3.2 along with the bias–dependent IS of NW samples.

In the following discussion, the nitridated Si substrate is referred to as substrate reference.

4.2. Nanowires

At first the n.i.d. GaN NWs are measured and evaluated. Figure 4.2 shows Bode–plots of four IS recorded for cathodic bias between $U_C = 0\,\mathrm{mV}$ and $U_C = 600\,\mathrm{mV}$.
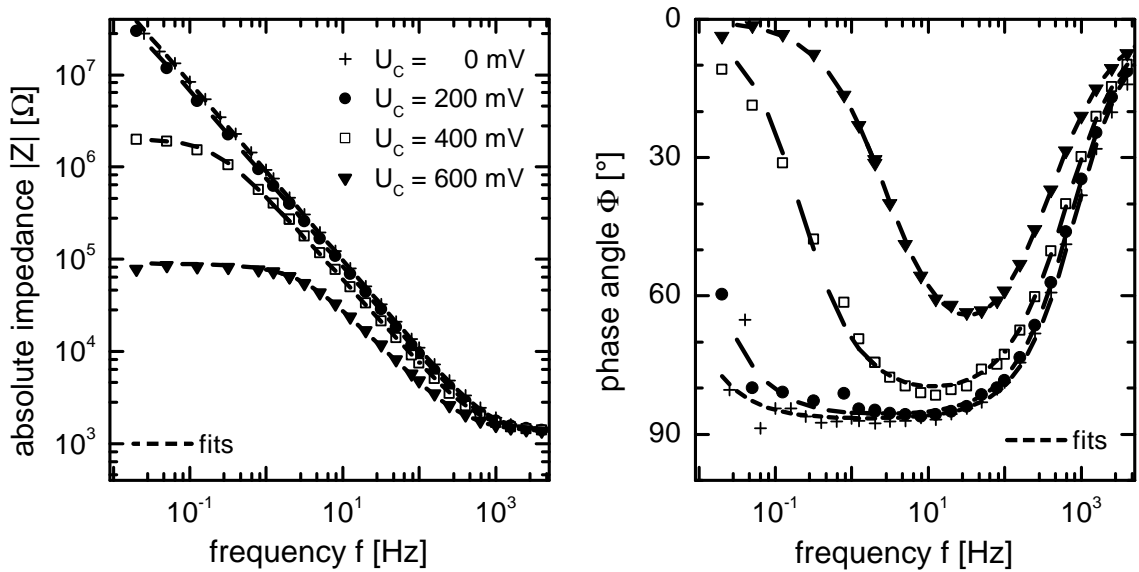
Figure 4.2.: Bode–plots of n.i.d. GaN NW ensembles with corresponding fits under various applied cathodic bias values.

A comparison of the results for the n.i.d. NW sample to those of the substrate reference reveals that the growth of GaN NWs does not significantly alter the extracted value for C_S $(2.2 \pm 0.3)\,\mu\mathrm{Fcm}^{-2}$, but causes a reduction of R_S to approximately $(19.8 \pm 8.1)\,\mathrm{M\Omega cm}^2$, half of its initial value (cf. Table 4.1). This can be attributed to the formation of leakage current pathways through the nitridated layer during NW growth.

4.2.1. Short Term Effects

In the beginning phase of the IS recordings, the spectra for the NWs are not reproducible. For all NW samples the electrochemical impedance spectra change significantly storage in ambient atmosphere at room temperature. In Figure 4.3 the development of recorded IS at $U_C = 0\,\text{mV}$ for a n.i.d. NW sample is shown for a series of multiple recordings. In alternation $U_C = 0\,\text{mV}$ ans $U_C = \pm 500\,\text{mV}$ are applied. The sample is regarded as stabilized when subsequent IS recordings at $U_C = 0\,\text{mV}$ produce identical spectra. The broken lines represent intermediate measurements at $U_C = 0\,\text{mV}$, indicating a gradual evolution toward the final, stabilized spectral shape. At the stabilized situation the extracted electrical parameters of the sample are constant.
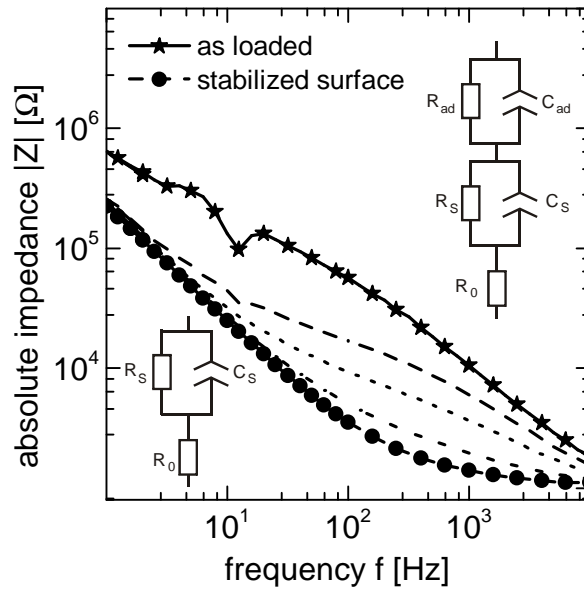
Figure 4.3.: Subsequent IS measurements at $U_C = 0\,\text{mV}$ for a n.i.d. GaN NW sample in PBS. Between the different recordings presented here, IS at $U_C = \pm 500\,\text{mV}$ were recorded.

For the evaluation of the non–stabilized spectra model B (cf. section 3.3.2) can be used to achieve reasonable agreement between a fit and the experimental data. The corresponding EEC consists of R_0 as the representative of all parasitic resistive effect which is also dominated by the used $1\,\text{k}\Omega$ resistor, the first RC–element with the interpretation of surface resistance R_S and surface capacitance C_S as described above and an additional RC–element (C_{ad}, R_{ad}) which in this case is attributed to adsorbates at the NW surface. For all spectra except for the lowest broken line and the stabilized spectra the effect of the second RC–element is quite prominent. In

case of the stabilized spectra the simple model A can be used for data evaluation, which indicates the complete removal of adsorbates during consecutive IS measurements with alternating bias. The number of measurements necessary to realize the stabilized shape of the IS depends on the storage time of the sample and on the applied bias voltages. Higher voltages accelerate the stripping process and result in a faster achievement of the stabilized IS. A direct quantitative evaluation of the IS is barely possible because of large α fluctuation for the RC–element attributed to the adsorbates.

The illumination with light $E_{exc} > E_g$ can also accelerate the stripping process as will be discussed in chapter 5.

4.2.2. Influence of Doping

In the following, the electrochemical characteristics of n.i.d. NW are compared to those of Si– or Mg–doped NWs. In detail three types of substrate dopand combination are examined. Si– and Mg–doped GaN NWs on n–type Si substrate and Mg–doped NW on p–type Si substrate.
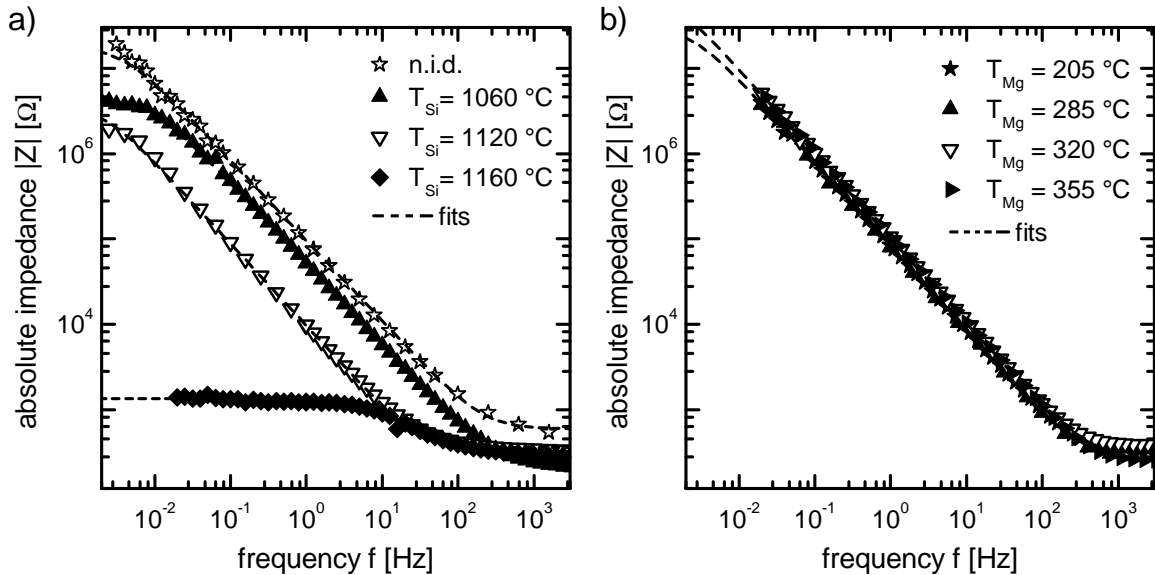

Figure 4.4.: Bode–plots for a) different Si–doped b) different Mg–doped GaN NW ensembles with fits corresponding to model A.

IS recorded for n.i.d. and differently Si–doped NW (Figure 4.4a) and Mg–doped (Figure 4.4b) grown on n–type substrates are displayed together with fits according to the EEC model A (cf. section 3.3.2) and Eq. 3.4. The extracted fit parameters are

summarized in Table 4.2 and related to the resulting BEPs of the Si– and Mg–effusion cell during the growth process.

sample	R_S [MΩcm^2]	C_S [μFcm^{-2}]	α	BEP$_\mathrm{Si/Mg}$ [mbar]
n.i.d. NW	19.8 ± 8.1	2.2 ± 0.3	0.95 ± 0.02	-
$T_\mathrm{Si} = 900°C$	11.5 ± 5.5	3.3 ± 1.2	0.94 ± 0.01	$4.0 \cdot 10^{-12}$
$T_\mathrm{Si} = 980°C$	8.7 ± 2.3	2.7 ± 0.3	0.95 ± 0.01	$1.8 \cdot 10^{-11}$
$T_\mathrm{Si} = 1060°C$	24.7 ± 21.5	3.5 ± 0.2	0.94 ± 0.02	$9.0 \cdot 10^{-11}$
$T_\mathrm{Si} = 1120°C$	1.0 ± 1.1	13.6 ± 6.9	0.90 ± 0.05	$3.0 \cdot 10^{-10}$
$T_\mathrm{Si} = 1160°C$	$1.1 \pm 0.2 \cdot 10^{-3}$	55.6 ± 31.2^a	0.73 ± 0.03	$7.0 \cdot 10^{-10}$
$T_\mathrm{Mg} = 205°C$	11.4 ± 4.3	1.8 ± 0.3	0.97 ± 0.01	$1.0 \cdot 10^{-11}$
$T_\mathrm{Mg} = 260°C$	12.1 ± 6.9	1.9 ± 0.4	0.96 ± 0.02	$1.7 \cdot 10^{-10}$
$T_\mathrm{Mg} = 285°C$	18.6 ± 2.2	1.7 ± 0.3	0.98 ± 0.01	$6.0 \cdot 10^{-10}$
$T_\mathrm{Mg} = 300°C$	37.4 ± 3.9	2.3 ± 0.9	0.96 ± 0.02	$1.2 \cdot 10^{-9}$
$T_\mathrm{Mg} = 320°C$	22.5 ± 2.9	1.3 ± 0.1	0.98 ± 0.01	$3.5 \cdot 10^{-9}$
$T_\mathrm{Mg} = 355°C$	26.3 ± 2.2	1.5 ± 0.1	0.98 ± 0.01	$2.8 \cdot 10^{-8}$

Table 4.2.: Extracted electrical parameters (R_S, C_S, α) of NW samples with the corresponding BEPs for Si/Mg during growth on n–type Si substrate. The large error bar results from uncertainties of ω_{max} in the capacitance correction according to Eq. 3.3.

The influence of silicon incorporation on the electrochemical properties of the NWs becomes evident by comparison of the IS presented in Figure 4.4 and the extracted fitting parameters in Table 4.2. An increasing T_Si during NW growth process is directly related to a decrease of the extracted value for R_S and an increasing value for C_S, as shown in Figure 4.5.

The results in Figure 4.5a show that, starting from a critical doping concentration reached for BEP$_\mathrm{Si}$ at $\approx 2 \cdot 10^{-10}$ mbar, C_S increases by more than one order of magnitude from (2.2 ± 0.3) μFcm^{-2} to (55.6 ± 31.2) μFcm^{-2} (cf. Figure 4.5a) whereas R_S shows a decrease from (19.8 ± 8.1) MΩcm^2 to (1.0 ± 1.1) MΩcm^2 (cf. Figure 4.5b), followed by a further decrease of more than two orders of magnitude for the highest Si concentration. Due to the normalization to the substrate area, which is in ensemble measurements only an approximation, the value for R_S tends to be underestimated while the value for C_S tends to be overestimated. As the observed variations in R_S are much stronger especially for the highest doped sample, this can be attributed to the presence of NWs and to Si–doping induced variations of the SBB.

In the case of Mg–doped NWs the doping induced effects on C_S and R_S are smaller
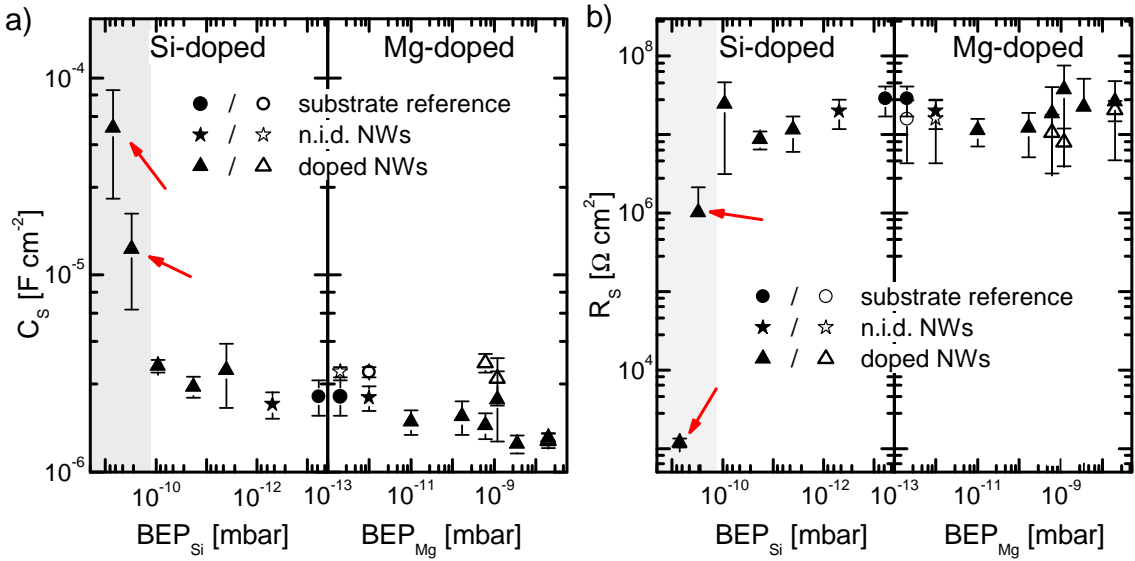
Figure 4.5.: Extracted electrochemical parameters a) C_S and b) R_S for n.i.d. doped, Si– and Mg–doped NWs and the substrate reference as a function of the BEPs during NW growth on n–type substrates (filled symbols) and on p–type substrates (open symbols). The samples used for evaluation of the flatband voltage in Figure 4.7 are marked by arrows.

compared to Si doped NWs. This is also valid for the usage of p–type Si substrate. The extracted values for the p–type Si substrate reference, n.i.d. GaN NW and differently Mg-doped NW ensembles are represented by open symbols in Figure 4.5.

With increasing Mg–concentration the value of C_S decreases slightly while R_S shows a minimal increase. Mg–doping leads to the compensation of the intrinsic and substrate related n–type doping within the NWs resulting in opposite effects on C_S and R_S as can be seen in Table 4.2.

Bias–dependent measurements revealed no transition to p–type conductivity while contrary measurements of the U_{OCP} indicate the existence of some kind of p–type region. This conflict can be explained with the lateral gradient of n–type background doping and the diameter dependence of the NWs. On the one side, the NW base region is highly Si– doped and barely influenced by Mg-doping, while on the other side the top region can be p–type.

The interplay of the NW diameter with the present doping concentration is of great importance for the determination of C_S and R_S and will be discussed in the next section.

4.2.3. Influence of the NW Diameter

In literature, some reports on the electrical properties of single GaN NWs in de-pendence of the NW diameter can be found. Calarco et al. [30] showed that for MBE–grown NWs the relation between diameter and a calculated critical diameter determines the photoconductivity and the dark conductivity. Under the assump-tion that the diffusion of Si from the substrate can be neglected, their calculations for n.i.d. NW yield the critical diameter in the range of $80 - 100 \, \mathrm{nm}$.

Below this critical diameter the NWs are completely depleted of free charge car-riers which implies that the SBB covers the whole volume of the NW. Above the critical diameter a small region in the center of the wire exists where no effect of the SBB is present (cf. section 2.1.1)

In ensemble measurements all contacted NWs participate to the measuring sig-nal. Due to the self–assembled growth, the NWs can exhibit diameter fluctuation of several tens of nm (cf. appendix A). These wire–to–wire variations broaden the overall influence of the NW diameter to a continuum. In the following interpre-tation, an average diameter of the examined NW ensemble is assumed. Because of the crucial dependence of the NWs properties on the diameter, the data in Figure 4.5 correspond to one specific growth series (series 1) for the respective dopant. In the following, the case of n–type doping with Si is discussed because Mg did not show significant influence on the electrical parameters.

For each single NW the local relation between the Si–doping concentration and the diameter determines the shape of the surface band bending and consequently the width of the depletion layer.

Figure 4.6a illustrates the influence of an increasing Si–doping concentration on the SBB in a NW (cf. section 2.1.1). For low Si–concentrations the NWs depletion width exceeds the diameter resulting in complete depletion of charge carriers and a low SBB [9, 95]. Such NWs can be considered as resistive. For a moderate increase of the Si–doping concentration the NWs remain depleted but exhibit a decrease of the depletion width and an increase in both the electric field in the depletion region and the SBB. For high Si–doping concentrations this results in a decrease of the con-duction band edge down to the bulk value $E_{C,B}$ within the NW diameter ($d_{\mathrm{crit}} > 2 \cdot W_{\mathrm{SCR}}$) and consequently to a field free region.

The impact of the NW diameter on the band profile, first discussed in reference [30], is summarized for a homogeneous and constant dopant distribution in Fig-ure 4.6b. An increase of the diameter above a critical value ($d_{\mathrm{crit}} > 2 \cdot W_{\mathrm{SCR}}$), which depends on the doping concentration, allows the formation of a field–free region
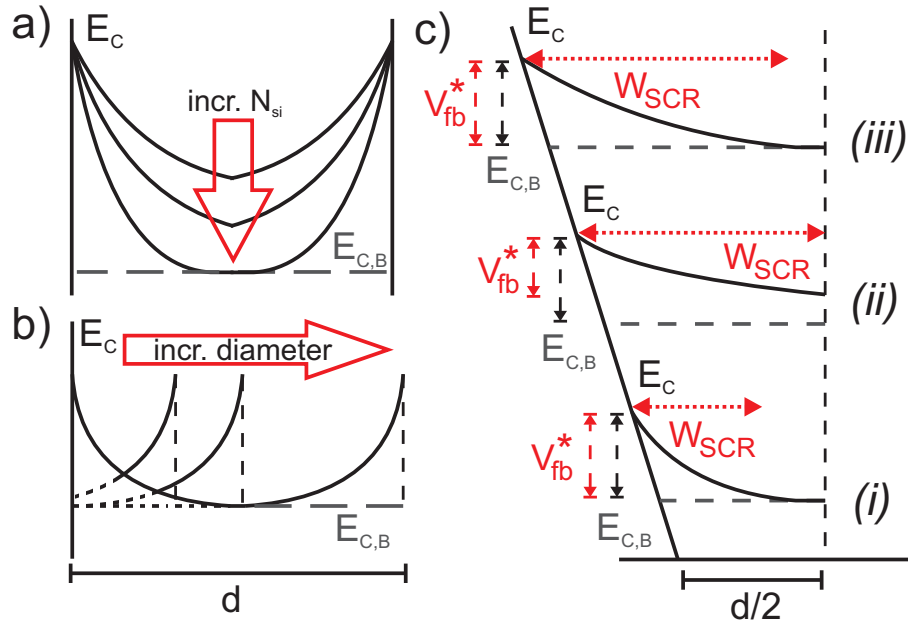
Figure 4.6.: Evolution of surface band bending using the example of the conduction band in GaN NWs for a) increasing Si–doping concentration b) different NW diameter [30] c) along a Si–doped GaN NW when both effects of a) and b) are taken into account.

defined by the conduction band edge at its bulk value $E_{C,B}$. Due to the cylindrical geometry this occurs in the center of the NW.

For a realistic description of the situation it has to be taken into account that due to diffusion from the Si substrate the Si–concentration in the bottom part of the NW is significantly higher than in the rest of the NW [14]. Furthermore, the high Si content related to the high T_{Si} during growth, the NW diameter increases along the c–axis [14]. Both effects have not been taken into consideration in earlier reports [30]. The resulting evolution of the conduction band profile along a highly Si–doped NW is schematically shown in Figure 4.6c. A small depletion width and the presence of carriers are found in the bottom part of the NW (i). If a homogeneous Si–concentration due to doping is assumed in the middle and upper part, the SBB increases along the growth direction, favoring the presence of carriers in the top part of the NW with a larger diameter (iii) while the middle part (ii) remains resistive. The corresponding effective barrier V_{fb}^* for electrons can be calculated according to Eq. 2.3.

Based on these considerations neither R_S nor C_S is expected to change significantly for low and medium Si concentrations. However, due to the higher Si content in the bottom part of the NWs, a conductive region can partially extend along the NW axis, resulting in an increasing C_S. If the depletion region is thin enough, tunneling

of electrons leads to a decrease of R_S.

With increasing Si–concentration, the resistivity of the NW middle section (cf. Figure 4.6c (ii)) decreases. Above a critical Si–concentration (cf. Figure 4.5, $BEP_{Si} > 2 \cdot 10^{-10}$ mbar) the total NW contributes to R_S and C_S, leading to the observed sudden increase of C_S and a decrease of R_S. A further strong decrease of R_S can be attributed to enhanced tunneling due to strong reduction of the depletion width and effective barrier especially in the bottom part of the NW.

As a distinct conductive region is assumed to exist in these samples, an effective ensemble average value for the magnitude of the SBB of the NWs can be obtained from the values for C_S extracted from the IS spectra for different bias by evaluation of the related Mott–Schottky plots, depicted in Figure 4.7. For the NW ensemble grown at $T_{Si} = 1120°C$ ($BEP_{Si} = 3 \cdot 10^{-10}$ mbar) and $T_{Si} = 1160°C$ ($BEP_{Si} = 7 \cdot 10^{-10}$ mbar) the values of (-960 $\pm$ 104) mV and (-205 $\pm$ 58) mV were obtained in PBS buffer at pH 7. For NW samples with lower Si–doping concentrations this method is not applicable because of the resistivity of the NWs. Due to the inhomogeneous Si distribution in the NWs and the variation of the NW diameter along the growth axis a straight forward assignment of the decreasing average SBB of the NW ensemble to a microscopic effect is not possible.
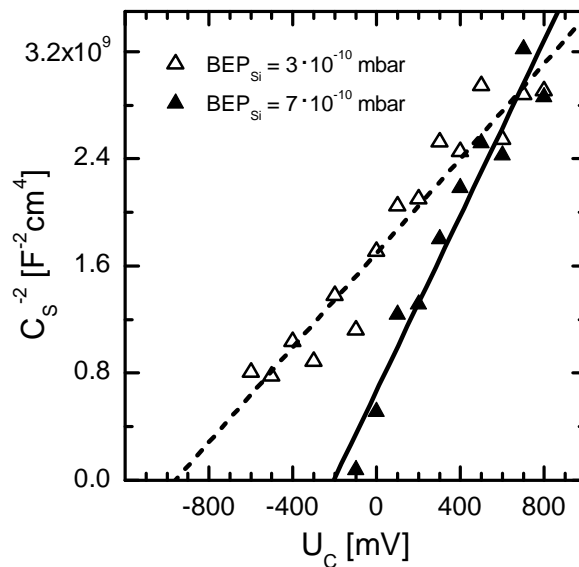

Figure 4.7.: Mott–Schottky plots of the in Figure 4.5 indicated samples. The values of the capacitance are corrected according to [91].

The weak influence of Mg–doping on the electrochemical characteristics in the investigated range is assigned to the compensation of residual donors by incorporated

Mg, resulting in an increased depletion width. In [96] the Mg–concentration of Mg doped GaN NWs was examined. This extracted Mg–concentration can be related either to the effusion–cell temperature during grown T_{Mg} or the $\mathrm{BEP}_{\mathrm{Mg}}$. From the results presented here it cannot be concluded whether a complete transition to p–type GaN NWs is achieved, as this would require a high Mg concentration due the high Si content close to the substrate. It has also been demonstrated in reference [96] that for Mg–concentrations of $10^{20}\,\mathrm{cm}^{-3}$ the formation of structural defects, that are very likely to inhibit p–type conductivity, is enhanced.

From the measurements it is apparent that the Mg–doping does not result in full p–type conductivity along the NW. Partial regions of p–type conductivity are likely for samples with higher Mg content as measurements of the U_{OCP} indicate.

4.3. Classification of NWs
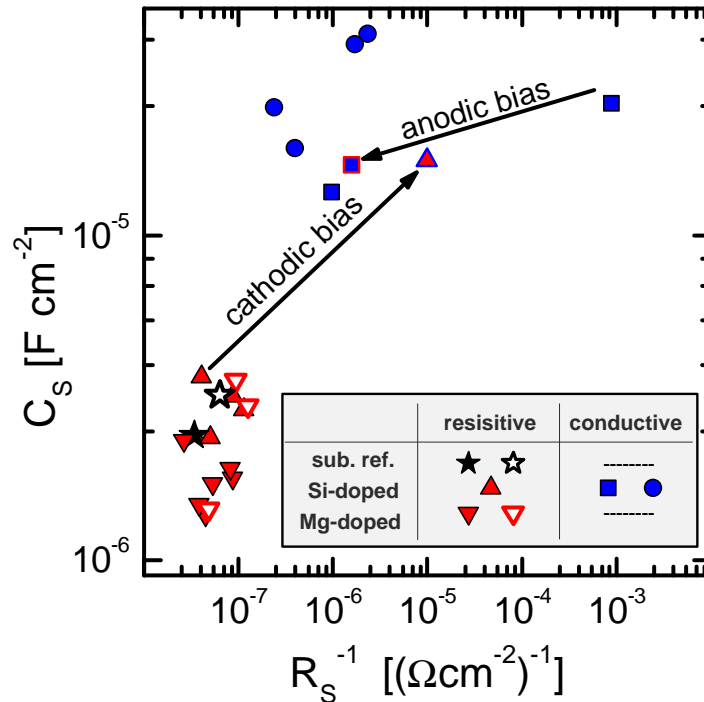
Figure 4.8.: GaN NWs can be classified in conductive and resistive according to the extracted values for R_{S} and C_{S}. N–type substrates are marked by full symbols while p–type substrates are represented by open symbols. The samples used in the bias–dependent measurements in the next section are indicated.

Following the analysis described above, the extracted electrochemical parameters R_S and C_S are not independent but form two groups, as depicted in Figure 4.8. Consequently, the NWs are classified as either *resistive*, consisting of n.i.d. , Mg–doped and moderately Si–doped NWs which are grouped around the substrate reference and characterized by low values for C_S and a large R_S. *Conductive* NWs, in contrast, are characterized by a higher value of C_S combined with lower R_S.

This assignment is confirmed by the analysis of a second series (series 2) of NW samples, grown at 5°C lower substrate temperature to increase the NW diameter to an average > 80 nm. In that case, following the analysis described above, the presence of a conductive region can be assumed for all Si concentrations. The same Si BEPs as for the first series were used during growth of the second series. Indeed, the extracted parameters for all of these NWs are located in the *conductive* regime as depicted in Figure 4.8 by blue circles.

The observation of charge transfer across the NW electrolyte interface into a redox couple present in the electrolyte could further support this classification. The measurements indicate occurring interfacial charge transfer only for the conductive GaN NWs.

4.3.1. Charge Transfer across the Interface into a Redox Couple

An adequate proof of the suggested classification of GaN NWs into *resistive* and *conductive* is possible by analysis of interfacial charge transfer into an appropriate redox couple. Figure 4.9 shows cyclic voltammograms of two *conductive* NW samples (T_{Si} = 1160°C) (series 1 (c)) and (T_{Si} = 1150°C) (series 2 (d)) in comparison to *resistive* NWs (T_{Si} = 980°C) as well as the substrate reference in a 1 mmol/l ferricyanide Fe^{2+}/Fe^{3+} solution, recorded at a scan velocity of v_{cv} = 100 mV/s. Full symbols represent measurements with the redox couple, whereas open symbols indicate measurements in pure PBS. For clarity, only the last cycle of a measurement series of 5 cycles is shown. The charging and discharging of the redox couple is clearly observable by two current peaks for the two presented *conductive* NWs.

In contrast, the *resistive* NW samples and the substrate reference do not show any charge transfer into the redox couple. These findings are regarded as another prove for the presence of carriers inside the resistive NWs and as well for the interfacial transfer which is facilitated by a reduction of the depletion width due to Si–doping (cf. Figure 4.6).
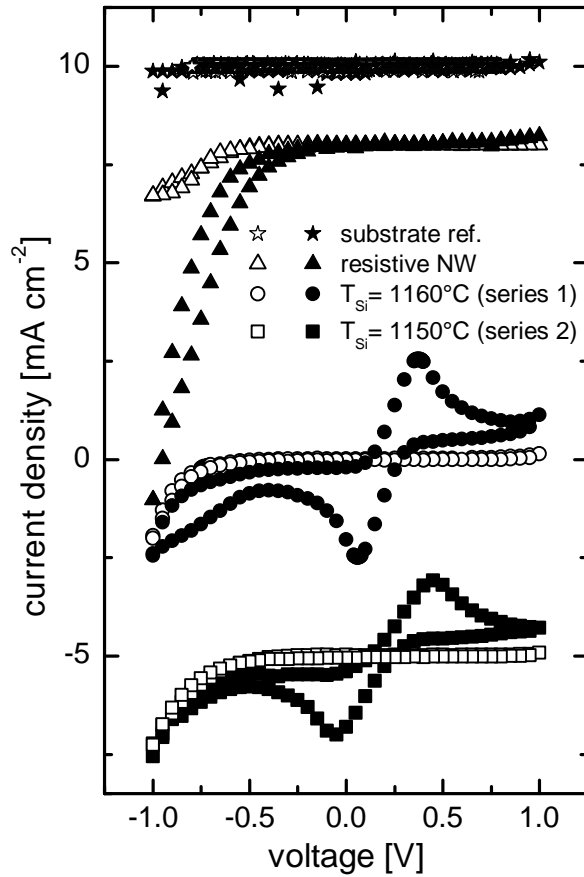
Figure 4.9.: Cyclic voltammograms for the n-type substrate reference, resistive NWs, $T_{Si} = 1160°C$ (series 1), $T_{Si} = 1150°C$ (series 2). Open symbols represent measurements in PBS buffer, filled symbols with the presence of Fe^{2+}/Fe^{3+} redox couple.

4.3.2. Influence of External Bias

A possibility to externally influence the band profile in the NWs is the application of an external bias via the electrolytic Schottky–contact as it was discussed in section 2.3.1.

As demonstrated for n.i.d. GaN NW above the application of an external bias has a direct impact on the SBB and consequently on the extracted electrical parameters in terms of R_S and C_S. Following the above presented model resistive wires can be made conductive (significant reduction of R_S) by the application of cathodic bias, while conductive wires can be depleted by anodic bias application.

Figure 4.10a shows the influence of an anodic bias between 0 and +600 mV on a conductive NW sample ($T_{Si} = 1160°C$) which is characterized by a thin depletion width but fully established SBB. The evaluation of the IS results in only minor de-

crease of C_S and an increase of R_S by more than three orders of magnitude.
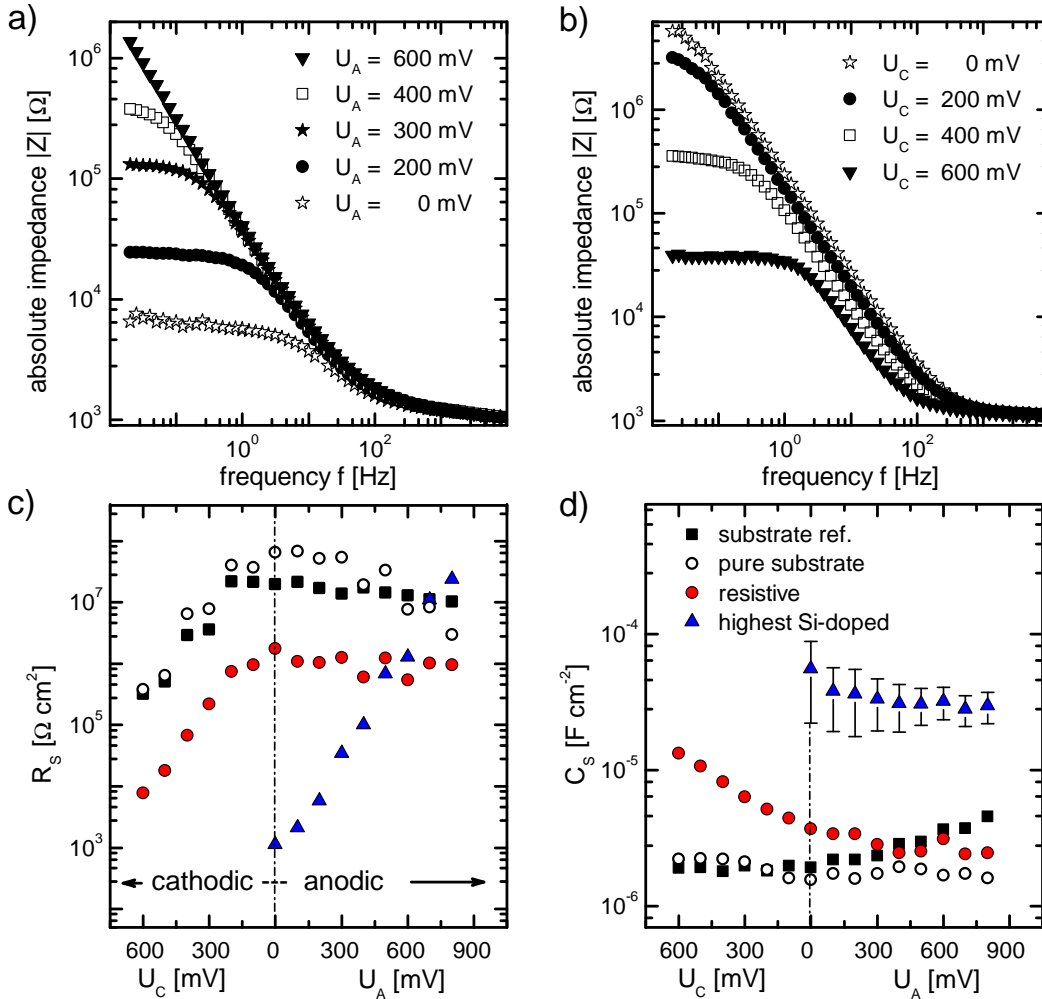

Figure 4.10.: Bode plots demonstrating the effect of external bias on IS of GaN NWs. a) Conductive NW sample with thin depletion width under anodic bias. b) Resistive NW sample under cathodic bias. Influence bias on the extracted values c) R_S and d) C_S, for the substrate reference, non nitridated substrate, resistive NWs and the highest Si–concentration NWs ($T_{Si} = 1160°C$). The large error bars for the highest Si–doped NW sample result from the uncertainty of ω_{max} in the capacitance correction according to Eq. 3.3.

On the contrary, resistive NW samples characterized by a less pronounced initial SBB respond to the application of cathodic bias between 0 and 600 mV with an increase of C_S by almost one order of magnitude and a strong decrease of R_S (by three orders of magnitude) as depicted in Figure 4.10b. While a comprehensive interpretation of the rather small capacitance variation is not possible based on the available experimental data and due to the limitations of the simplifies model the more pro-

nounced effect on the surface resistance can be attributed to an enhancement or reduction of the SBB within the NW with anodic or cathodic bias, respectively.

Figure 4.10c) and d) show the surface resistance R_S and the surface capacitance C_S extracted from the bias dependent IS presented in Figure 4.10a) and b) compared to results from the substrate reference and a non–nitridated n–type Si substrate.

A qualitatively similar behavior is observed for the bias dependence of R_S for substrates and resistive NWs. However, compared to the substrate reference the NW samples exhibit lower R_S values which becomes more pronounced with higher Si–concentrations and is attributed to additional leakage current pathways originating in the removal of the native oxide layer prior to NW growth or to spatial agglomeration of Si in the nitridated layer due to diffusion.

Both resistive and conductive NWs show a significant increase of R_S towards the anodic direction Figure 4.10c. However, for the highest Si–doped NW sample the absolute change of R_S is enhanced which may be attributed to the different initial SBB in the NW and an extended field free region within the NW. This is interpreted in the way that in the case of conductive NWs the total NW contributes to R_S resulting in stronger bias induced variations.

The bias dependence of C_S is presented in Figure 4.10d. Contrary to untreated Si surfaces (non nitridated substrate, open circles) the substrate reference (black squares) exhibits a behavior that is more typical for p–type substrates. This effect is detectable on both used substrates either n–type or p–type. Consequently, the effect is attributed to the existence of structural defects created during nitridation of the surface prior to NW growth. Removal of the Si_xN_y surface layer in diluted buffered HF restores the original behavior of the non–nitridated substrate.

In the case of resistive NWs (filled red circles), C_S is dominated only by the bottom section of the NW whereas the total NW contributes for the sample with the highest doping concentration, leading to no significant changes of the overall capacitance (blue triangles) as discussed above.

4.4. Summary

In summary, the electrochemical parameters (R_S and C_S) of n.i.d., Si–doped and Mg–doped GaN NWs grown on highly conductive Si(111) substrates were analyzed in a three electrode configuration and compared to the findings for the Si substrate.

The capacitance of the NW/electrolyte interface C_S can be increased by more than one order of magnitude by Si–doping, indicating the presence of free carriers in

doped NWs. In contrast, Mg–doping showed no significant influence on the electrochemical parameters of the examined GaN NWs.

Based on the extracted values for the interface capacitance C_S and for the interface resistance R_S a doping induced transition between two classes of NWs, resistive and conductive, is found. For conductive NW electrodes the interfacial charge transfer into the redox couple Fe^{2+}/Fe^{3+} without illumination is facilitated. Contrary to conductive NWs no charge transfer for the resistive class of NWs could be observed.

Application of an external bias allows the modification of the electrochemical properties (C_S and R_S) due to variations of the SBB. Resistive NW can be translocated into the conductive regime by application of a cathodic bias. Conductive NWs characterized by a thin depletion width become resistive under anodic bias.

In conclusion, the control of the dark conductivity by doping and external bias is an important feature for any electrochemical application of GaN NWs.

Photoelectrochemical Characterization of Gallium Nitride Nanowires

In this chapter, photoelectrochemical characterization of PAMBE–grown group III–nitride NWs is carried out by photoluminescence spectroscopy under controlled electrochemical conditions. The measurement setup is presented in section 3.4.1 and 3.4.2.

First, the photoluminescence response of n.i.d. GaN NWs to variation of the external bias and of the solution pH is studied. These findings are interpreted on the basis of an extended "dead layer" model for semiconductors. Accounting for the NW geometry several adjustments to the original "dead layer" model were necessary in order to apply it for GaN NWs.

In the scope of the extended "dead layer" model the interfacial charge transfer from a photo–generated hole across the interface is discussed as a weakening mechanism for the PL signal. The mechanism is further tested by the exchange of the water–based electrolyte PBS by an ionic liquid.

The analysis of Si– and Mg–doped GaN NW supports this model.

5.1. Photoluminescence of n.i.d. GaN NWs in an Electrolyte

The PL of GaN NW sample in contact with an electrolyte is recorded with the electrochemical measurement setup in a three electrode configuration (working, reference and counter) with the sample as working electrode as described in section 3.4.1. The NW sample were prepared as described in section 3.3.2. The parameters varied are the bias U_C between sample and reference electrode and the pH value of the electrolyte. Figure 5.1 shows two PL spectra recorded at the same n.i.d. GaN NW sample. The first PL spectrum is recorded under ambient atmosphere. The second is recorded while the sample is mounted into the flow chamber under floating po-

tential conditions in PBS at pH 7. Optics and laser excitation power are identical in both cases.
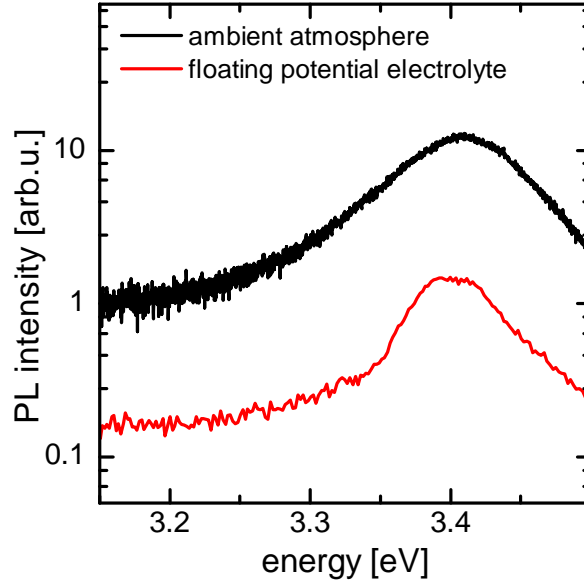

Figure 5.1.: PL spectra of a n.i.d. GaN NW sample under different ambient conditions.

Both spectra exhibit the GaN near band edge recombination peak at 3.4 eV with FWHM values of ≈ 110 eV (air) and ≈ 80 eV (electrolyte). The PL intensity recorded immersed into the electrolyte is one order of magnitude smaller compared to the air measurement due to scattering effects for the excitation and the emitted light.

Previous to bias– and pH–dependent PL measurements the open circuit voltage U_{OCP} is measured under UV–illumination in floating potential configuration in 10 mM PBS at pH 7.

Figure 5.2 shows the U_{OCP} for the sample examined in the scope of this work. All examined NW samples except of the two highest Mg–doped samples are characterized by a positive U_{OCP} pointing towards n–type conductivity of the samples. For the two highest Mg–concentrations, the negative U_{OCP} can either result from the correlated high defect density or from regions with dominating p–type conductivity. The NW sample with the highest Si–concentration shows a very small U_{OCP} of 24 mV. The exact origin of this effect remains unclear. It can be suggested that this drop in the U_{OCP} is related to a significant change in NW morphology due to the high Si content [14].

This value of U_{OCP} acts as a reference for the succeeding bias application. To avoid anodic oxidation and photo corrosion by photo–generated holes, the measurements are restricted to bias voltages on the cathodic side of the U_{OCP} and pH < 7.4.
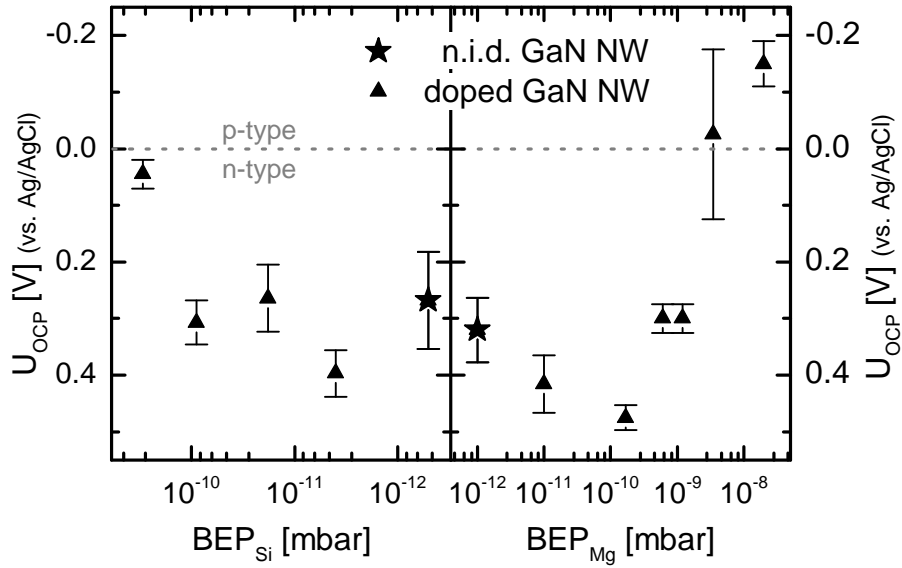
Figure 5.2.: OCP values for differently Si– and Mg–doped GaN NW samples under UV–illumination.

Intrinsic Luminescence of Water

It is known from literature [97] that pure water shows a luminescence peak at $\approx$ 3.4 eV when excited with UV–light ($E_{exc} > 3.5$ eV). The light source used for the excitation of the GaN PL in this work emits at $E_{exc} = 3.81$ eV. Therefore, water luminescence contributes a background signal that cannot be separated from the GaN luminescence at 3.41 eV at room temperature [27]. Figure 5.3a depicts PL spectra of n–type nitridated Si(111) substrates without NWs obtained at $U_C = 400$ mV and $U_C = 800$ mV. In both spectra the emission clearly originates from the water with its maximum remaining at approximately 3.39 eV with a bias–independent constant emission intensity.

Figure 5.3b) illustrates the superposition of the GaN band edge luminescence and the intrinsic water luminescence for a n.i.d GaN NW ensemle. The measurement at $U_C = 400$ mV reflects a spectral center at 3.39 eV while the PL spectra at $U_C = 500$ mV is slightly shifted to a higher energies at 3.41 eV. This can be attributed to the bias–dependent GaN luminescence superimposed to the water luminescence. Due to the difficult deconvolution of the water peak itself, a further examination of the overlay with the GaN luminescence is not possible.

The microscopic origin of this water luminescence is still under discussion. For the data interpretation in this work one has to keep in mind that due to this water luminescence, the GaN related luminescence at low bias voltages, especially for
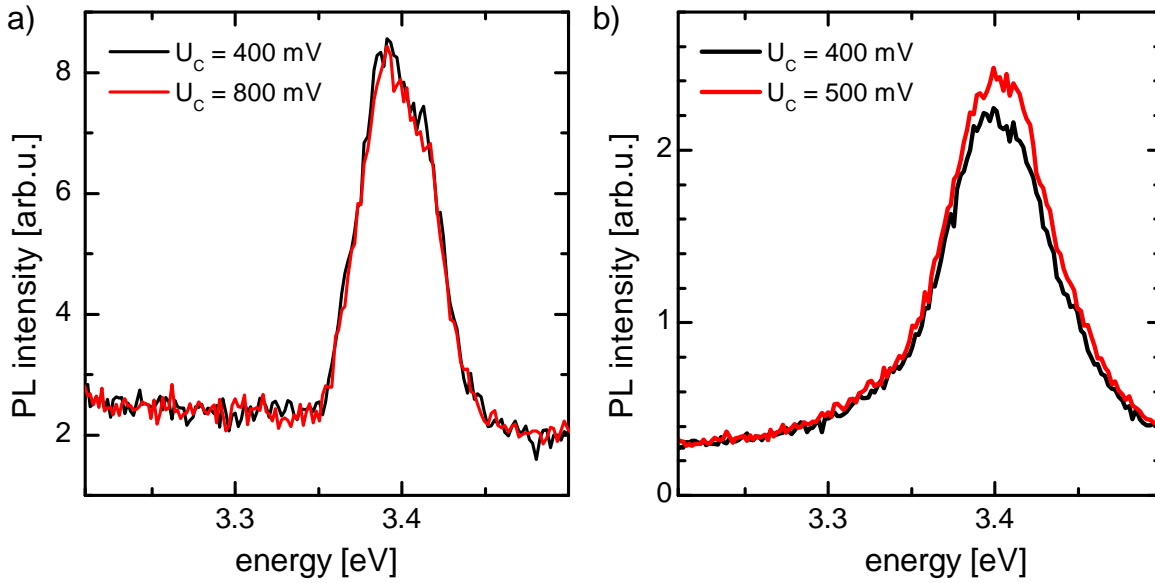
Figure 5.3.: a) PL spectra recorded of the substrate reference for $U_C = 400\,\text{mV}$ and $U_C = 800\,\text{mV}$. b) PL spectra of a n.i.d. GaN NW sample for $U_C = 400\,\text{mV}$ and $U_C = 500\,\text{mV}$ with the deconvolution into constant water and bias dependent GaN luminescence.

$U_C \approx U_{OCP}$, the intensity is overestimated. For Si–doped NWs, the water luminescence can be neglected because the PL at lower bias voltages is already significantly increased (cf. Figure 5.14b).

Bias–Dependence

The PL of a n.i.d. GaN NW ensemble depicted in Figure 5.1 was recorded under floating potential conditions. The application of an external bias $U_C > U_{OCP}$ directly influences the PL intensity.

Figure 5.4 shows the integrated PL intensity recorded for a Si–doped GaN NW sample grown at $T_{(\text{Si})} = 900°\text{C}$ at pH 7 and $U_C = 1000\,\text{mV}$. The four accentuated points mark the recording times of single PL spectra depicted in the insert at the same bias. The first recording shows a spectrum directly after immersion. The second PL spectra is recorded with a time delay of 10 minutes without further illumination. Note that the UV–illumination is only applied at the measuring spot (diameter $\approx 100\,\mu\text{m}$) during the recordings ($\approx 30\,\text{s}$). A slight increase of the PL is observable, due to stripping of adsorbates from the NW surface which is mainly defined by m–plane sidewalls. In succeeding transient measurements under continuous illumination with constant excitation intensity the trend of increasing PL signal becomes obvious. After 25 minutes, spectrum 3 was recorded. The overall intensity has increased

significantly. The recording of a further transient reveals only a minor enhancement of the PL intensity indicating a saturation of the response process. A change of the measuring spot reveals that the effect of increased intensity is restricted to the measuring spot.

This process is attributed to the UV–induced stripping of adsorbate comparable to the bias–induced stripping described in section 4.2.1 during IS. In the following experiments the sample was illuminated at the measuring spot previous to the actual measurements.
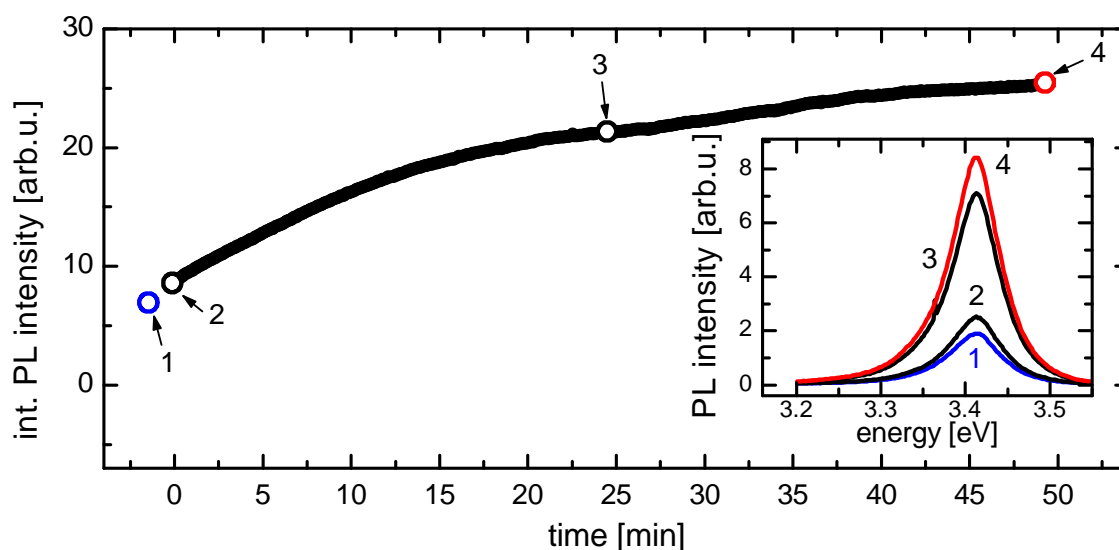

Figure 5.4.: Transient PL intensity recorded at $U_C = 1000\,\mathrm{mV}$ at pH 7 at the identical position. The insert shows the PL spectra corresponding to the given times.

In Figure 5.5a the PL spectra of another n.i.d. GaN NWs at pH = 7 for different cathodic bias $U_C > U_{OCP}$ are depicted. The PL spectra are dominated by the band edge recombination at 3.41 eV [14]. No change of emission energy or peak width is detectable when the bias is altered.

An increasing PL intensity is found for increasing cathodic bias values. The PL intensity increases by almost two orders of magnitude for a cathodic bias of 1200 mV. The insert of Figure 5.5a shows the integrated PL intensity of the spectra normalized to the PL signal intensity at $U_C = 500\,\mathrm{mV}$.

Additionally, Figure 5.5b shows the transient response of the PL intensity for voltage steps ranging from $U_C = 400\,\mathrm{mV}$ to $U_C = 1000\,\mathrm{mV}$ and back with step size of 50 mV at pH 7. Each voltage step was applied for two minutes. The voltage pulses are clearly reproduced by the PL intensity curve for $U_C > 700\,\mathrm{mV}$. For lower bias the
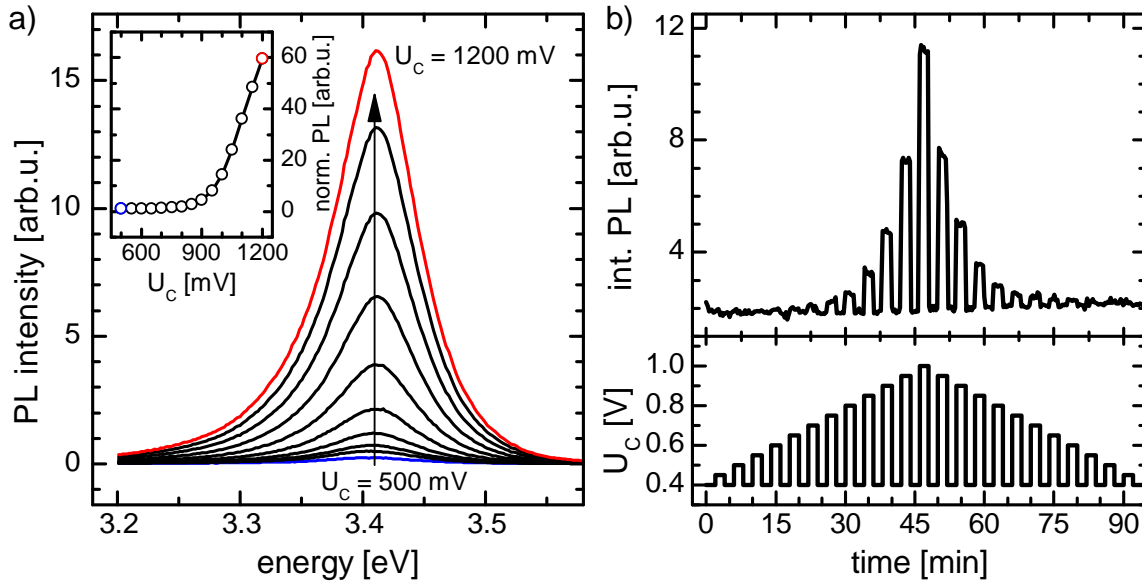
Figure 5.5.: a)PL spectra of n.i.d. GaN NWs for U_C between 800 and 1200 mV in steps of 50 mV at $U_C = 500$ mV and pH 7. The insert shows the integrated PL intensity of the spectra between 3.35 and 3.45 eV as a function of the applied bias. b) Transient changes of the integrated PL intensity for voltage steps ranging from $U_C = 400$ mV up to $U_C = 1000$ mV and back with step size of 50 mV at pH 7.

resolution at pH 7 for the given illumination intensity is not high enough to resolve the bias steps.

In general, the PL transients were recorded at a slightly increased excitation intensity with a spectral resolution of one second compared to the recording of single spectra.

pH–Dependence

In order to assess the influence of pH variations on the characteristics of the NW PL, the measurements have to be performed under well–defined electrochemical potential conditions achieved by a constant applied U_C. In Figure 5.6a, seven PL spectra of n.i.d. GaN NWs at $U_C = 500$ mV for different pH values are depicted. An increasing PL intensity with decreasing pH is found while the emission energy and the FWHM of the emission peak remain unaffected.

The insert of Figure 5.6a shows the integrated PL intensity of the corresponding spectra as a function of the solution pH. The integration was performed in the range between 3.35 and 3.45 eV.

Figure 5.6b shows a transient measurement of the PL intensity of a n.i.d. NW
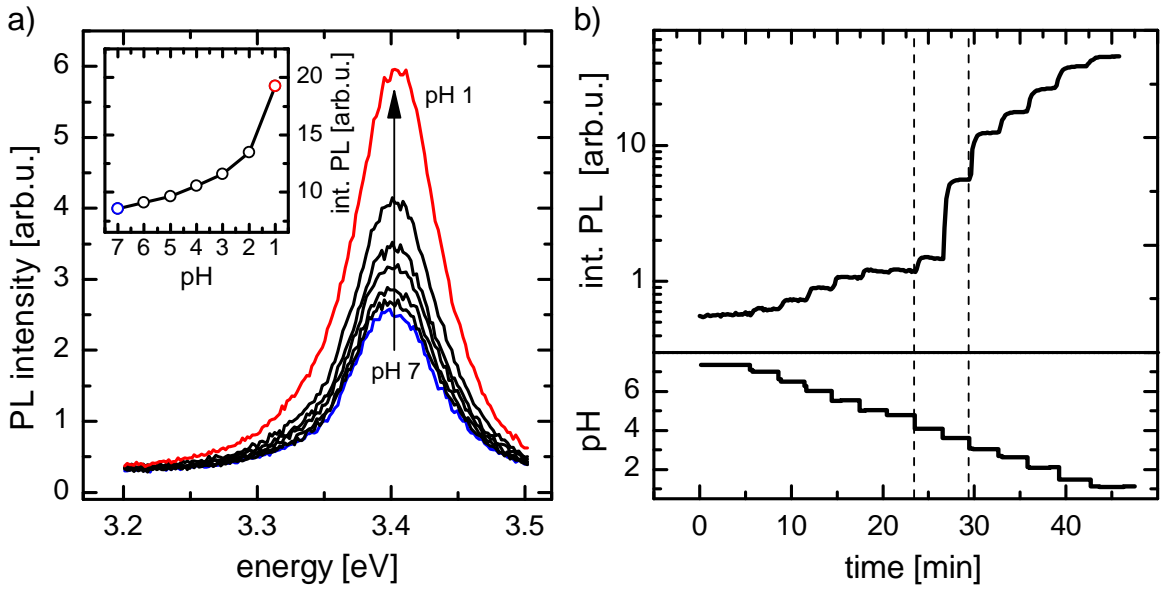
Figure 5.6.: a) PL spectra of n.i.d. GaN NWs between pH 7 and pH 1 at $U_C = 500\,\text{mV}$. The insert shows the integrated PL intensity of the spectra between 3.35 and 3.45 eV as a function of the solution pH. b) Transient measurement of the PL for titrated pH changes between pH 7 to pH 1.1 in steps of ≈ 0.5 pH at $U_C = 800\,\text{mV}$.

sample while the pH is decreased stepwise ($\approx 0.5\,\text{pH}$ each step) starting at a value of 7.4 down to pH 1.1.

The shape of the recorded PL transient clearly resembles the pH titration steps. The small time delay between the measured pH change and the corresponding PL intensity change is directly related to the tube length between electrolyte reservoir and the pumping speed as indicated exemplarily by two broken lines in Figure 5.6b. Comparing the shape of the pH–dependent PL in the insert of Figure 5.6a with the transient in Figure 5.6b the qualitative reaction of the PL intensity to pH reduction is the same, but the magnitude varies significantly. This effect can be attributed to inhomogeneities among the NWs related to the self–assembled growth process appendix A.

Combined Bias and pH Dependence

Comparison of Figure 5.6 and Figure 5.5 reveals that a decrease of the electrolyte pH leads to a qualitatively similar change of the PL characteristics as an increase of U_C. This points towards the same mechanisms being involved in the observed PL intensity changes.

Figure 5.7 shows the normalized integrated PL intensity as a function of U_C for dif-

ferent pH values between 7 and 1 for a n.i.d. GaN NW sample. The pH–dependent bias curves all resemble a s–shape. The more acidic the pH value the lower the on-set cathodic voltage of the curve. In the following, these curves are referred to as calibration curves.
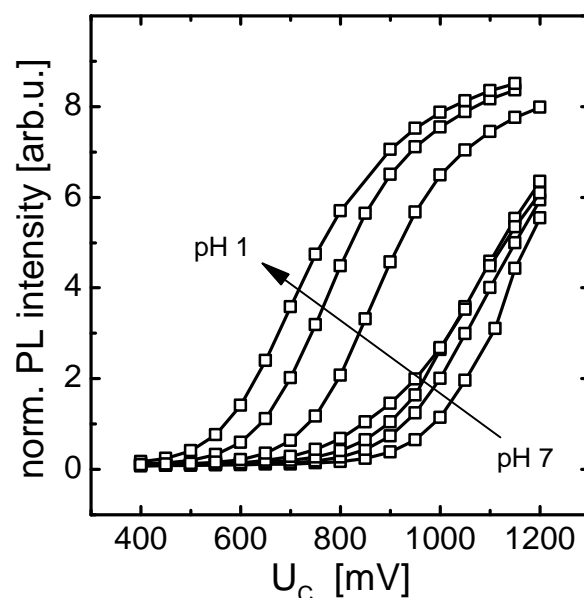

Figure 5.7.: The normalized integrated PL intensity (between 3.35 and 3.45 eV) as a function of the applied cathodic bias U_C for different pH values between 7 and 1. In the following, these curves are referred to as calibration curves.

This bias–dependence of the pH response offers the possibility for electrochemical definition of a working point with optimized pH–sensitivity and PL intensity.

Under consideration of the pH induced shift of the PL intensity between 40 and 90 mV/pH which is in good agreement with the reported pH–dependence of the surface potential of c–plane GaN layers [98, 99] a bias variation of 1 mV corresponds to differences in pH of 0.01 to 0.03.

5.2. The "Dead Layer" Model

In the following section, the pH and bias dependence of GaN as a semiconductor are discussed in terms of the "dead layer" model. It describes a thin layer beneath the surface of a semiconductor characterized by the presence of electric fields where no radiative recombination occurs. This is explained by the spatial separation of electron and hole caused by the the electric fields. In case of a present "dead layer", charge carriers can recombine radiative only directly at the surface or the field–free

region.

Based upon the first examination of such an optically "dead layer" in cathodoluminescence experiments from Wittry et al. [100], the model was also verified with other experimental methods e.g. PL. The extension of the dead layer in a semiconductor with bias application across a Schottky–contact and the corresponding quenching of the luminescence signal was evaluated by several groups [101, 102, 103]. Hetrick et al. [101] examined a CdS/Au schottky barrier diode and found a decrease of the PL intensity with increasing anodic bias and attributed this to an increase in spatial extension of the space charge region W_{SCR} (cf. section 2.3.1).

The concept was extended to the semiconductor/electrolyte interface by Smandek et al. and Chmiel et al. [104, 105]. They assumed that at the semiconductor/electrolyte interface similar to a semiconductor/metal interface an optical dead layer on the semiconductor side is formed.

In general, the illumination of an n–type semiconductor/electrolyte interface with light with $E_{\text{exc}} > E_{\text{g}}$ leads to the generation of electron–hole pairs (cf. section 2.1.2). Recombination can occur accordingly to three different mechanisms, as depicted in Figure 5.8 [105].

I The radiative band edge recombination of an electron with a hole under photon emission in the field–free region of the semiconductor.

II The non–radiative recombination of an electron with a hole in the bulk or at the surface via surface states.

III The charge separation (transfer) of an electron or a hole across the interface into a redox system present in the electrolyte. This transfer can also be mediated by surface states.

In general, for a n–type semiconductor, the strength of the PL signal depends on the availability of minority charge carriers (cf. section 2.1.2).

For the bulk of a n–type semiconductor, the minority carrier density $p(x)$ under illumination, at assumed flatband conditions and the absence of non–radiative recombination pathways via surface states (Figure 5.8 II) or interfacial charge transfer (Figure 5.8 III), can be calculated according to Eq. 5.1 [105].

$$p_{(x)} = \frac{\alpha L_h^2 I_0}{D(1 - \alpha^2 L_h^2)} \cdot \left(e^{-\alpha x} - \alpha L_h \cdot e^{-\frac{x}{L_h}}\right) \tag{5.1}$$
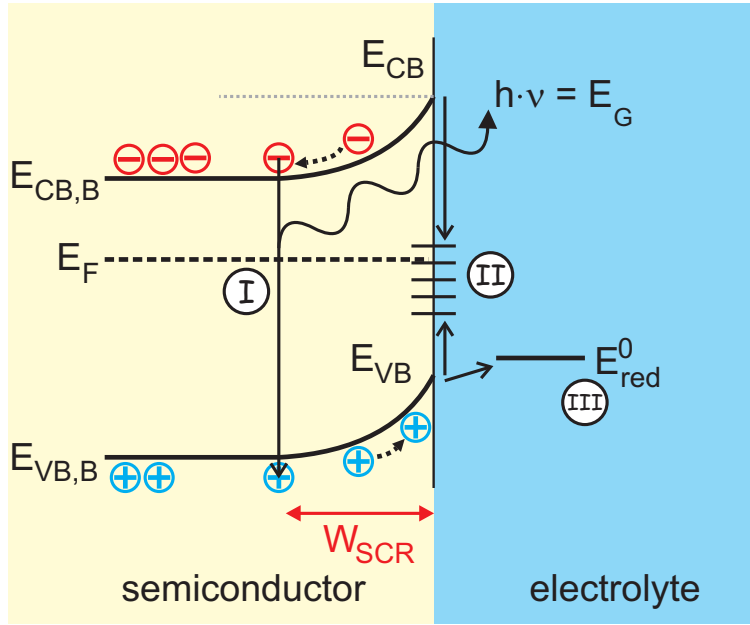
Figure 5.8.: Recombination mechanisms for photo–generated electron–hole pairs. (I) Band edge recombination in the field–free bulk region with photon emission. (II) Non–radiative recombination via surface states. (III) Transfer into redox levels of the electrolyte. According to [105]

with the absorption coefficient of the semiconductor α, $L_h = \sqrt{D \cdot \tau}$ the mean diffusion length of holes, τ_h the hole lifetime, I_0 the illumination intensity and x the distance to the surface.

The first approach of Eq 5.1 formulated in [103] can be extended with the possibility of hole consumption at the surface by recombination and hole diffusion to the bulk to Eq. 5.2.

$$p(x) = \frac{\alpha \cdot \tau_h \cdot I_0}{1 - \alpha^2 L_h^2} \cdot \left(e^{-\alpha x} - \frac{\alpha L_h + s}{1 + s} \cdot e^{-\frac{x}{L_h}} \right) \tag{5.2}$$

with

$$s = k_s \cdot \frac{L_h}{D} \tag{5.3}$$

$$k_s = k_{surface\ states} + k_{transfer} \tag{5.4}$$

s as a reduced recombination velocity that summarizes the possible loss processes for non–radiative recombination. $k_{surface\ states}$ and $k_{transfer}$ are the rate constants for the corresponding loss mechanisms via surface states or charge transfer. The values of τ_h and the rate constants are assumed to be concentration independent.

As the electron concentration in the bulk remains constant under illumination, the crucial parameter that determines the PL is the concentration of additionally

photo–generated holes. The total PL intensity can be calculated by integration of the minority carrier density or in the case of n–type doping the hole density $p(x)$.

$$Int_{PL} = \frac{1}{\tau_h} \cdot \int_0^d p(x) \, dx \tag{5.5}$$

Insertion of Eq. 5.2 into Eq. 5.5 and subsequent integration yield Eq. 5.6.

$$Int_{PL}^{fb} = \frac{I_0}{1 - \alpha^2 L_h^2} \cdot \left(1 - \alpha L_h \cdot \frac{\alpha L_h + s}{1 + s}\right) \tag{5.6}$$

According to Eq. 5.6 the PL intensity reaches its maximum for s = 0, implying that all photo–generated charge carriers recombine radiatively. It has to be noted that the PL intensity in this equation strongly depends on the solid state properties via L_h and α.

The situation changes to Eq. 5.2 when a SBB expressed by a space charge region W_{SCR} is present.

$$p(x, W_{SCR}) = \frac{\alpha I_0 \tau_h}{1 - \alpha L_h} \cdot \left(e^{-\alpha(x - W_{SCR})} - \frac{\alpha L_h + s_w}{1 + s_w} \cdot e^{-\frac{(x - W_{SCR})}{L_h}}\right) \tag{5.7}$$

with the boundary conditions

$$p(x = W) = 0 \tag{5.8}$$
$$s(x = W) \rightarrow \infty \tag{5.9}$$

According to Eq. 5.7 two different physical situations are important, $\frac{W_{SCR}}{L_h} \gg 1$ and $\frac{W_{SCR}}{L_h} \simeq 1$ defining the cases when all holes can reach the field free region outside W_{SCR} while $\frac{W_{SCR}}{L_h} \ll 1$ defines the case that all holes must recombine at the surface non–radiatively.

For a real semiconductor the relation between non–radiative recombination of charge carriers and the flatband potential is given according to [104] by Eq. 5.10

$$s = s^* \cdot e^{\left(\frac{U_{fb} - U_C}{k_B \cdot T}\right)} \tag{5.10}$$

which in combination with Eq. 5.6 leads to the normalized function of PL intensity Int(U_C) depending on the difference from the flatband potential $\Delta U_{fb} = U_{fb} - U_C$ and the non radiative surface recombination parameter s^*.

$$Int(U_C) = \frac{Int_{PL}^{fb}}{Int_{min}} = \frac{1}{1 - \alpha L_h} \cdot \left(1 - \alpha L_h \cdot \frac{\alpha L_h + s^* \cdot e^{\left(\frac{\Delta U_{fb}}{k_B \cdot T} \right)}}{1 + s^* \cdot e^{\left(\frac{\Delta U_{fb}}{k_B \cdot T} \right)}} \right) \tag{5.11}$$

Figure 5.9 shows simulations according to Eq. 5.11 for variations of the two parameters s^* (1, 5, 50 for U_{fb} = -100 mV) in a and U_{fb}[1] (-100 mV, -200 mV, -300 mV for s^* = 1) in b. In both cases an increasing value (the arrow points to the direction of higher values) leads to qualitatively similar behavior.
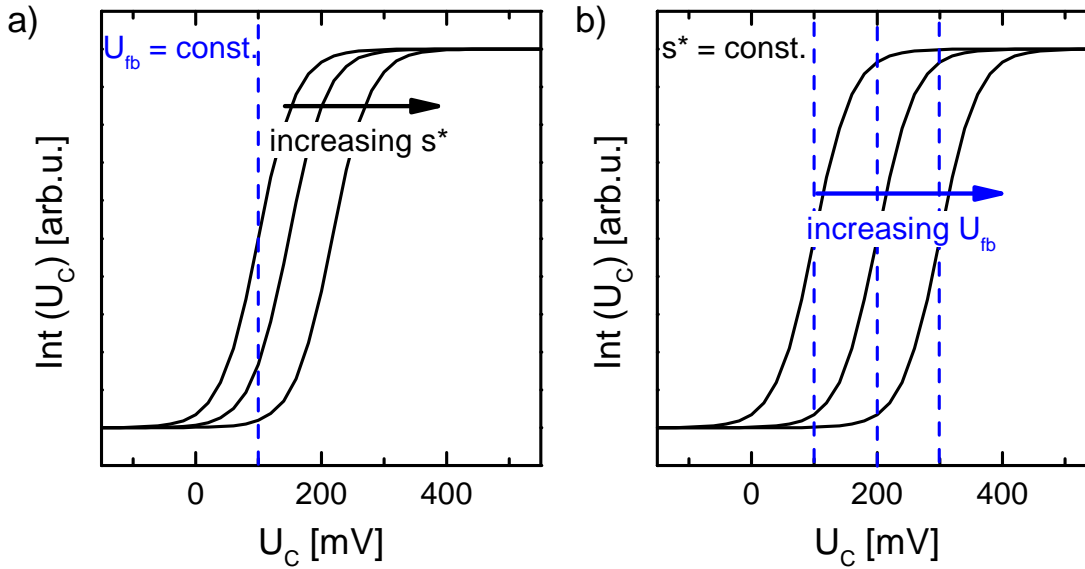

Figure 5.9.: Simulation of the PL intensity according to Eq. 5.11 for a n–type semiconductor for various values of a) s^* and b) U_{fb}. The arrows indicate increasing values of the modified parameters.

The PL intensity is at its minimum when all electron hole pais are separated allowing the holes to recombine non–radiatively at the surface. Increasing cathodic bias U_C compensates the SBB and the electric field defined by U_{fb}, responsible for the separation. As a result a higher value of requires a higher value of U_C applied to reach the same PL intensity. At a certain voltage U_C electron accumulate at the surface resulting in a full blocking of surface recombination. The PL intensity is at its maximum.

In the case of an increasing non–radiative surface recombination parameter s^* the required voltage to compensate the fast loss of the photo–generated holes is also increased. Higher values of s^* and higher values of U_{fb} lead to an identical shift of

---

[1]Note that in all Figures the value of U_{fb} is depicted with the opposite sign. This is necessary to stay in consistence with the definition of a positive cathodic bias.

the Int(U_C) function towards higher cathodic bias values.

5.3. Extended "Dead Layer" Model for NWs

In the following, the "dead layer" model is extended to NW geometry. Figure 5.10 schematically shows the PL intensity as a function of the applied cathodic bias U_C. The floating potential under illumination U_{OCP} and the flatband potential U_{fb} are marked for the case of n–type conductivity. In cathodic bias direction starting from the U_{OCP}, an increase of the PL intensity is expected due to compensation of the SBB (cf. section 2.3.1). This directly hinders two loss processes, the recombination of electron–hole pairs via surface states and the interfacial hole transfer which is possible due to the energetic positions of the GaN band edges in relation to the hydroxide ion OH^- (cf. Figure 2.6). Both loss processes cannot be examined separately in the experiments conducted in this work and are consequently discussed as one. The cylindrical symmetry of the NW implies that for a diameter $< d_{crit}$ the whole volume must be regarded as a "dead layer". The minimum of the PL intensity in this case is determined only by the intrinsic water luminescence (cf. section 5.1) in aqueous electrolytes.
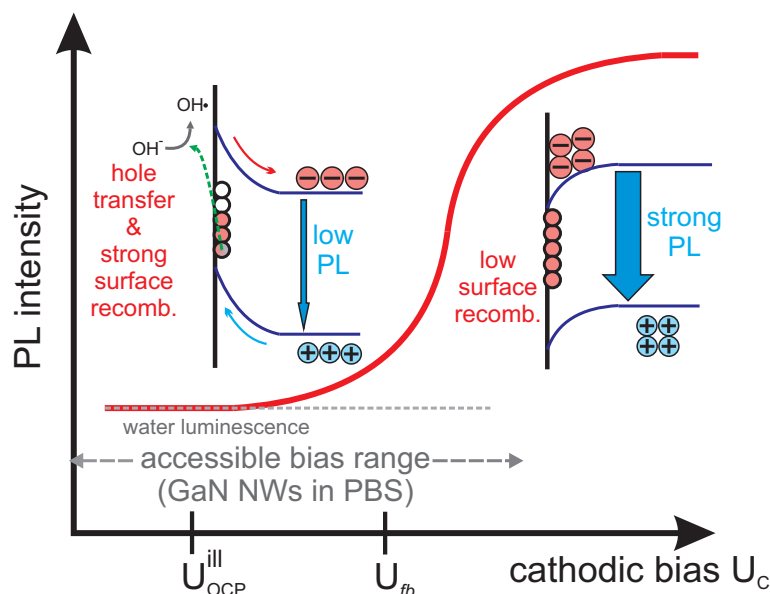

Figure 5.10.: The extended "dead layer" model relates the NW PL intensity to the applied cathodic bias U_C and adds interfacial charge transfer as a further non–radiative recombination processes.

For the application of the formalism presented in the "dead layer" model to the PL of the NW ensembles some adjustments are required. The parameters α (absorption

coefficient), τ_h (hole lifetime), L_h (mean diffusion length of the holes) are known for the case of layers. In NW geometry they can be different. In Eq. 5.12 this difference could be integrated by the insertion of a factor γ into Eq. 5.11 which includes all the changes in relation to the GaN layer values. It is assumed to be $\gamma > 1$. The best approximation to the experimental data is achieved for $\gamma = 6$. This value is closely related to the NW geometry and the doping concentration. In the case of other NW ensembles the value of γ must be adjusted.

$$Int_{PL}^{fb} = \frac{I_{min}}{1 - \gamma \cdot \alpha_L \cdot L_{L,h}} \cdot \left(1 - \gamma \cdot \alpha_L \cdot L_{L,h} \cdot \frac{\gamma \cdot \alpha_L \cdot L_{L,h} + s^* \cdot e^{\left(\frac{\Delta U_{fb}}{k_B \cdot T}\right)}}{1 + s^* \cdot e^{\left(\frac{\Delta U_{fb}}{k_B \cdot T}\right)}} \right) \tag{5.12}$$

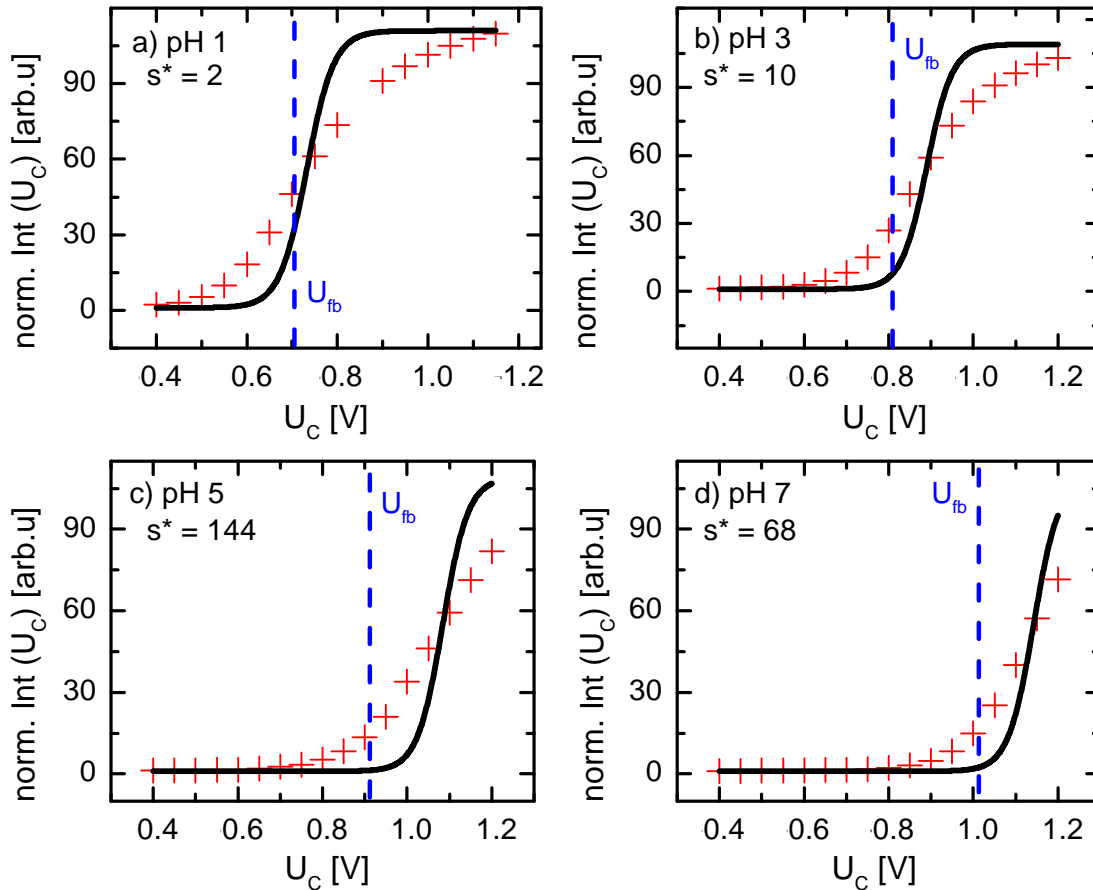Figure 5.11.: Integrated PL intensity for n.i.d. GaN NW sample normalized to the PL value at $U_C = 0.4\,\mathrm{V}$ with the fit according to Eq. 5.12.

In Figure 5.11, the integrated PL intensity is plotted for a n.i.d. GaN NW sample for the pH values of 7, 5, 3, and 1. As first step of the evaluation, the value of s^* in the case of pH 1 is assumed to have a low value (in this case $s^* = 2$). This seems

pH	U_{fb} [mV]	s*
7	-1016[+]	68
5	-935[+]	144
3	-821[+]	10
1	-707	2[+]

Table 5.1.: Values of U_{fb} and s* calculated according to Eq. 5.12. [+]Values that were assumed as constant in the fittings according Eq. 5.12.

reasonable because according to the site binding model in strong acidic solutions the surface hydroxyl groups are protonated (cf. section 2.3.4). The enhanced presence of positive charge at the surface is an effective barrier for photo–generated holes to reach the surface, leading to a reduction of both non–radiative loss processes. With the assumption of s* = 2 and γ = 6, the experimental data for a n.i.d. GaN NW sample can be fitted according to Eq. 5.12 at pH = 1 as depicted in Figure 5.11a. The fit yielded good agreement for U_{fb} = -707 mV.

In the following, this result is used as a reference to calculate the U_{fb} for the other pH values. Fixing the pH–induced variation of U_{fb} by assuming a similar shift as published for c–plane GaN layers of 57 mV/pH [98] the fit results for pH = 3, 5, and 7 yield a trend of increasing s*, i.e. stronger non–radiative recombination, with increasing pH s*(pH 3) = 10, s*(pH 5) = 144, s*(pH 7) = 68. Note that for pH 7 the fitting procedure underestimates s* due to the limited data range.

Thus, the overall qualitative shape of the Int(U_C) dependence is in agreement with existing theoretical model and the dependence on the pH value can be explained by pH dependent variations of the flat band potential and the resulting ratio of radiative and non–radiative recombination, expressed by the parameter s*. The extracted positions of the flat band potential are given in Table 5.1 and indicated in Figure 5.11a-d by the blue marks.

Figure 5.11 shows that this model predicts a much steeper variation of the PL intensity with U_C due to the assumption of a constant flat band potential U_{fb}. This is true for a layer but in the case of NW geometry the U_{fb} cannot be assumed as constant along the NW. From the results presented in chapter 4 it can be concluded that U_{fb} varies along the c–axis of the NW barely related to the doping concentration and the NW thickness. Especially for a thin n.i.d. GaN NW the U_{fb} is suspected to have its maximum value close to the bottom region of the NW followed by a decrease of U_{fb} towards the NW top. At the tip of the NW, only a minimum flat band voltage should be present. Since the precise dependence of the flat band potential

on the NW height represented by $U_{fb}(h)$ is unknown and complicated by wire–to–wire fluctuations it is approximated by an exponential decay $U_{fb}(h)$ along the c–axis with a characteristic decay length l along the c–axis according to equation 5.13.

$$U_{fb}(h) = U_{fb} \cdot e^{\left(-\frac{h}{l}\right)} \tag{5.13}$$

The combination of Eq. 5.12 with Eq. 5.13 results in Eq. 5.14. In the calculations an average height of the NWs is assumed to h = 700 nm.

$$Int(U_C) = \int_0^h \frac{1}{1 - \gamma \alpha_L L_L} \cdot \left(1 - \gamma \alpha_L L_L \cdot \frac{\gamma \alpha_L L_L + s^* \cdot e^{\left(\frac{-U_C - U_{fb} \cdot e^{\left(\frac{-h}{l}\right)}}{k_B \cdot T}\right)}}{1 + s^* \cdot e^{\left(\frac{-U_C - U_{fb} \cdot e^{\left(\frac{-h}{l}\right)}}{k_B \cdot T}\right)}} \right) \tag{5.14}$$
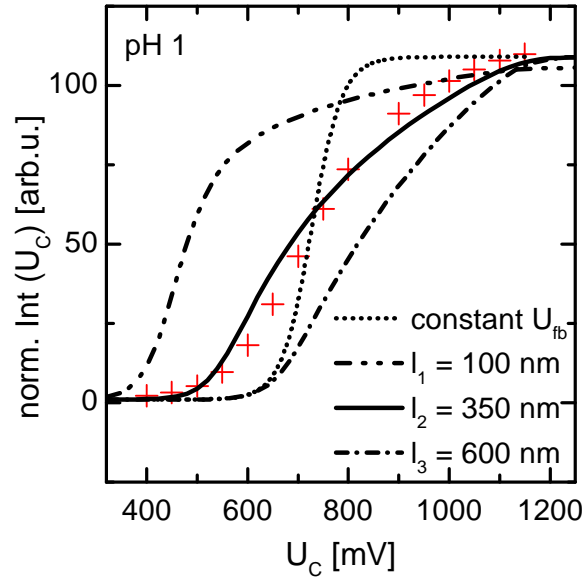

Figure 5.12.: Calibration curve for pH 1 with simulated $Int(U_C)$ according to Eq. 5.14 with different $U_{fb}(h)$ according to various l (Eq. 5.13) with an bias offset 420 mV.

This is calculated exemplarily for an exponential decay length l (l_1 = 100 nm, l_2 = 350 nm, l_3 = 600 nm), starting at assumed U_{fb} = -707,mV for pH 1. The calculations based on Eq. 5.14 yield the intensity plots depicted in Figure 5.12. Compared to the predicted evolution of $Int(U_C)$ with constant flat band potential (dotted line), the shape broadens significantly. The best agreement to the experimental shape is obtained for a decay length of l = 350 nm (full line). To match the experimental data,

the calculated curves need to be shifted along the U_C axis which can be attributed to an additional potential reduction related at e.g. the electrical contacts, the substrate/NW interface or within the electrolyte.

In Figure 5.13, the decay length $l_2 = 350\,\text{nm}$ is used for fitting further calibration curves of the n.i.d. GaN NW sample which is in the following referred to as *fitting 1*. The resulting calculated curves (black lines) show better conformance with the experimental data then with the assumption of a constant $U_{fb}(h)$ (dotted lines). The potential offset necessary to achieve best agreement with the experiments depends on the pH value (420 mV at pH 1, 504 mV at pH 3, 600 mV at pH 5, 680 mV at pH 7).
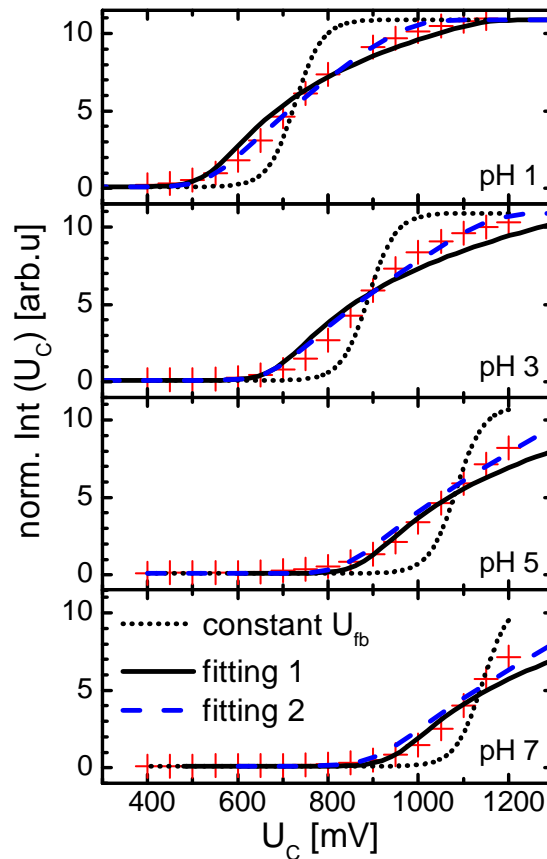

Figure 5.13.: Simulated PL intensity curves as a function of the applied cathodic bias. According to Eq. 5.12 with $l = 350\,\text{nm}$, with the corresponding bias offsets (420 mV at pH 1, 504 mV at pH 3, 600 mV at pH 5, 680 mV at pH 7) and according to a numerical fitting algorithm according to Eq. 5.14.

Under the assumption that no potential offset is required to fit the experimental data, another fitting approach is followed. A numerical fitting for all three free parameters of Eq. 5.14 (s^*, U_{fb}, l) is performed. The results of the fully numerical analysis are added in Figure 5.13 as blue broken lines and referred to as *fitting 2*.

pH	U_{fb} [mV]	s^*	l [nm]
7	-1310	490	1150
5	-1240	479	1100
3	-1070	34	1100
1	-985	1	1099

Table 5.2.: Values of U_{fb}, s^* and l used for the fitting according to Eq. 5.14.

Comparing both fittings, a slightly better approximation of the experimental data is achieved with the numerical analysis. The results of the numerical *fitting 2* are noted in Table 5.2. However, the extracted values for U_{fb}(h) and for the decay length of l = 1150 nm are not realistic, as this would imply the presence of a comprising high U_{fb} along the NWs axis, which is in contrast to the theoretical results in literature and the experimental data presented in chapter 4.

A possible reason for these controversial findings can be the presence of large local thickness fluctuations in the NW ensemble, as for a NW thickness above critical diameter of d $\approx$ 80 nm such values of U_{fb} might be explicable.

The dead layer model was formulated for a semiconductor with a homogeneous SBB and with illumination perpendicular to its surface. The transition to NWs with a variable SBB (cf. chapter 4) presents a different situation. The average height of the NWs is with $\approx$ 700 nm thicker than in the case of a layer structure. Following the Beer–Lambert law for the absorbtion the upper parts of the NWs will be accentuated.

The overall corresponding SBB region is defined by the NW height, at least for resistive NWs. Additionally, due to the average height of $\approx$ 700 nm of the used NWs, the weakening of the illumination intensity due to absorbtion (Beer–Lambert) is stronger then for layers. In sum this would lead to an accentuation of the upper parts of the NWs, which are represented by a low U_{fb}. Finally, this would result in a further broadening of the shape of Int(U_{C}).

In summary, it is obvious that a variation of U_{fb} along the NW as well as the lateral inhomogeneity of the NW ensemble have to be taken into account in order to obtain a comprehensive quantitative description. However, it is not possible without further experimental inputs to fully reveal the exact relation between the characteristic parameters with the data collected in the scope of this work. Nevertheless, the good agreement of the modified theoretical model of refs. [105, 104] with the experimental results confirms the proposed mechanisms.

5.3.1. Influence of Silicon Doping

To further confirm the proposed mechanism, Si–doped NW ensembles were also investigated. In that case the width of the "dead layer" due to the SBB is reduced, resulting in an increased potential barrier between the NW core and the surface (cf. Eq. 2.1). In Figure 5.14a the results for Si–doped NWs are compared to those of the n.i.d. NW ensembles and to a plain GaN layer. These results show that the doping–induced increase of the SBB [86, 106] results in a shift of the Int(U_C) characteristics to higher values of U_C. For the highest Si–concentration (BEP$_{Si}$ = $7\cdot10^{-10}$ mbar) the steep increase in Int(U_C) occurs outside the electrochemically accessible bias range for PBS.
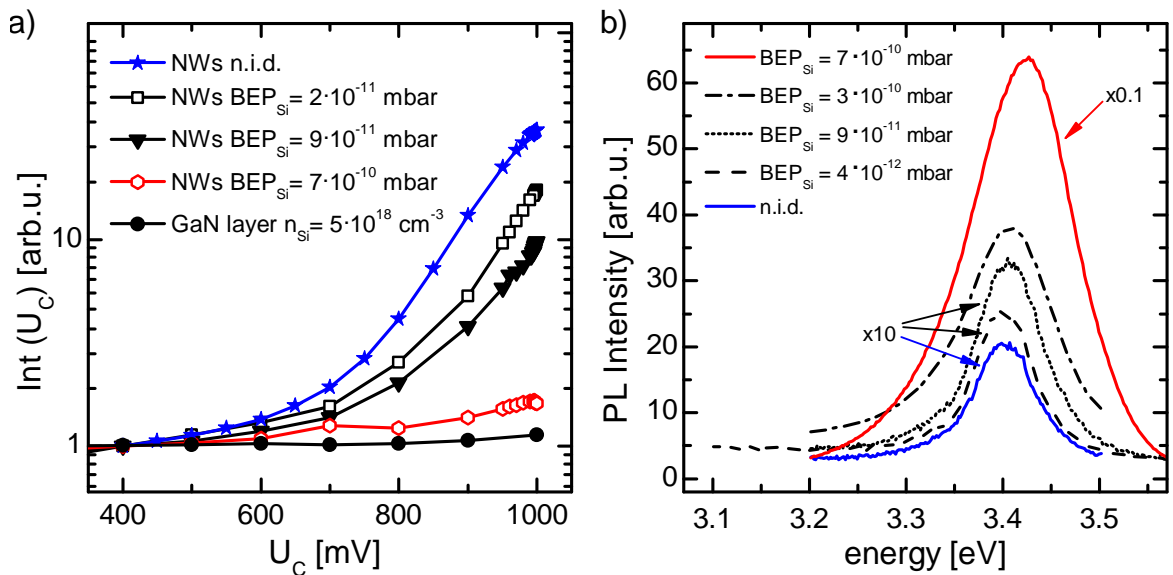

Figure 5.14.: a) Influence of Si–doping on the bias–dependence of the integrated PL intensity at pH 7. For better comparability the intensities are normalized to their value at U_C = 400 mV. Different Si–concentrations are indicated by their respective BEP$_{Si}$ values. Additionally, the response of a n–GaN substrate with a Si–concentration of n_{Si} = $5\cdot10^{18}$ cm^{-3} is shown. b) Influence of Si–doping on the absolute PL intensity at pH 7 for U_C = 400 mV. Different Si–concentrations are indicated by their respective BEP$_{Si}$ values.

The GaN layer shows a qualitatively similar behavior, however, the magnitude of the relative PL response within the achievable potential window is more than one order of magnitude smaller than for n.i.d. NWs.

The absolute PL intensity increases significantly with higher Si–concentration as depicted in Figure 5.14b and can be attributed to a larger NW center region. The

slight shift of the emission intensity with increasing Si–concentration was also ob-
served in literature [36] and can be attributed to the Burstein–Moss effects [32].

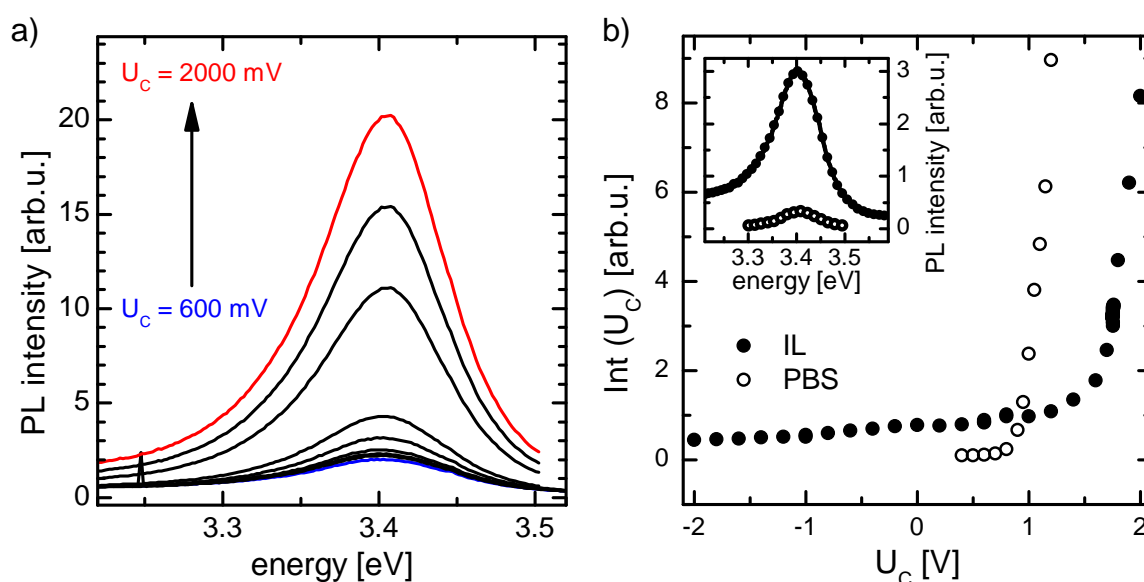## 5.3.2. Interfacial Hole Transfer

Figure 5.15.: a) PL Spectra recorded in IL of a n.i.d. GaN NW sample under various ca-
thodic bias values compared to measurements in PBS at a similar sample.
b) The calibration curves extracted from a) for the used IL and PBS at
pH 7. The insert in b) shows the PL spectra recorded at floating potential
in [EMIM][NTf$_2$] and 10 mM PBS with identical laser excitation.

A different approach to verify the importance of interfacial hole transfer is the use
of an electrolyte that is free of hydroxide ions, as provided by *ionic liquids* ILs, which
are non–aqueous electrolytes based on large asymmetric organic cations. When such
an electrolyte is in electrical contact with the NW surface the interfacial hole transfer
can not occur due to the absence of OH$^-$ ions.

Figure 5.15a shows the PL spectra recorded for a n.i.d. GaN NW sample in contact
with [EMIM][NTf$_2$] as electrolyte. Qualitatively the sample shows a similar behav-
ior as in PBS (cf. Figure 5.5). When comparing the PL recordings under floating
conditions it becomes obvious that the overall signal intensity from the sample con-
tacted with the IL is a factor six higher than for the same sample contacted with PBS
as depicted in the insert in Figure 5.15b. This can be directly related to the absence
of hydroxide ions OH$^-$ in the solution which effectively suppresses the interfacial
charge transfer of photo–generated holes to OH$^-$ ions. Instead, these holes are now

available for radiative recombination with electrons and contribute to the overall PL intensity. Independent of the electrolyte, non–radiative recombination via surface states can still occur and leads to a reduction of the PL intensity.

Following the same data evaluation as for PL spectra recorded in PBS, the calibration curve for the n.i.d. GaN NW sample in the IL is depicted in Figure 5.15b with the corresponding curve in PBS at pH 7. Comparing the two calibration curves, it is apparent that the onset potential for the by IL–contacted n.i.d NW sample is shifted to higher values of U_C compared to the PBS–contacted sample and that the lowest achievable PL intensity is by an order of magnitude higher in [EMIM][NTf$_2$] as electrolyte. A possible explanation for the potential offset can be found in the higher resistivity of the IL compared with PBS or, more probably, in the *liquid junction potential* (LJP) between the Ag/AgCl reference electrode which was used in this proof of principle experiment[2]. The LJP for the water/water–free organic solvents interface is part of extensive research. LJP comparable to the here presented Ag/AgCl/[EMIM][NTf$_2$] interface are in the order of 300 to 700 mV [107].

Besides this indirect method to determine the importance of the interfacial hole transfer on the GaN NW PL, a direct method can also be applied. In *electron paramagnetic resonance* (EPR) experiments we have recently shown, that the formation of the hydroxyl radical OH· occurs. The hydroxyl radical OH· is formed by transfer of a photo–generated hole from the GaN NWs into a hydroxide ion OH$^-$ under UV–illumination. A detailed description of the experiments and the results can be found in [108].

5.4. Summary

In summary, it was shown that the PL intensity of GaN NWs in electrolytes sensitively responds to the pH of the solution and the applied bias. Cathodic bias and a decreasing pH result in a strong increase of the PL intensity. This behavior was assigned to a reduction of the upward SBB that attenuates surface recombination and the transfer of photo–generated holes to redox levels of the electrolyte and thereby enhances radiative interband recombination in the NW. The resulting pH response strongly increases with higher cathodic bias and smaller pH, allowing the electrochemical definition of a working point with optimized sensitivity. It was demonstrated that for GaN NWs a resolution of better than 0.05 pH can be achieved for a

---

[2]The disadvantages of the water based Ag/AgCl reference electrode in contact with water free IL are well known but in this case of primary proof of principle experiments tolerated.

cathodic bias of 1000 mV around pH = 7.

To further confirm the presented extended "dead layer" model, the influence of Si–doping and the importance of the interfacial hole transfer into the hydroxyl radical were examined. For the latter a non–aqueous electrolyte is used. This additional findings reassure the proposed mechanism responsible for the pH– and bias–dependent luminescence of GaN NWs.

5.5. Influence of Mg–doping

In section 4.2.2, the characterization of Mg–doped GaN NWs showed that the existence of p–type regions is likely for high Mg–concentrations (cf. measured values of the U_{OCP} in section 5.1), although p–type conductivity cannot be is achieved for the complete NW.

As a consequence of the SBB in the n–type n.i.d. and Si–doped GaN NWs, the photo–generated holes can cause an oxidation at the surface. Due to the different SBB for p–type semiconductors (cf. section 2.1.1), which leads to an accumulation of photo–generated holes in the NW center, this reaction is attenuated. consequently, these NW can be assumed to be more stable even under basic pH values.

This section the first results of the photoelectrochemical characterization of Mg–doped GaN NW samples are presented. Figure 5.16a displays the PL spectra of five GaN NW samples with different Mg–concentrations recorded at RT in ambient atmosphere. The Mg–concentrations of these NW samples were analyzed directly by *secondary ion mass spectrometry* (SIMS) in [96].

For better comparability, all PL spectra are normalized to the peak–value of the GaN emission. With increasing Mg–doping a shoulder on the low–energy side of the GaN peak appears, corresponding to a second luminescence peak at an energy of ≈ 3.2 eV for $[Mg] = 1.3 \cdot 10^{19}$ cm^{-3}. Figure 5.16b shows the extracted peak positions from the PL spectra in Figure 5.16a as a function of the Mg–concentrations measured in [96]. The small red shift of the band edge emission for the highest Mg–concentration (red) is attributed to band gap renormalization. For the second peak a shift in the emission to lower energies is obvious for increasing Mg–concentration.

Power–dependent PL spectra were recorded for the Mg–doped NW ensemble with $[Mg] = 5.4 \cdot 10^{18}$ cm^{-3} in order to determine the origin of this second emission peak. Figure 5.17 shows 5 PL spectra recorded at RT in ambient atmosphere for different excitation intensities, ranging from 0.05 % to 5 %. This corresponds to a excitation power density of 2 Wcm^{-2} to 200 Wcm^{-2}. While the near band gap GaN
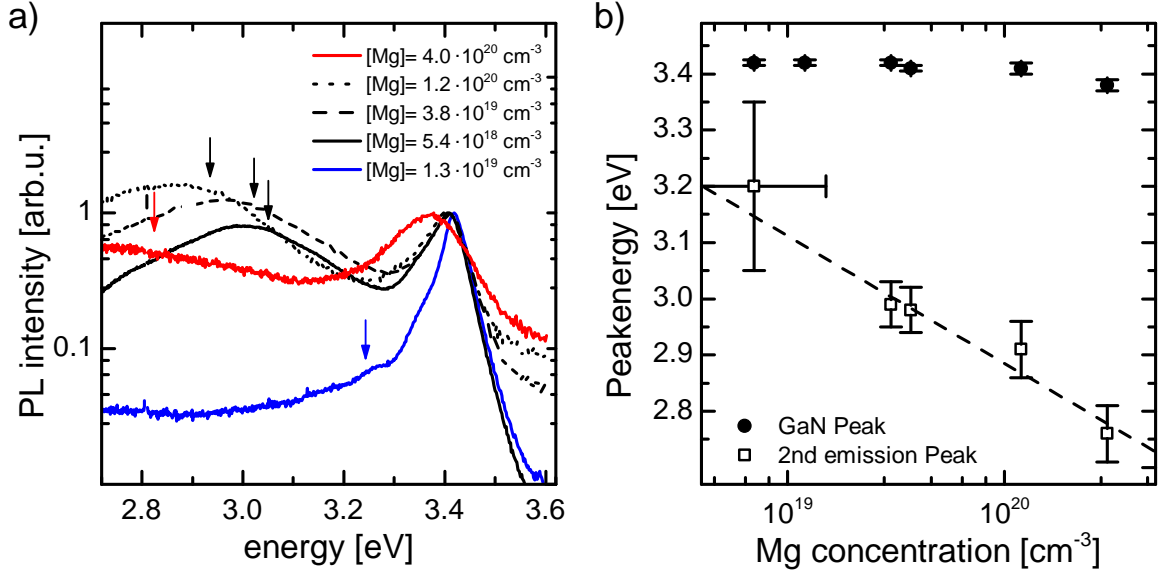
Figure 5.16.: a) PL spectra recorded at ambient atmosphere and RT for NW ensembles with different [Mg] normalized to the GaN emission. The arrows indicate the energetic position of a second detectable luminescence peak. b) Emission energy positions of the two measurable peaks for Mg–doped GaN NWs as a function of Mg–concentrations according to [96].

emission remains at a constant position, the second peak shifts to higher energies with increasing excitation intensity.

According to the power– and concentration–dependent energetic position of the emission peak, this second emission can be attributed to a DAP recombination related to the Mg–doping at RT similarly to GaN layers [36, 38, 109].

Eq. 5.15 describes the energy of the photons emitted by the DAP recombination, in dependence of the donor and acceptor energies.

$$E_{DAP} = E_g - E_A - E_D + \frac{e^2}{4 \cdot \pi \cdot \varepsilon_0 \cdot \varepsilon_r \cdot R_{DA}} \tag{5.15}$$

The energy of the emitted photon E_{DAP} is increased by the amount of $\frac{e^2}{4\cdot\pi\cdot\varepsilon_0\cdot\varepsilon_r\cdot R_{DA}}$ which represents the coulomb coupling between electron and hole. Using the assumption that $E_A = 260\,\text{mV}$ [41] and $E_D = 42\,\text{mV}$ [110] (for an O_N donor) the emission maxima in Figure 5.16b are fitted and displayed by the broken line. The high ionization energy E_A of the Mg_{Ga} acceptor explains the stability of the DAP luminescence even at RT. It is obvious that for a increasing [Mg] the value of R_{DA} decreases leading to an increased coulomb interaction term.

In the sections 4.2.3 and 5.3 the diameter was identified as a crucial parameter for the electrochemical and photoelectrochemical properties of n.i.d. and Si–doped GaN
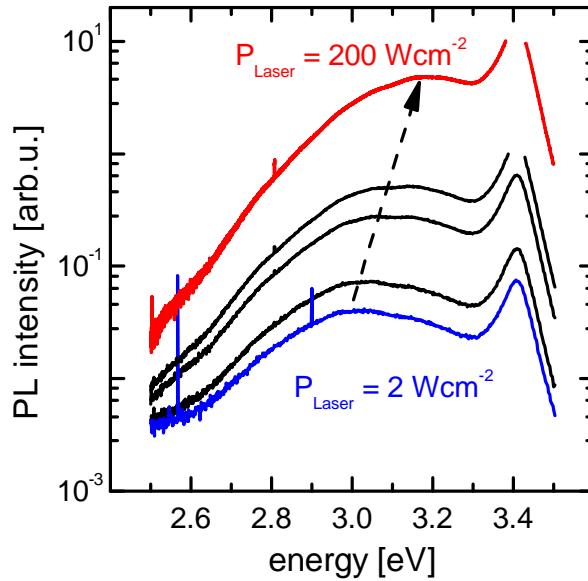
Figure 5.17.: PL spectra of the NW ensemble with $[\text{Mg}] = 5.4 \cdot 10^{18}$ cm^{-3} recorded at different excitation power densities.

NWs. In the case of Mg–doping the influence of the NW diameter is also reflected in the PL characteristics as depicted in Figure 5.18 for the NW ensemble with [Mg] = $1.2 \cdot 10^{20}$ cm^{-3}. It is shown that the relative intensities of the *near band edge emission* (NBE) of GaN and the DAP luminescence sharply depend on the NW diameter. This relation of the integrated PL emission intensities is shown as a function of the average NW diameter in Figure 5.18.

It is obvious that for NWs with a diameter > 75 nm the DAP luminescence exceeds the NBE luminescence, resulting in a ratio of NBE/DAP $\leq$ 1 (cf. spectrum upper right corner in Figure 5.18). NWs with a diameter below 75 nm are characterized by a strong NBE luminescence and a weak DAP (cf. spectrum lower left corner in Figure 5.18).

Considering the temperature–dependent incorporation of Mg into the GaN NWs during the growth process [14] differences in the Mg–content among the NWs will also occur. Furthermore, Furtmayr et al. [14] reported that increasing Mg incorporation leads to an increasing average NW diameter. Consequently, it can be assumed that thicker NWs posses a higher Mg–concentration than thinner NWs.

This interpretation is further confirmed by the evaluation of the energetic position of the DAP as a function of the NW–diameter as shown in Figure 5.19 which indicates a lower DAP emission energy for larger diameters corresponding to a higher overall Mg incorporation [14].
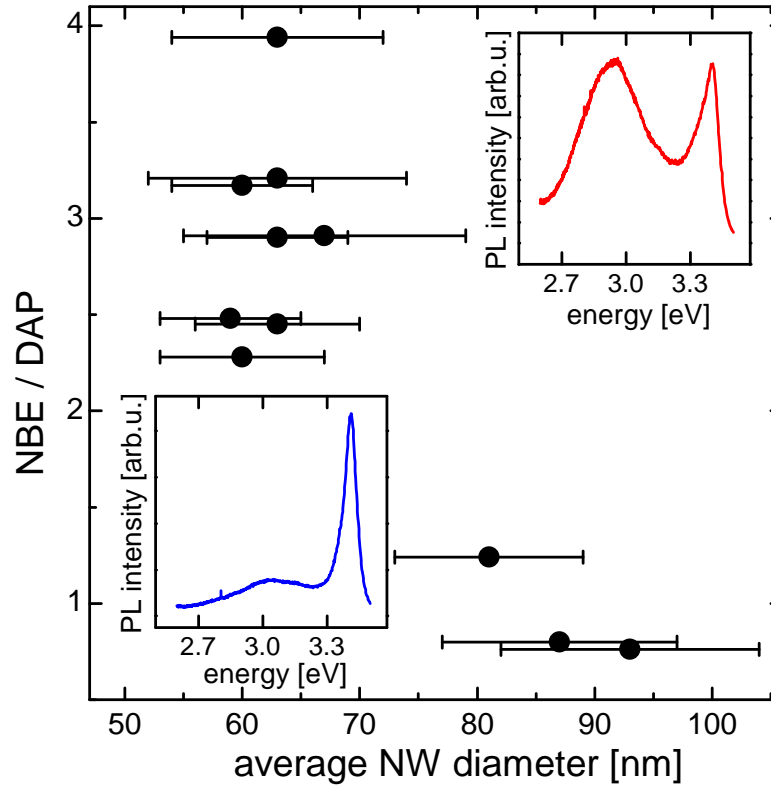
Figure 5.18.: The relation between the PL intensity of the NBE emission of GaN and the DAP as a function of the NW diameter. The inserts show one PL spectrum of a DAP–dominated NW ensemble (upper right corner) which can be detected for thicker NWs and a GaN NBE dominated PL spectrum (lower left corner) characteristic for thinner NWs.

An additional effect of Mg–doping on the PL properties is the loss of intensity due to the formation of structural defects [14, 96]. The insert in Figure 5.19 shows the PL spectra for differently Mg–doped NW samples with applied cathodic bias U_C = 1200 mV in PBS at pH 7. It is obvious that the intensity decreases with increasing Mg–concentration. While the NWs with the lowest Mg–content show a GaN emission intensity comparable to that of a n.i.d. NW sample, the PL intensity of the sample with the highest Mg–content is reduced by a factor of > 100.

pH– & bias–dependence

Following the same procedure as for the n.i.d. and Si–doped GaN NW samples, the PL of Mg–doped NWs is examined as a function of pH and bias. The floating potential with illumination ($U_{OCP} \approx 460$ mV) is measured and used as reference for the cathodic bias application. Figure 5.20a shows the PL spectra of a Mg–doped
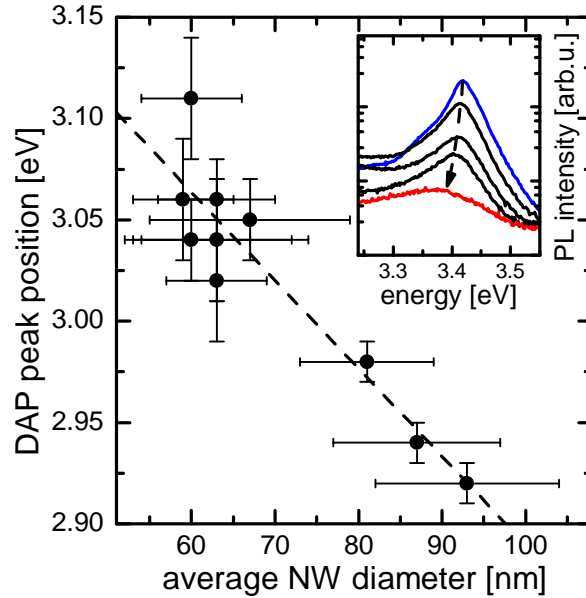
Figure 5.19.: The energetic position of the DAP luminescence as a function of the extracted average NW diameter. The insert shows the NBE emission peak magnified for 5 PL spectra of differently Mg–doped GaN NW ensembles in PBS at pH 7 and $U_C = 1200\,mV$. The arrow points towards higher Mg–concentrations. Note that the spectrum with the lowest intensity is recorded at 10 fold higher excitation intensity.

GaN NW sample with $[Mg] = 3.8 \cdot 10^{19}\,cm^{-3}$ at $U_C = 900\,mV$ between pH 7 and pH 1. Both, the NBE GaN peak and the DAP peak respond to a decreasing pH with an increasing PL intensity while the FWHM and the emission energy remain constant. In Figure 5.20b PL spectra for various applied U_C in PBS at pH 7 are shown. For clarity, only the spectra between $U_C = 850\,mV$ and $U_C = 1200\,mV$ ar depicted. Again, both luminescence peaks react to increasing U_C with increasing PL intensity. This behavior is the same as observed for the n.i.d. NWs examined so far.

Similar to the evaluation of n.i.d. and Si–doped NWs, calibration curves from the bias–dependent PL spectra for both emission peaks can be extracted. This is depicted in Figure 5.21 for the pH values between pH 7 and pH 1 in the voltage range between $U_C = 400\,mV$ and $1200\,mV$. The NBE GaN intensity was integrated between 3.35 and 3.45 eV and the DAP was integrated between 3.0 and 3.2 eV. To be able to compare the PL responses, the calibration curves are normalized to the integrated PL intensity at $U_C = 400\,mV$ in pH 7. The calibration curves in Figure 5.21 show the typical behavior explainable by the enhanced dead layer model for both luminescence peaks. In the case of the GaN NW ensemble with $[Mg] = 4.6 \cdot 10^{19}$ cm^{-3} [96] grown on p–type substrate examined here the achievable intensity gain
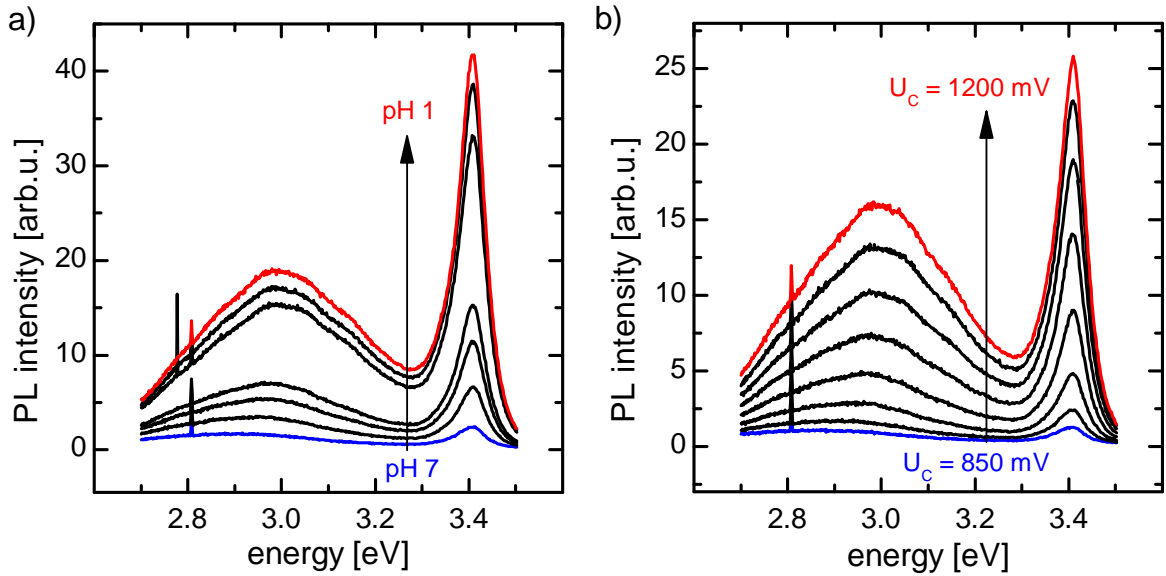
Figure 5.20.: PL spectra of a Mg–doped GaN NW sample ($[Mg] = 3.8 \cdot 10^{19}$ cm^{-3}) for a) pH 7 to 1 at $U_C = 900$ mV and b) for bias values between $U_C = 850$ mV and $U_C = 1200$ mV in steps of 50 mV at pH 7.

for the DAP related luminescence peak is significantly higher compared to the NBE of GaN for all pH values < pH 7. If this effect can be exclusively related to the Mg–doping or the average NW diameter cannot be fully classified based on the presented data.

PL measurements in basic solution reveal a good stability of the NW ensemble as shown by the calibration curves recorded in PBS with basic pH values between pH 7 and pH 12 presented in Figure 5.22.

These preliminary results indicate the large impact of Mg–doping on the PL properties of GaN NWs. The data recorded in the scope of this work indicate a strong relation between Mg–concentration in the NW and the sensitivity of the DAP emission to bias and pH changes and further strengthens the importance of the single NW diameter.

One method to examine the PL of Mg–doped GaN NWs further could be the clear identification of the measured region for a subsequent SEM analysis of the exact NW diameters.

Figure 5.21.: Calibration curves for the Mg–doped GaN NW ensemble ([Mg] = 4.6 · 10^{19} cm^{-3}) for the GaN near band edge and the DAP emission for the pH range between pH 7 and pH 1. All integrated intensities are normalized to the PL intensity recorded at $U_C = 400\,$mV pH 7.
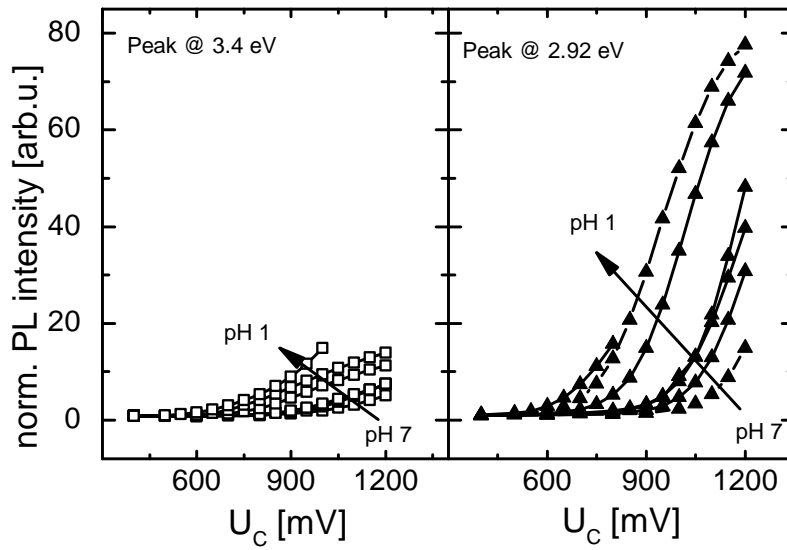

Figure 5.22.: Calibration curves for the Mg–doped GaN NW sample ([Mg] = 4.6 · 10^{19} cm^{-3}) for the GaN near band edge and the DAP emission for the pH range between pH 7 and pH 12. All integrated intensities are normalized to the PL intensity recorded at $U_C = 400\,$mV pH 7.
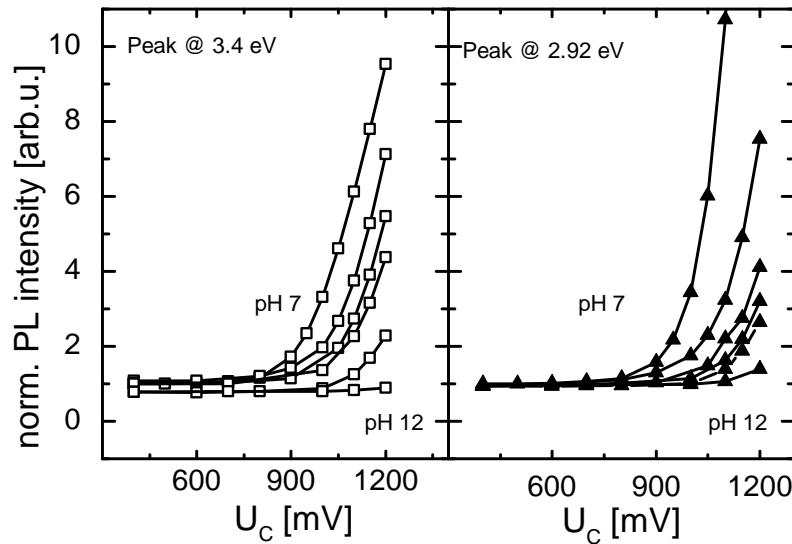
Application of Gallium Nitride Nanowires as Optical pH–Sensors

The pH–measurement in electrolytes is an important task in chemical industry, food production and water–monitoring but also for biochemical applications, e.g. monitoring enzymatic activity or cell metabolism [111, 112, 113, 114]. The emerging field of nanoparticles relies inseparable on solution–based methods for the chemical synthesis which depend on the exact knowledge of the pH [115]. Of special interest are the fields of artificial photosynthesis and photoelectrochemical water–splitting [116] which are regarded as green technologies. All these technologies require a reliable and cheap method to control the pH of a solution. A more detailed overview on different existing methods for the determination of the pH value in electrolytes is given in the appendix D.

6.1. Detection Principle

According to the presented results on the pH dependence of the PL intensity of GaN NWs, the application as optical pH sensor is discussed in this section and the first proof of principle for biologically induced pH detection experiments are presented.

According to the extended "dead layer" model discussed in section 5.3, the calibration curves are unique for each pH value. The derivative of a calibration curve in the following is, referred to as *optical transconductance* which defines the point with the highest slope and consequently the highest sensitivity towards changes of the potential. The optical transconductance is depicted in Figure 6.1a for the simulated calibration curves according to Eq. 5.14 for pH 1, 3 and 5. The maximum of the optical transconductance depends on the pH. This concept is applied to the measurement data presented in Figure 6.1b for a n.i.d. GaN NW sample. The corresponding optical transconductances are depicted for the pH values of 5, 3 and 1. This fact allows a pH detection that can compensate fluctuations in the overall PL intensity which is favorable in long term use.

In the following, several issues that are relevant for the application as a pH sensor are discussed on the basis of specific experiments.
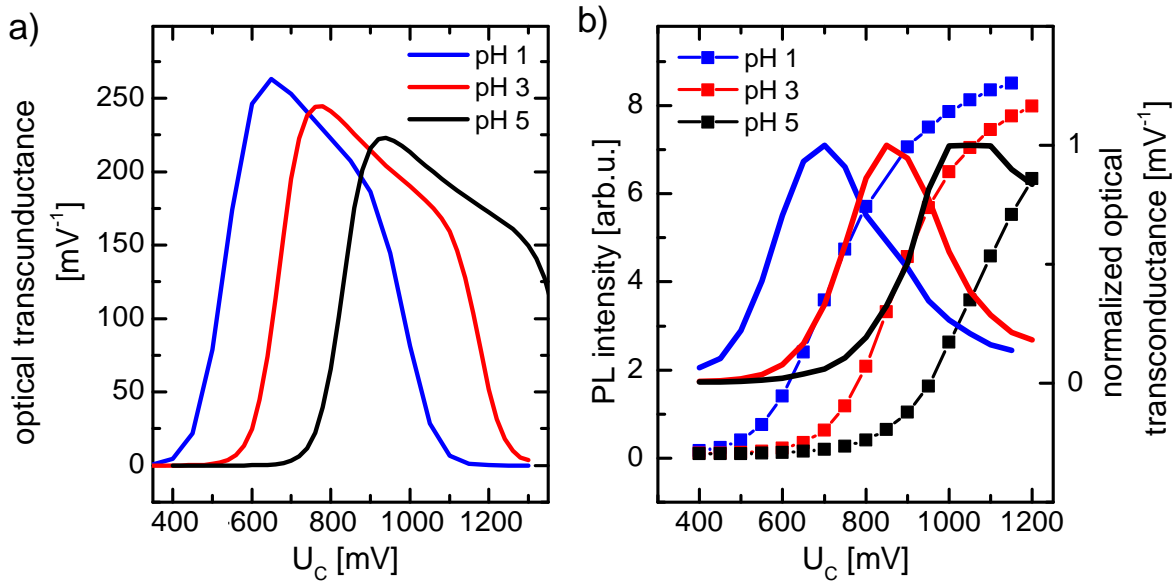
Figure 6.1.: Calibration curves for a n.i.d. GaN NW sample at pH values of 5, 3, 1 with the normalized derivatives representing an optical transconductance.

6.1.1. Reproducibility

For a possible application as a pH sensor the reproducibility of the sensor is a crucial parameter. Figure 6.2a shows 12 PL spectra recorded for different pH values between 7.4 and 6.6. Each pH was preadjusted in a particular reservoir. In the insert of the Figure the two PL spectra recorded at pH 7.1 are magnified to allow a discrimination. During the experiment the reservoirs were exchanged carefully to guarantee that no air is injected into the measurement setup and that the applied cathodic bias potential is maintained during the solution exchange. All spectra were recorded in PBS at U_C = 1000 mV. The measurement spot was illuminated under applied bias conditions for 25 minutes previous to the actual measurements to guarantee the complete stabilization of the PL intensity (cf. section 5.1).

In Figure 6.2b, the integrated PL intensities (between 3.35 and 3.45 eV) from Figure 6.2a are arranged in the order of their recording.

The recorded spectra and the integrated intensities in Figure 6.2 indicate the high accuracy and reproducibility of the pH–dependent PL intensity measurement for GaN NWs in three electrode configuration.

6.1.2. Response Time

Another possible detection method is the transient PL measurement while the pH is exchanged. Figure 6.3a shows the integrated PL intensity during a pH exchange
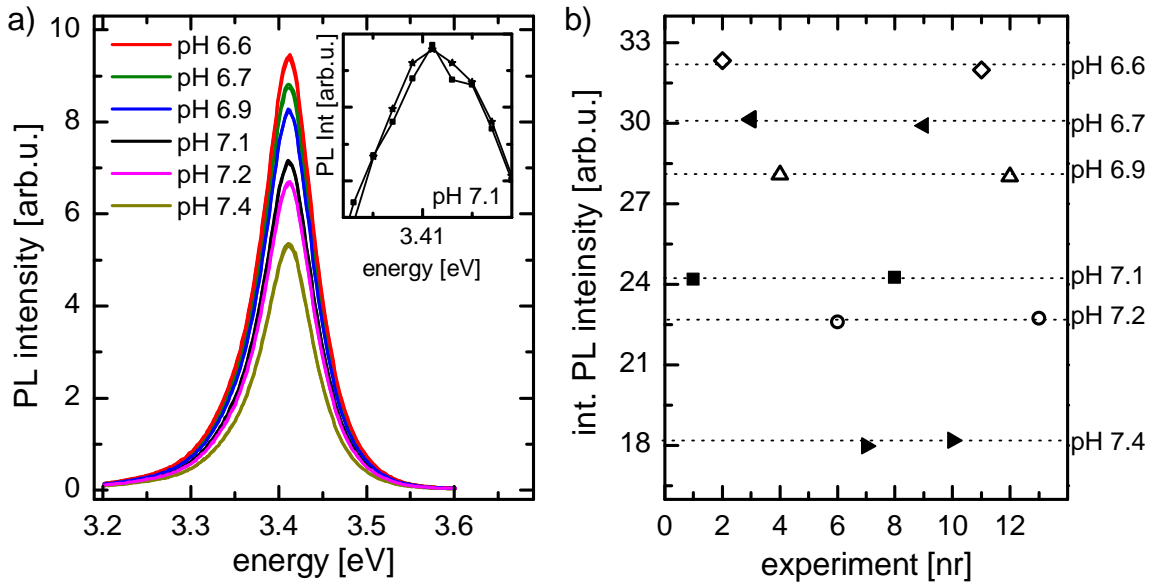
Figure 6.2.: a) 12 PL spectra recorded for GaN NWs in the pH interval between 7.4 and 6.6. The insert shows the two magnified spectra recorded at pH 7.1. b) Corresponding integrated PL intensities in the order of recording.

for a n.i.d. GaN NW sample. Obviously the PL resembles all pH steps with a slight delay that can be attributed to the tube length between reservoir and measuring cell.

Figure 6.3b shows in a magnified diagram a part of Figure 6.3a of the pH steps between pH 6.82 and pH 6.94 and between pH 6.94 and pH 7.05. The broken lines indicate the times of executed pH changes. It is clearly visible that the PL transient requires three to four measurements to reach the stable plateau (indicated by the dotted lines). With the duration of one PL recording of $\approx 10\,\text{s}$ this results in a response time of the system of $30 - 40\,\text{s}$ to pH changes. This response time is specific for this system and is assumed to be lowerable by the optimization of electrolyte inlet and measuring time.

6.1.3. Sensitivity

Due to the restrictions of the glass electrode pH sensor with a resolution of 0.01 pH and the lack of temperature control a pH resolution > 0.05 cannot be realized. An alternative to test the maximum sensitivity are bias–dependent transients. To simulate the maximum achievable resolution, two bias–dependent PL transients were recorded at pH 7. Both transients, depicted in Figure 6.3b, were recorded using identical experimental conditions but vary in their electrolyte concentration (10 and 1 mM PBS), which implies different conductivities of the electrolyte.
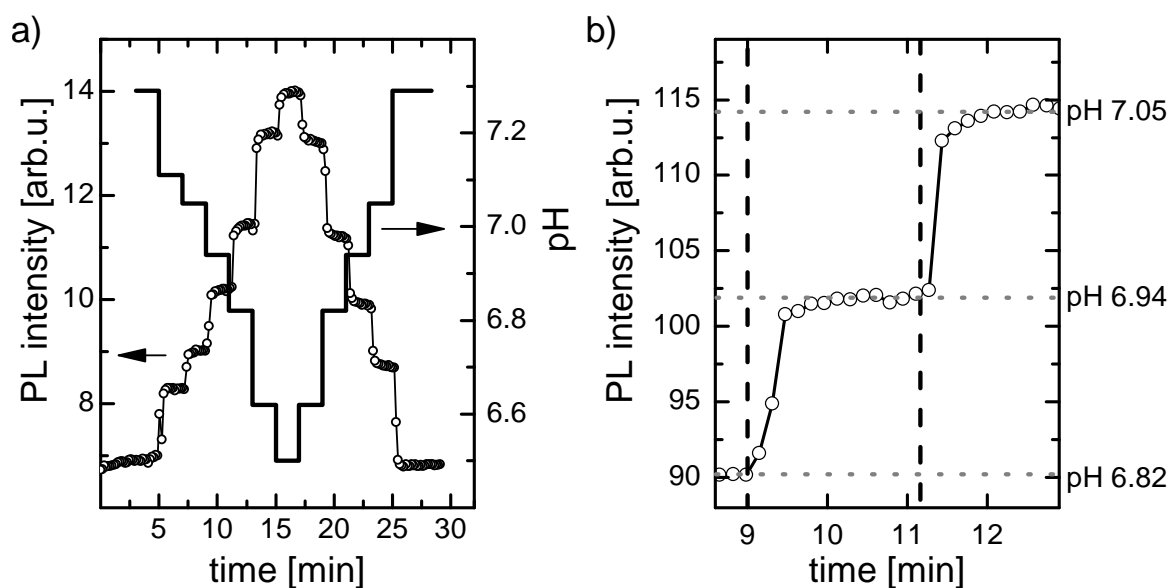
Figure 6.3.: a) Transient measurement of the PL intensity for a n.i.d. GaN NW sample at $U_C = 1000\,\text{mV}$ for variation of the solution pH between 7.3 and 6.5. b) Magnification of the pH steps between pH 6.82 to pH 6.94 and pH 6.94 to pH 7.05 indicating the delayed PL reaction.

The response of the PL intensity upon variation of U_C in steps of $1\,\text{mV}$ from 1000 to $990\,\text{mV}$ was detected for both concentrations.

These results show that variations as small as $1\,\text{mV}$ can be resolved in the PL response even for diluted concentrations ($1\,\text{mM}$ PBS). Under consideration of the pH–induced shift of $\text{Int}(U_C)$ between 40 and $90\,\text{mV/pH}$ (cf. Figure 5.7a), which is in good agreement with the reported pH dependence of the surface potential of c–plane GaN layers [98, 99], a bias–variation of $1\,\text{mV}$ corresponds to differences in pH of 0.01 to 0.03.

6.1.4. Detection of an Enzymatically produced pH Change

As a proof of principle for the detection of a biologically induced pH change, the enzymatic conversion of penicillin–G into penicilloic acid by penicillinase is examined on basis of the PL intensity change of GaN NWs. The deprotonation of the enzymatically produced penicilloic acid is the pH relevant process. Details about the used enzyme and the occurring reaction can be found in [117, 118, 119].

The measurement setup described in section 3.4.1 was modified in order to reduce the measurement volume of the measuring solution to a minimum of $10\,\text{ml}$. To guarantee a homogeneous distribution of enzyme and substrate the experiments were
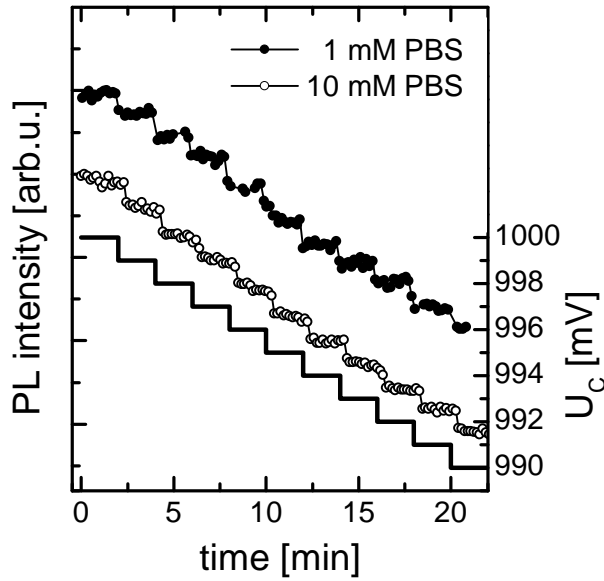
Figure 6.4.: PL transients for U_C in steps of $1\,\mathrm{mV}$ for $\approx 2\,\mathrm{minutes}$ from 1000 to $990\,\mathrm{mV}$ for two electrolyte molarities. For clarity the transient for $1\,\mathrm{mM}$ is shifted.

performed while the electrolyte was exchanged at maximum rate of $30\,\mathrm{ml/min}$. The measurements were carried out at room temperature.

To detect the enzymatically catalyzed production of penicilloic acid, the PL of a n.i.d. GaN NW sample in $1\,\mathrm{mM}$ PBS at the working point at $U_C = 1000\,\mathrm{mV}$ (cf. section 5.1) at pH 7 [120] is monitored.

Figure 6.5 shows two transient PL measurements. The penicillinase concentrations were adjusted to $0.49\,\mu\mathrm{M}$ (represented by the open circles) and $0.25\,\mu\mathrm{M}$ (represented by the open triangles) and fully dissolved in the circulating PBS before the measurements started. In 10 intervals of $\approx 2.5\,\mathrm{minutes}$ length, $6\,\mathrm{mmol}$ of penicillin–G solution were added. The stepwise shape of the transients indicates that it is possible to detect the enzymatic activity of penicillinase by the transient changes in the GaN NW PL for both enzyme concentrations. Both PL transients reproduce the stepwise structure of the substrate addition curve. The curve for $0.25\,\mu\mathrm{M}$ penicillinase is shifted to higher PL intensities for clarity.

A more detailed examination of the curve for $0.49\,\mu\mathrm{M}$ penicillinase reveals that per addition interval of penicillin–G the PL intensity rises by $\approx 7\%$. According to the transient pH measurements this corresponds to a pH change of 0.06 pH per interval.

Assuming that no UV–induced degradation of the penicillinase occurs, the smaller amount of penicillinase should catalyze the same amount of added substrate in a extended period of time. On the same timescale the lower concentration of peni-
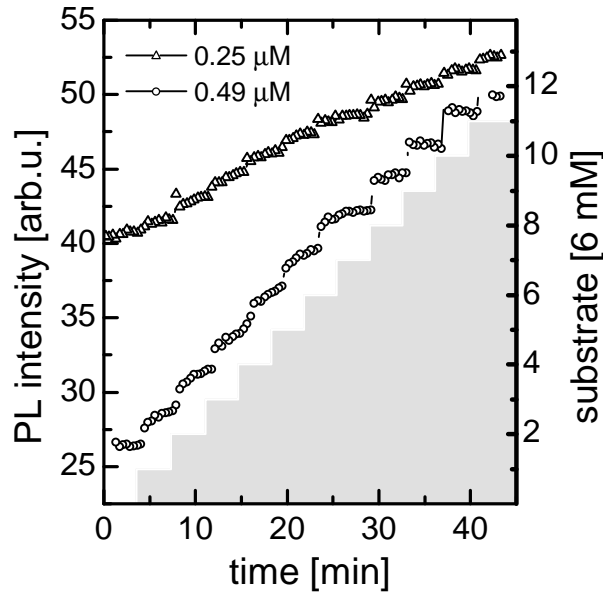
Figure 6.5.: Transient PL intensity measurements of penicillinase activity upon 10 additions of 0.6 mM penicillin–G for two different concentrations penicillinase. The staircase function indicates the penicillin–G addition.

cillinase catalyzes less penicillin–G and consequently leads to a less detectable pH change.

6.2. Indium Gallium Nitride NWs

For biological-related application in optical pH–detection, the above band gap illumination with $E_{exc} > 3.41$ eV (363.63 nm) necessary for GaN NWs is problematic due to the destructive influence of UV light (< 320 nm) on the *Deoxyribonucleic acid* (DNA). A possible alternative are the ternary alloys consisting of Gallium, Indium and Nitrogen. The energy gaps for these group III–nitride materials can be adjusted to the visible regime. By lowering the bandgap of the material, lower excitation energies are sufficient to excite the PL. Figure 6.6a depicts the bandgap of the alloy composition $In_{1-x}Ga_xN$ for an Indium content between 0 and 100 % [121]. The theoretical shape is plotted according to reference [122]:

$$E_g(In_{1-x}Ga_xN) = xE_g^{GaN} + (1 - x)E_g^{InN} - bx(1 - x) \qquad (6.1)$$

Eq. 6.1 represents the so–called virtual crystal approximation with the bowing parameter b = 1.1 according to [27, 122].

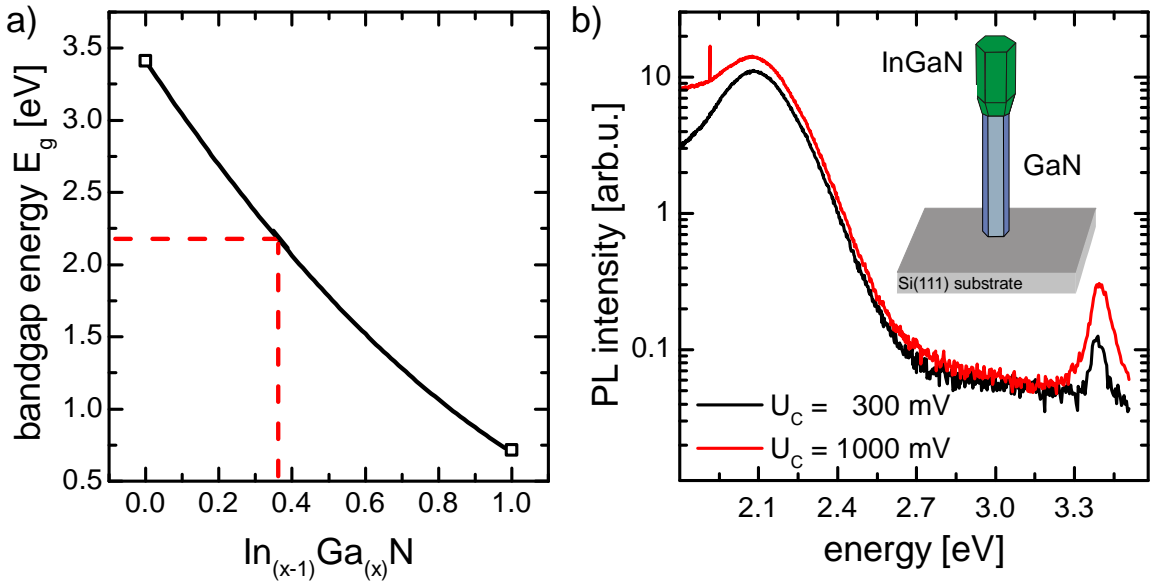Therefore, a possible alternative to the GaN NWs examined so far InGaN/GaN

Figure 6.6.: a) Evolution of the bandgap of $In_{1-x}Ga_xN$ for increasing Indium concentration. Calculated with b = 1.1 [122] according to Eq. 6.1. b) Two PL spectra of one InGaN NW sample excited with an UV laser at 325 nm in 10,mM PBS at pH 7 for the cathodic bias values of U_C = 300 mV and U_C = 1000 mV. The insert schematically shows the structure of GaN/InGaN NWs.

NW structures will be examined in the following. The schematic structure of the NWs is depicted in the inset in Figure 6.6b. On top of an initially grown GaN base part the InGaN part was grown at a lower substrate temperature of 560°C, leading to an increase of the NW tip diameters up to about 90 nm. From the position of the PL emission energy peak at T = 4 K the In concentration is estimated to 36 % using Eq. 6.1 with a conduction band offset to GaN of 1.20 eV [27]. The growth conditions of the InGaN NWs used here are similar to those described for the growth of InGaN nanodisks in GaN NWs presented in [121]. Recently, Tourbot et al. [123, 124] demonstrated that in InGaN/GaN NW the formation of In rich areas occurs. This would lead to a broadening of the overall PL spectra as it can be observed in Figure 6.6b.

In Figure 6.6b the PL excited with the UV–laser (HeCd laser (30 mW), λ = 325 nm) is depicted at pH 7 for two different bias values U_C = 300 mV and U_C = 1000 mV. It is clearly visible that the PL emissions of both parts of the NW, namely the GaN Base and the InGaN top, increase to cathodic bias application. The absolute PL intensities of the GaN and InGaN emission cannot be compared as the spectra are not corrected for the response of the optical system which, however, is not necessary as here the

interest is focused on the relative variations of the intensity.

In the following, a green laser (λ = 532 nm) is used for PL–excitation.

Figure 6.7a shows the PL spectra for the pH values between 7 and 1 and a cathodic bias of U_C = 200 mV. The PL emission of the InGaN part shows in principle the same the same evolution for bias application and pH changes as the GaN NWs. However, in this case the PL spectra at U_C = 200 mV for pH 2 and pH 1 are almost identical. Figure 6.7b shows the integrated PL intensities for different pH values. In contrast to the pure GaN NWs these calibration curves are not normalized to the PL value corresponding to a $U_C \approx U_{OCP}$ but to the U_C producing the maximum achievable PL intensity for each pH value.

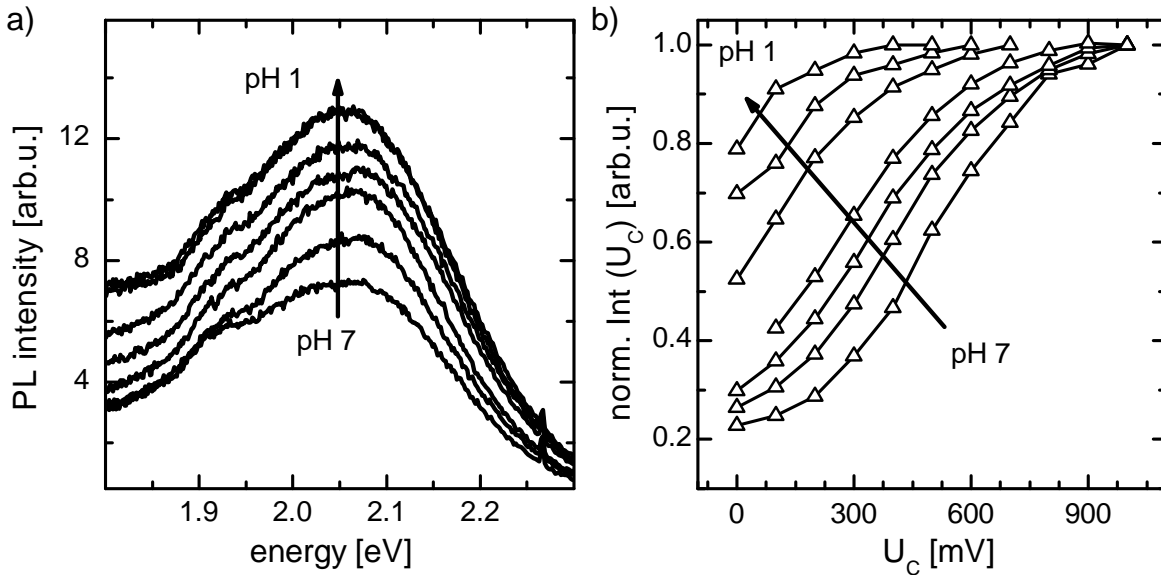
Figure 6.7.: a)PL spectra of GaN/InGaN NWs recorded at various pH values at U_C = 200 mV. b) The normalized integrated PL intensity (between 1.95 and 2.15 eV) as a function of bias and for different pH values. The data are normalized to the maximum achievable PL intensity for each pH value.

The intensity modification by external bias and pH are far smaller than for GaN NWs. While for GaN NWs an intensity enhancement of up to a factor of 200 is observed for the InGaN NWs the factor was 3 at max. According to the model presented for the GaN NW in section 5.3 this reduced enhancement factor indicates a smaller SBB in the InGan/GaN NWs and as a result a lower non radiative recombination rate. The fact that the saturation of the PL intensity is achieved at lower values $U_C \approx 900$ mV (pH 7) and $U_C \approx 400$ mV (pH 1) also points towards the direction of less pronounced loss processes. Consequently, less potential is required to overcome the loss processes by establishing a inversion layer at the surface of the

InGaN.

6.2.1. Detection of an Enzymatically produced pH Change

The experiment to detect the enzymatically produced penicilloic acid with GaN NWs and UV–illumination presented in section 6.1.4 is repeated in the following with the above presented GaN/InGaN NWs excitable with a green laser. Excitation in the visible range is noncritical when it comes to more complex biological system e.g. living cells.

The working point was set according to the optical transconductance in Figure 6.7b to $U_C = 300\,\text{mV}$. Figure 6.8 shows the pH change resulting from the enzymatic reaction of penicillin–G to penicilloic acid as transient PL intensity measurements at the GaN/InGaN NW sample. The recorded PL transient shows more noise than the comparable transient with GaN NWs in Figure 6.5. Nevertheless, the substrate steps are resembled in the PL transient for the substrate concentrations $> 400\,\mu\text{M}$.
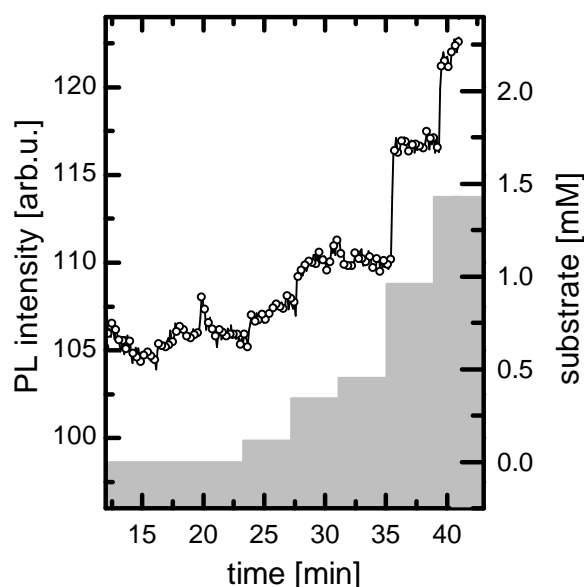

Figure 6.8.: The pH change resulting from the enzymatic reaction of penicillin–G to penicilloic acid catalyzed by penicillinase is detected optically by a PL intensity transient at a GaN/InGaN NW sample at $U_C = 300\,\text{mV}$. The staircase function indicates the penicillin–G addition.

Conclusion & Outlook

In the present work, the potential of group III–nitride nanowire (NW) ensembles for application as bio–chemical sensors with optical readout was evaluated. The sample analysis was divided into two main parts. At first, an electrochemical analysis with impedance spectroscopy (IS) and cyclic voltammetry was conducted. The second part comprises a photoelectrochemical examination by means of photoluminescence spectroscopy (PL) at room temperature.

In the electrochemical characterization by impedance spectroscopy the recorded impedance spectra were evaluated by comparison to an electrical equivalent circuit (EEC) consisting of ideal electrical elements. The influence of Silicon– and Magnesium–doping on the extracted parameters defining the NW/electrolyte interface, the surface capacitance (C_S) and the surface resistance (R_S), was investigated.

Comparing the n.i.d. GaN NW ensembles to Si–doped ensembles reveals an increase of C_S from $(2.2 \pm 0.3)\ \mu\mathrm{F\,cm^{-2}}$ to $(55.6 \pm 31.2)\ \mu\mathrm{F\,cm^{-2}}$ with a simultaneous reduction of R_S. This is assigned to the formation of a conductive channel inside the NWs. For Mg–doped NWs only a slight increase of R_S in combination with a small decrease of C_S was observed and assigned to compensation of the residual n–type doping. Open circuit voltage measurements for higher Mg–concentrations ([Mg] $> 10^{20}\ \mathrm{cm^{-3}}$) measured under illumination indicate the presence of p–type regions along the NWs.

According to the extracted electrochemical parameters (C_S, R_S) the NWs were classified into two groups. On the one hand, the conductive NWs, defined by a high C_S ($> 10^{-5}\ \mathrm{F\,cm^{-2}}$) in combination with a low R_S ($< 10^{-7}\ \Omega\,\mathrm{cm^2}$). On the other hand, the resistive NWs which were characterized by a lower C_S and higher R_S.

The differences between these two groups were explained in terms of different bandprofiles within the NWs. Assuming a constant diameter along the NW growth axis the width of the space charge region W_{SCR} depends on the doping concentration. Due to Si diffusion the doping concentration is known to be higher in the region close to the interface to the Si substrate. The interplay between the NW diameter d and the surface band bending (SBB) determines the potential barrier U_{fb} for electrons to reach the surface. For conductive NW a high doping concentration and/or a

large diameter allows the formation of a conductive channel in the NW so that the complete NW to contributes to C_S and R_S. On the contrary, a resistive NW with a thin diameter is fully depleted of charge carriers as the space charge region is extended throughout the whole NW.

This model was approved by cyclic voltammetry measurements which indicate the interfacial charge transfer into a redox couple (Fe^{2+}/Fe^{3+}) occurring only for conductive NWs.

Bias application allows for the modification of the SBB inside the NWs which was investigated by bias-dependent IS analysis. Cathodic bias application decreases W_{SCR} for resistive NWs, resulting in an increase of C_S accompanied by a significant decrease of R_S (by up to two orders of magnitude). Anodic bias application showed the opposite effect of a sharply increased R_S (by two orders of magnitude) and a slightly decreased C_S for the conductive NW sample with the highest Si–concentration, indicating that the electrical characteristics of NWs can be controlled by externally applied bias.

The photoluminescence of GaN NW ensembles in electrolyte solution was characterized as a function of the externally applied bias (U_C) and the pH value. It was shown that the intensity of the PL intensity strongly depends on the bias and the pH, while its energetic position and full width at half maximum (FWHM) remain unchanged.

These results were discussed on the basis of the extended "dead layer" model for semiconductors, assuming the absence of radiative recombination within the space charge region W_{SCR}. Photo–generated charge carriers can either recombine non–radiatively at the surface or radiatively in the field–free NW center. The application of cathodic bias at constant pH directly impacts the SBB with the result that photo–generated holes are no longer attracted towards the surface. As a consequence the radiative recombination rate increases while non–radiative losses at the surface decrease. At constant bias the decrease of the pH value below 7 leads to a similar increase of the intensity. This was explained in terms of the site–binding model which states that in acidic solutions the surface becomes more positively charged. This impacts the SBB in a similar manner as cathodic bias.

Blocking the interfacial hole transfer by the exchange of the water–based electrolyte with an ionic liquid resulted in an overall higher PL intensity indicating the importance of this loss mechanism. The "extended dead layer model" was confirmed by analysis of Si–doped NWs that exhibit a higher SBB due to the smaller width of the SCR. First results on the influence of Mg–doping of GaN NWs were

presented.

The GaN peak of Mg-doped NW ensembles showed a response towards cathodic bias and pH identical to that of n.i.d. GaN NWs. A second luminescence peak attributed to a DAP recombination reacts in a similar manner towards bias and pH changes as the near band edge emission. The PL intensity ratio of both peaks strongly depends on the diameter of the examined NWs. Thicker NW contain a larger amount of Mg which results in a dominating DAP luminescence while thinner NW are dominated by the GaN emission.

Finally, a conceptional study of NW ensembles as an optical transducer for pH detection was briefly presented. According to the "extended dead layer model" the optical transcoductance could be defined. With this definition of a working point of the sensor was examined with the purpose of testing the sensor with respect to its reproducibility, response time, and sensitivity. The data indicated that with the setup used here a pH resolution of 0.05 pH can be achieved with high reproducibility.

Finally, two proof of principle measurements were presented where the enzymatically catalyzed production of penicilloic acid accompanied by a subsequent pH change was optically detected with GaN and InGaN/GaN NWs.

Outlook

The measurement showed the strong influence of the diameter on the (opto) electrochemical properties of NWs. Therefore, the exact knowledge, in the ideal case the control, of the NW diameter and the NW length at the measurement position is of major importance for further measurements. In the case of Mg–doped NWs this could enable a better understanding, especially about how the Mg–incorporation in the NWs is accomplished and this influences the sensitivity of the DAP luminescence which is not interfered by the intrinsic water luminescence.

In comparison to Si–doping, Ge–doping of GaN NW promises a smaller impact on the structural properties and strongly suppresses the lateral growth of highly doped NW. With a possible gradual Ge–doping along the NW growth axis it might be possible to adapt a desired evolution of the SBB along the growth axis without the disadvantage of an increasing diameter.

Following another approach, the use of heterostructures, like quantum disks of GaN embedded in AlGaN NWs or InGaN in GaN Nws, could be a way to increase the sensitivity and stability and to overcome the interference of the GaN emission with the intrinsic water luminescence. The approach with a quantum disk structure

might also offer a way to increase the SBB in InGaN NWs with the aim to achieve higher intensity changes. A better conductivity of the GaN base region could further be achieved by doping.

In a first proof of principle experiment the spatially resolved detection of the PL with a standard microscope setup was demonstrated using InGaN/GaN NWs. Figure 7.1 depicts a series of microscope images recorded for an InGaN/GaN NW sample at different applied U_C in 10 mM PBS. The PL was excited with a mercury arc lamp using an excitation filter (530 – 580 nm) and the detection of PL–light $\lambda_{PL} \geq$ 615 nm was detected using a CCD camera. It can be seen, that the intensity of the PL emission first decreases under the reduction of U_C till the sample is completely dark (between $U_C = 400$ mV and $U_C = 0$ mV). In the following increase of the cathodic bias the PL intensity is increased again. It is also obvious that the images shows areas that shine brighter and react at other values of U_C with an intensity change. This can be attributed to inhomogenities across the NW ensemble indicating towards different In–concentrations or NW diameters.

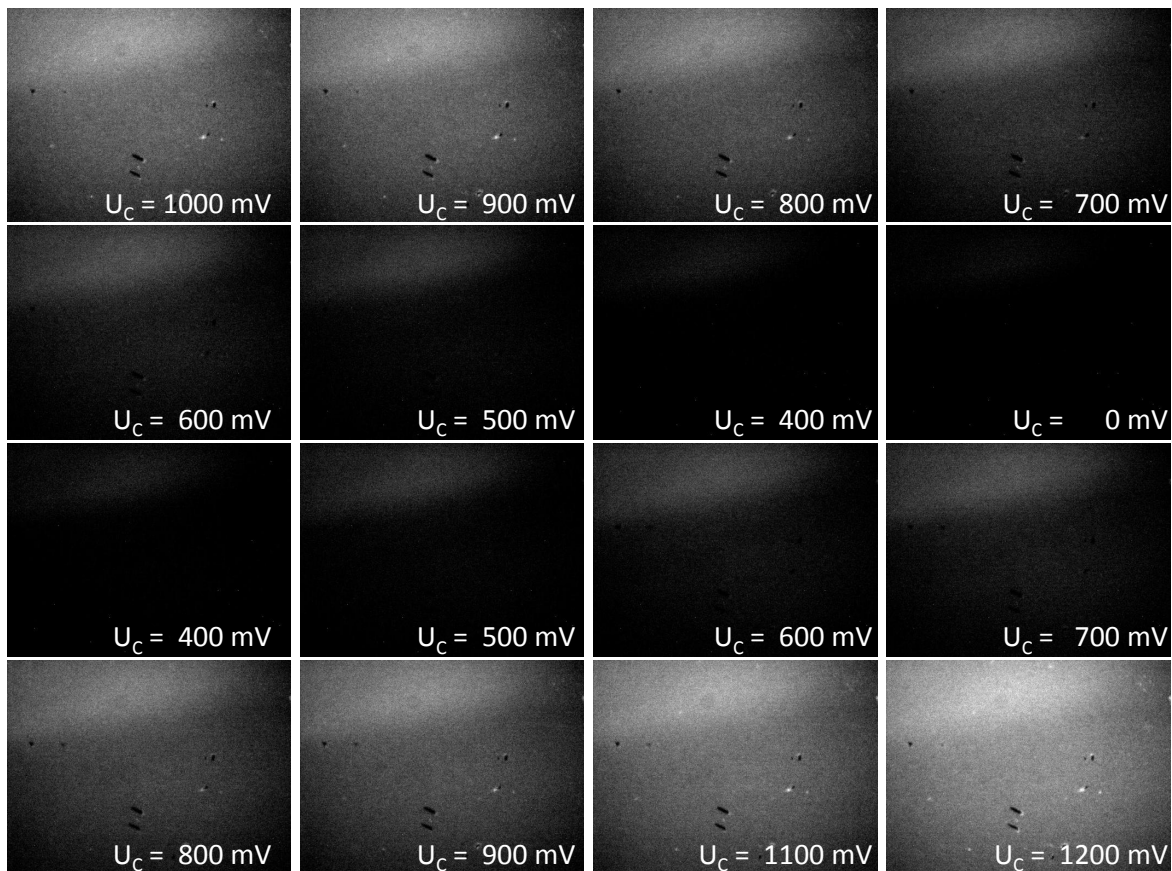Figure 7.1.: Subsequent microscopic images taken of a InGaN/GaN NW sample at different applied U_C. The area depicted is ≈ 0.5 mm^2.

With optimized InGaN/GaN NWs the detection of local pH–changes produced e.g. by cells is possible. With a time–resolved recording this could offer a completely new approach for in–vitro monitoring of any kind of biological process that involves a pH change.

Sample Inhomogeneities

As a consequence of the self–assembled growth process the resulting NW ensemble yields a certain inhomogenity of the NW height, diameter and density. One main reason for this fluctuations is the non uniform heat–distribution across the substrate surface which has a larger impact with increasing sample size. These fluctuations also influence the incorporation of dopands and the growth rates of the NWs.
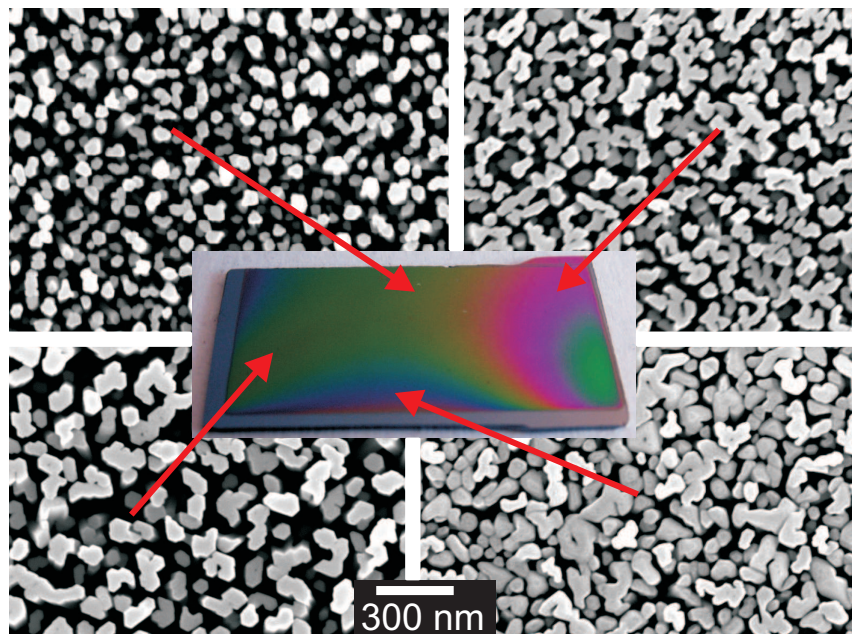

Figure A.1.: Four scanning electron microscope images of a Mg–doped GaN NW sample ($[Mg] = 1.2 \cdot 10^{20}$ cm^{-3}) taken at different positions (as indicated) of the sample.

Due to the relatively large sample area defined for the electrochemical measurements ($\approx 50\,\text{mm}^2$) the effects of the wire–to–wire fluctuations can be negelcted. The situation changes significantly for the photoelectrochemical experiments where the illuminated spot on the NW sample is $< 0.01\,\text{mm}^2$. In this case the local wire–to–wire variations have a great impact on the experimental results.

Figure A.1 illustrates this issue for a Mg–doped NW sample ($[Mg] = 1.2 \cdot 10^{20}$ cm^{-3} [96]). Different SEM images recorded at the indicated positions visualize these strong fluctuations. A clear assignment of a specific area with average NW geometry

to the reflections of one color is not possible.

In summary it can be stated, that for the Mg–doped GaN NWs the average thickness of the examined NWs is of major importance for the expectable DAP luminescence.

Electrostatic Charging of GaN NWs

The structural evaluation of the NW ensembles is typically performed in a scanning electron microscope (SEM). Depending on the actual diameter and height of the NW a charging effect leading to an agglomeration of the NWs is observable. Single NWs are charged up by the incident electron beam ($U_{ac} = 30\,keV$) in dependence of their conductivity. Thicker NWs due to the presence of an conductive channel in their centrer avoid being strongly electrostatic charged. Figure B.1 shows a series of three SEM images taken from a live examination of a n.i.d. GaN NW ensemble. The first image was recorded directly at the beginning of the examination at $t = 0\,s$. The second image was taken after $15\,s$ and the last after $35\,s$ continuous detection. Changes in the overall NW morphology occurring in the first Intervall are indicated by the red circles in the upper and middle image. Subsequent occurring changes in the second interval are marked by orange circles in the middle and lower image. From the inspection of both intervals the electrostatic induced moving of NWs is clearly demonstrated. Smaller NW move towarda thicker NW or groups of NWs.

Whether this effect leads to a detachment of NWs from the substrate or if the NWs only bend over, can not be distinguished from these findings. Nevertheless, the process seem irreversible when the NWs have clutched together.

In summary can not be excluded, that this agglomeration of NW also occurred during the EIS measurements. However, this effect is very distant sensitive and can not be responsible for the complete stripping of NWs that is pictured in section 4.2.1 Figure C.2.
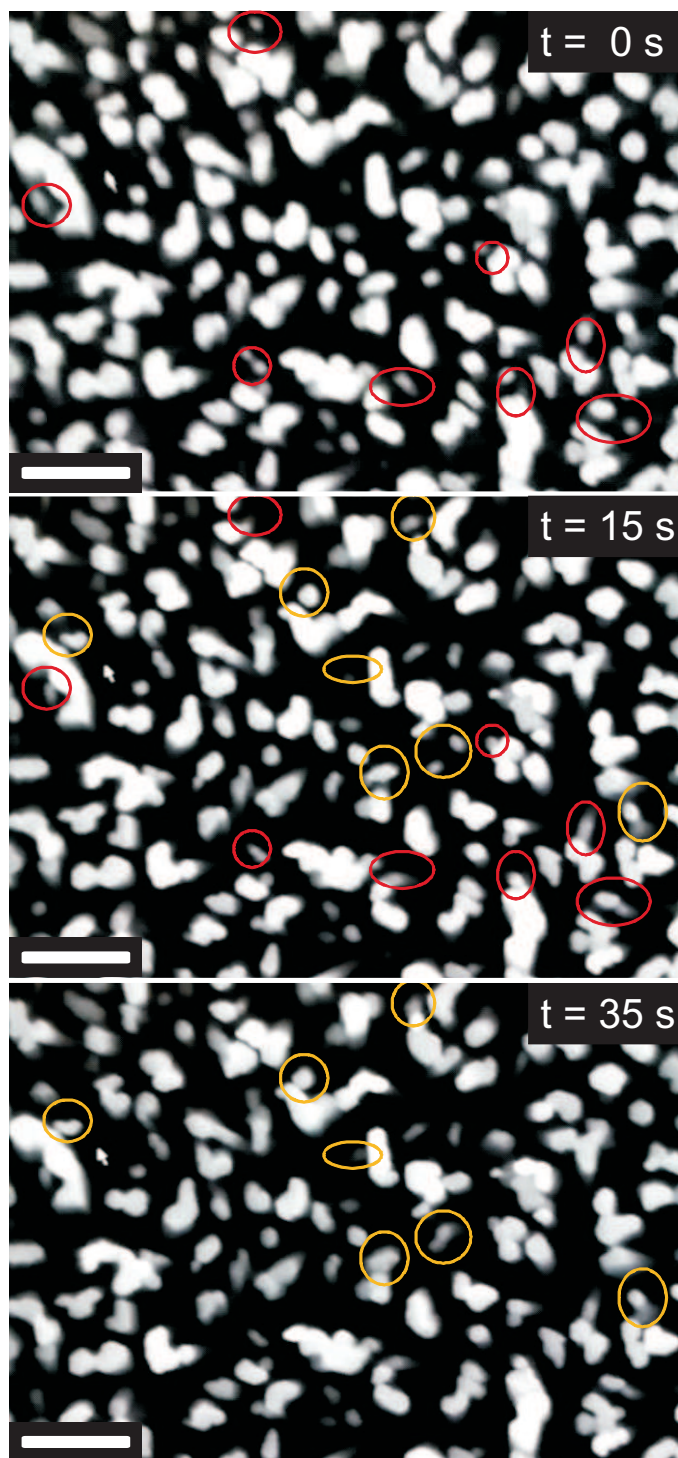
Figure B.1.: A series of three SEM images. The red circles indicate the position where morphological changes occure due to electrostatic charging after 15 s the orange circles after additional 35 s. The size of the scale bar is 100 nm.

Long Term Stability

According to the classification of GaN NWs into resistive and conductive the reproducibility of the measured IS is different. As representative of the resistive group a Si–doped GaN NW sample (T_{Si} = 980°C) was repetitive measured over a period of 14 months. Figure C.1a shows IS after different storage times (1 to 7 months). The stars in Figure C.1a represent the first recorded IS at U_C = 0 mV after the corresponding storage period (under ambient atmosphere) and the filled circles the stabilized spectrum. Complete recovery of the IS shape is observed after all three storage periods. The number of measurement cycles required to reach the stabilized spectra increases with increasing storage time.
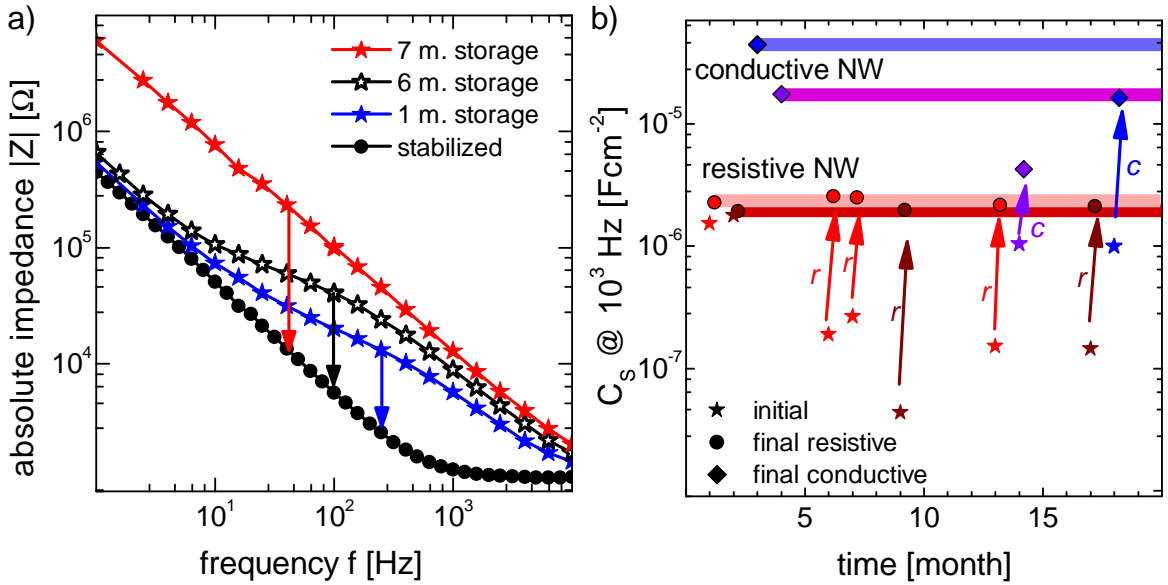
Figure C.1.: a) IS for a resistive NW recorded in various time intervals. The first and the last measurement at U_C = 0 are depicted. b) Evolution of the extracted electrical parameters for two resistive and two conductive NW samples. The stabilized values are indicated by the colored bars.

Figure C.1b shows exemplarily the extracted values for the surface capacitance for the sample depicted in Figure C.1a and a conductive NW ensemble at the fixed frequency of $\omega = 10^3$ s^{-1}. The star symbols indicate the values extracted from the first measurement of each series, while the circle (resistive NWs) and squares (con-

ductive NWs) represent the stabilized parameters. It is obvious that the surface capacitance C_S decreases by almost one order of magnitude after storage in air due to an additional contribution from the second RC–element. The extracted values for C_S at the beginning of the measurements (represented by stars) and at the end of the stabilization (full circles) indicate complete reversibility of the storage induced effects for resistive NW samples. The arrows indicating the recovery of C_S for resistive NWs are additionally marked by a r.

For the conductive NW this effect is also measurable. After a storage period the IS shape indicates the presence of adsorbates that are stripped during IS recording. In contrast to resistive NW the stabilized value for C_S does not fully resemble the initial value. Figure C.1b depicts the evolution for conductive NWs (T_{Si} = 1160°C) represented by the square symbols. It becomes obvious that irreversible changes at the surface occur, which permanently decrease the original value of C_S. The arrows indicating the recovery of C_S for conductive NWs are additionally marked by a c.

The exact microscopical interpretation of this effect is unclear. It is known that anodic oxidations of GaN layers under UV–illumination occurs preferentially at structural defects and causes the formation of amorphous Ga_2O_3 [125]. More recently Teubert et al. [24] demonstrated for InGaN quantum dot structure in a GaN matrix that anodic currents (30 μA) in a basic solution lead to the oxidation of current pathways which permanently increases the resistance. In the case of conductive NWs this effect might be enhanced due to the high Si–concentration especially in the NW region close to the Si substrate. This interpretation is in agreement with Figure C.2 that shows a conductive GaN NW sample after long term IS measurements at high potentials of both polarities (U_A, $U_C \leq 800\,mV$). The NWs in certain regions are cut off directly at the foot and either stick with neighboring NWs or are washed away. This could be related to anodic oxidation processes preferentially occurring in this region with the result of weaker stability of the NW substrate connection. This reduction of contacted NWs consequently leads to a decrease in the measured C_S. Another possible explanation of the observable sticking of the NWs in the intact regions was given in appendix B.

As the storage effect was not observed for either the substrate reference or the plain Si substrate the effect can be attributed to the NWs. IS measurements after the sample has been stored in an exsiccator revealed that no change in IS is occurring in the absence of atmosphere. Consequently, the connection with specific adsorbates from ambient atmosphere can clearly be attributed as responsible for the effects on the IS for NW samples. It is known that oxygen adsorbates have a significant impact
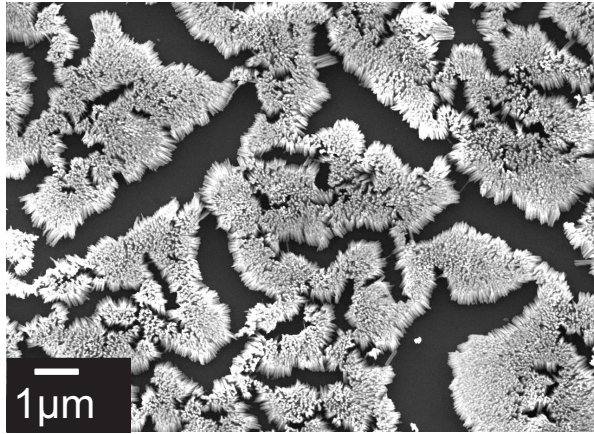
Figure C.2.: Scanning electron microscope image of a conductive GaN NW sample after long term IS measurements at high potentials of both polarities (U_A, U_C $\leq 800\,\text{mV}$).

on the electrical properties of GaN NWs so this is a reasonable candidate [126].

NWs from the resistive class show no indication of degradation of the electro-chemical properties during the measurements whereas conductive NW undergo an irreversible surface reaction that permanently impacts the value of C_S. This is attributed to a oxidation reaction due to the occurring high current flow.

Continuous CV recordings of NWs from the conductive classification while a redox couple is present in the electrolyte reveal a changing of shape after long term measurements (IS recording at both bias polarities up to $800\,\text{mV}$).

At first, the equal height of both current peaks points towards the reversibility of the charge transfer process but after several days the shape of the redox peak smudges as can be seen in Figure C.3.

The shape of the CV–curves after the long measurement period still exhibits a measurable current that is significantly larger compared to the case without redox couple but does not show clear evidence for the previous observed redox peaks. This also points towards a permanent modification at the NW samples surface due to the occurring curentflow.
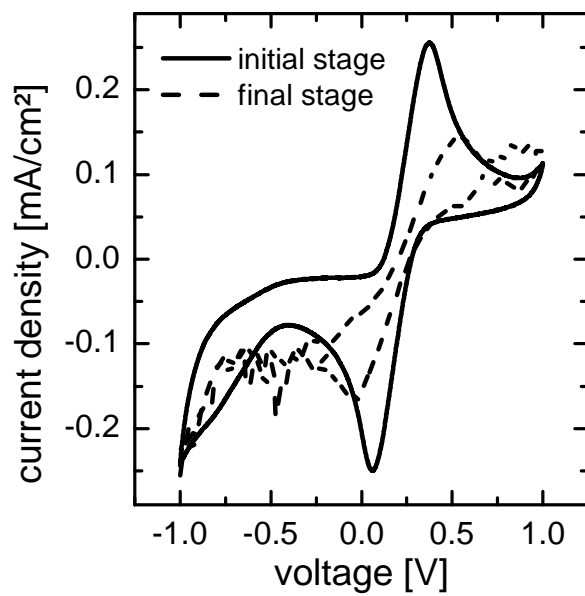
Figure C.3.: Cyclic voltammograms for a conductive NW sample with redox couple Fe^{2+}/Fe^{3+} at a scan rate of $v_{cv} = 100\,mV/s$.

Existing Methods for pH Determination

The backbone of classical pH determination is formed by glass electrodes going back to the first reference [127] following a potentiometric detection principle. Though several alternative measuring principles and optimizations of glass electrodes have been proposed [128] their major drawbacks, namely the problem of miniaturization and the brittleness [129] limit their usability, especially in all food industry related processes, noticeably. To overcome these limitations serious efforts have led to different alternative approaches for pH determination and monitoring. A good overview about the latest developments can be found in [129]. Overall these approaches can be divided according to their sensory readout principle into electrical and optical.

The electrical detection side is dominated by various designs of ion sensitive field effect transistors (ISFETs) which based on Silicon technology were at first reported in 1970 by Bergveld et al. [130]. To overcome the low pH–sensitivity and the electrochemical instability of initially used SiO_2 gate areas different Si_3N_4, Al_2O_3 or Ta_2O_5 have been investigated as gate materials leading to substantial improvement of both stability and sensitivity [131]. More recently, ISFETs based on wide-bandgap semiconductors such as AlGaN/GaN [132] or diamond [133] have been demonstrated to allow for sensitive pH detection combined with improved electrochemical stability. Their greatest advantage lies in the cheap and well developed producibility via standardized photolithographic techniques. However, pH–sensitive devices with electric readout often suffer from signal drift and photocurrent effects as well as from stability issues of the encapsulated electric contacts in chemically aggressive liquids.

The optical pH detection offers a route to overcome such problems. Optical pH sensors based on organic dyes are easy to fabricate when an appropriate dye (or an organic indicator molecules) is adapted to the pH region of interest. It can either be attached to a supporting membrane or surface [134] or free floating. These kinds of sensors offer the advantages of being applicable in low conductive solu-

tions and are easy to fabricate [129]. To our knowledge no organic dye was reported yet, that covers a wide pH range and is immune to photo–bleaching effects. The luminescence properties of uncoated and polymer coated anorganic CdTe nanoparticles (NPs) have been shown to respond to pH variations in the range of pH 4–6 [135]. Frasco et al. [136] used a different approaches of realizing optical pH probes. They achieved pH sensing by capping inorganic NPs with organic ligands. However, as the potential of free NPs cannot be controlled a quantitative analysis of the pH response or the electrochemical definition of a working point is not possible. A further problem is that once the NP are released into a system it is impossible to extract them completely. This in particular is a problem concerning all biological systems due to possible toxicity effects which can not be excluded up to now [137].

In summary it can be stated, that the realization of a stable optical pH sensor for a wide pH range with controllable sensitivity and luminescence intensity is an unsolved issue, so far.

Phosphate Buffered Saline

The buffer *phosphate buffered saline* (PBS) is widely used in bio–electrochemistry. Its ingredients are listed in the table below.

Ingredient	Concentration
$NaCl$	$137\,\text{mM}$
KH_2PO_4	$10\,\text{mM}$
KCl_2	$3\,\text{mM}$
Na_2HPO_4	$2\,\text{mM}$

Ingredients of the standard buffer solution phosphate buffered saline resulting in a concentration of $10\,\text{mM}$.

The adjustment of the solutions pH value was achieved by the addition of either HCl (acidic) or NaOH (basic).

The conductivity of the solution depends strongly on the pH. Table provides an overview about the related conductivities.

pH value	σ [mS/cm]
7 ± 0.1	17.8 ± 0.1
6 ± 0.1	17.9 ± 0.1
5 ± 0.1	18.1 ± 0.2
4 ± 0.1	18.3 ± 0.2
3 ± 0.1	18.4 ± 0.2
2 ± 0.1	21.1 ± 0.3
1 ± 0.1	50.6 ± 0.3

pH values for $10\,\text{mM}$ PBS with the corresponding conductivities at RT.

List of Publications

- **Electrochemical properties of GaN Nanowire electrodes–influence of doping and control by external bias**

  J. Wallys, S. Hoffmann, F. Furtmayr, J. Teubert, and M. Eickhoff;

  Nanotechnology, 2012, 23, 165701

  DOI: 10.1088/0957-4484/23/16/165701

- **Bias-Enhanced Optical pH Response of Group III–Nitride Nanowires**

  J. Wallys, J. Teubert, F. Furtmayr, D. M. Hoffmann, and M. Eickhoff;

  Nano Letters, 2012, 12, 6180 – 6186

  DOI: 10.1021/nl303021v

- **Radical formation at the gallium nitride nanowire / electrolyte interface by photoactivated charge transfer**

  J. M. Philipps, G. M. Müntze, P. Hille, J. Wallys, J. Schörmann, J. Teubert, D. M. Hoffmann, and M. Eickhoff;

  Nanotechnology, 2013, 24, 325701

  DOI: 10.1088/0957-4484/24/32/325701

- **InGaN / GaN quantum dots as optical probes for the electric field at the GaN / electrolyte interface**

  J. Teubert, S. Koslowski, S. Lippert, M. Schäfer, J. Wallys, G. Dimitrakopulos, Th. Kehagias, Ph. Komninou, A. Das and E. Monroy, and M. Eickhoff;

  Journal of Applied Physics, 2013, 114, 074313

  DOI: 10.1063/1.4818624

- **High Precision, Electrochemical Detection of Reversible Binding of Recombinant Proteins on Wide Bad Gap GaN Electrodes Functionalized with Biomembrane Models**

N. Frenkel[1], J. Wallys, J. Teubert, M. Eickhoff, and M. Tanaka[1];

[1] Physical Chemistry of Biosystems, Institute of Physical Chemistry, University of Heidelberg, 69120 Heidelberg, Germany

to be published.

Bibliography

[1] nano.de-report 2011, Bundesministerium für Bildung und Forschung (BMBF), Referat Neue Werkstoffe; Nanotechnologie 53170 Bonn, 2011.

[2] A. Kikuchi, M. Kawai, M. Tada, and K. Kishino, Jpn. J. Appl. Phys. **43**, L1524 (2004).

[3] S. Sakr et al., Appl. Phys. Lett. **99**, 142103 (2011).

[4] B. AlOtaibi et al., Nanotechnology **24**, 175401 (2013).

[5] Y. Iwaki et al., Phys. Stat. Sol. (c) **5**, 2349 (2008).

[6] H. S. Jung et al., ACS Nano **2**, 637 (2008).

[7] N. Sofikiti et al., Mater. Lett. **64**, 1332 (2010).

[8] Y.-T. Lai, A. Ganguly, L.-C. Chen, and K.-H. Chen, Biosens. Bioelectron. **26**, 1688 (2010).

[9] J. Teubert, P. Becker, F. Furtmayr, and M. Eickhoff, Nanotechnology **22**, 275505 (2011).

[10] R. S. Wagner and W. C. Ellis, Appl. Phys. Lett. **4**, 89 (1964).

[11] E. Calleja et al., Mat. Sci. Eng. B **82**, 2 (2001).

[12] E. Calleja et al., J. Cryst. Growth **201-202**, 296 (1999).

[13] E. Calleja et al., Phys. Rev. B **62**, 16826 (2000).

[14] F. Furtmayr et al., J. Appl. Phys. **104**, 034309 (2008).

[15] S. Porowski, J. Cryst. Growth **189**, 153 (1998).

[16] J. O. Bockris and A. K. Reddy, *Modern Electrochemistry 1: Ionics, 2nd Edition*, Springer, 1998.

[17] O. Stern, Zeitschrift für Elektrochemie und Angewandte Pysikalische Chemie **30**, 508 (1924).

[18] C. H. Hamann and W. Vielstich, *Elektrochemie (German Edition)*, Wiley-VCH Verlag GmbH, 4. vollst. überarb. und aktualisierte Auflage. edition, 2005.

[19] S. M. Sze and K. K. Ng, *Physics of semiconductor devices*, Wiley. com, 2006.

[20] O. Brandt et al., Papers from the 29th Conference on the Physics and Chemistry of Semiconductor Interfaces **20**, 1626 (2002).

[21] C. Adelmann et al., Appl. Phys. Lett. **82**, 4154 (2003).

[22] F. Furtmayr et al., Phys. Rev. B **84**, 205303 (2011).

[23] O. Weidemann et al., Appl. Phys. Lett. **94**, 113108 (2009).

[24] J. Teubert et al., J. Appl. Phys. **114**, 074313 (2013).

[25] S. Dhesi et al., Phys. Rev. B **56**, 10271 (1997).

[26] H. Morkoc, *Handbook of Nitride Semiconductors and Devices.*, volume 3, Wiley-VCH, 2009.

[27] I. Vurgaftman and J. R. Meyer, J. Appl. Phys. **94**, 3675 (2003).

[28] C. A. Koval and J. N. Howard, Chem. Rev. **92**, 411 (1992).

[29] J. O. Bockris, A. K. Reddy, and M. E. Gamboa-Aldeco, *Modern Electrochemistry 2A: Fundamentals of Electrodics*, Springer, 2008.

[30] R. Calarco et al., Nano Lett. **5**, 981 (2005).

[31] M. Kocan, A. Rizzi, H. Lüth, S. Keller, and U. Mishra, Phys. Stat. Sol. (b) **234**, 773 (2002).

[32] F. Furtmayr et al., J. Appl. Phys. **104**, 074309 (2008).

[33] J. Schörmann et al., J. Appl. Phys. **114**, 103505 (2013).

[34] W. Shan et al., Phys. Rev. B **54**, 16369 (1996).

[35] D. Volm et al., Phys. Rev. B **53**, 16543 (1996).

[36] M. A. Reshchikov and H. Morkoc, J. Appl. Phys. **97**, 061301 (2005).

[37] J. S. Colton et al., Appl. Phys. Lett. **75**, 3273 (1999).

[38] U. Kaufmann et al., Appl. Phys. Lett. **72**, 1326 (1998).

[39] R. Stepniewski et al., Phys. Stat. Sol. (b) **210**, 373 (1998).

[40] M. A. Reshchikov, G.-C. Yi, and B. W. Wessels, Phys. Rev. B **59**, 13176 (1999).

[41] J. L. Lyons, A. Janotti, and C. G. Van de Walle, Phys. Rev. Lett. **108** (2012).

[42] F. Furtmayr, *Nitride Nanowire Heterostructures*, PhD thesis, Walter Schottky Institut, Technische Universität München, 2013.

[43] J. I. Pankove, J. Appl. Phys. **47**, 5387 (1976).

[44] I. Shalish et al., Appl. Phys. Lett. **77**, 987 (2000).

[45] H. Yang, T. Lin, and Y. Chen, Phys. Rev. B **62**, 12593 (2000).

[46] J. L. Lyons, A. Janotti, and C. G. Van de Walle, Appl. Phys. Lett. **97**, 152108 (2010).

[47] L. Polenta et al., ACS Nano **2**, 287 (2008).

[48] R. Crouch, W. Debnam, and A. Fripp, J. Mater. Sci. **13**, 2358 (1978).

[49] H. Gerischer, Z. Physik. Chem. **26**, 223 und 325 (1960).

[50] H. Gerischer, Z. Physik. Chem. **27**, 48 (1961).

[51] R. Memming, *Semiconductor electrochemistry*, Wiley. com, 2008.

[52] R. A. Marcus, J. Chem. Phys. **24**, 966 (1956).

[53] S. R. Morrison, *Electrochemistry at semiconductor and oxidized metal electrodes*, Plenum Press, 1980.

[54] R. Gomer and G. Tryson, J. Chem. Phys. **66**, 4413 (1977).

[55] E. Koetz, H. Neff, and K. Mueller, J. Electroanal. Chem. **215**, 331 (1986).

[56] F. Lohmann, Z. Naturforsch. Pt. A **A 22**, 843 (1967).

[57] J. D. Beach, R. T. Collins, and J. A. Turner, J. Electrochem. Soc. **150**, A899 (2003).

[58] J. Wallys, J. Teubert, F. Furtmayr, D. M. Hofmann, and M. Eickhoff, Nano Lett. **12**, 6180 (2012).

[59] P. Wasserscheid and T. Welton, *Ionic Liquids in Synthesis*, Wiley-VCH, 2002.

[60] G. Mamantov, Molten salt electrolytes in secondary batteries, in *Materials for Advanced Batteries*, pages 111–122, Springer, 1980.

[61] Iolitec, Emim bta 1-ethyl-3-methylimidazolium bis trifluoromethylsulfonyl imide, Technical report, Iolitec, 2013.

[62] S. Rondinini, Anal. Bioanal. Chem. **374**, 813 (2002).

[63] R. Dalven, *Introduction to Applied Solid State Physics: Topics in the Applications of Semiconductors, Superconductors, Ferromagnetism, and the Nonlinear Optical Properties of Solids*, Springer, 1990.

[64] M. L. Rosenbluth and N. S. Lewis, J. Phys. Chem. **93**, 3735 (1989).

[65] D. E. Yates, S. Levine, and T. W. Healy, J. Chem. Soc. Farad. T. 1 **70**, 1807 (1974).

[66] G. Steinhoff, O. Purrucker, M. Tanaka, M. Stutzmann, and M. Eickhoff, Adv. Funct. Mater. **13**, 841 (2003).

[67] O. Weidemann et al., Appl. Phys. Lett. **83**, 773 (2003).

[68] M. J. Madou and S. R. Morrison, *Chemical Sensing with Solid State Devices*, Academic Press, 1989.

[69] Y. Xu and M. A. A. Schoonen, Am. Mineral. **85**, 543 (2000).

[70] M. Bayer, C. Uhl, and P. Vogl, J. Appl. Phys. **97**, 033703 (2005).

[71] L. Bousse, S. Mostarshed, B. van der Schoot, and N. de Rooij, Sensor. Actuat. B-Chem. **17**, 157 (1994).

[72] A. Hickling, Trans. Faraday Soc. **33**, 1540 (1937).

[73] A. Hickling, Trans. Faraday Soc. **38**, 27 (1942).

[74] H. Gerischer, J. Electrochem. Soc. **113**, 1174 (1966).

[75] H. Gerischer, J. Electrochem. Soc. **125**, 218C (1978).

[76] M. de la Mata et al., Nano Lett. **12**, 2579 (2012).

[77] J. Neugebauer and C. G. Van de Walle, Phys. Rev. B **50**, 8067 (1994).

[78] M. Chemla et al., Electrochim. Acta **51**, 665 (2005).

[79] M. Petrova, M. Bojinov, S. Zanna, and P. Marcus, Electrochim. Acta **56**, 7899 (2011).

[80] R. P. Janek, W. R. Fawcett, and A. Ulman, Langmuir **14**, 3011 (1998).

[81] O. Purrucker, H. Hillebrandt, K. Adlkofer, and M. Tanaka, Electrochim. Acta. **47**, 791 (2001).

[82] V. Horvat-Radošević and K. Kvastek, J. Electroanal. Chem. **631**, 10 (2009).

[83] H.-Y. Chen et al., Appl. Phys. Lett. **95**, 143123 (2009).

[84] E. Sackmann, Science-AAAS-Weekly Paper Edition **271**, 43 (1996).

[85] S. Liu, Phys. Rev. Lett. **55**, 529 (1985).

[86] J. Wallys, S. Hoffmann, F. Furtmayr, J. Teubert, and M. Eickhoff, Nanotechnology **23**, 165701 (2012).

[87] J. R. Macdonald and W. R. Kenan, *Impedance Spectroscopy: Emphasizing Solid Materials and Systems*, Wiley-Interscience, 1987.

[88] D. Ende and K.-M. Mangold, Chem. unserer Zeit **27**, 134 (1993).

[89] U. Rammelt and G. Reinhard, Electrochim. Acta. **35**, 1045 (1990).

[90] G. Steinhoff, *Group III–Nitrides for Bio– and Electrochemical Sensors*, PhD thesis, Walter Schottky Institut, 2008.

[91] C. H. Hsu and F. Mansfeld, Corrosion **57**, 747 (2001).

[92] J. E. B. Randles, T. Faraday. Soc. **44**, 327 (1948).

[93] private communication Nastaran Krawczyk.

[94] Y. C. Yeo et al., IEEE. J. EDL **21**, 540 (2000).

[95] C. Pfüller et al., Phys. Rev. B **82**, 045320 (2010).

[96] J. Arbiol et al., Nanotechnology **20**, 145704 (2009).

[97] V. I. Lobyshev, R. E. Shikhlinskaya, and B. D. Ryzhikov, J. Mol. Liq. **82**, 73 (1999).

[98] G. Steinhoff et al., Appl. Phys. Lett. **83**, 177 (2003).

[99] S. S. Kocha et al., J. Electrochem. Soc. **142**, L238 (1995).

[100] D. B. Wittry and D. F. Kyser, J. Appl. Phys. **38**, 375 (1967).

[101] R. E. Hetrick and K. F. Yeung, J. Appl. Phys. **42**, 2882 (1971).

[102] U. Langmann, Appl. Phys. **1**, 219 (1973).

[103] K. Mettler, Appl. Phys. **12**, 75 (1977).

[104] G. Chmiel and H. Gerischer, J. Phys. Chem.-US **94**, 1612 (1990).

[105] B. Smandek, G. Chmiel, and H. Gerischer, Berich. Bunsen. Gesell. **93**, 1094 (1989).

[106] T. Richter, H. L. R. Meijers, R. Calarco, and M. Marso, Nano Lett. **8**, 3056 (2008), PMID: 18687013.

[107] K. Izutsu, *Electrochemistry in Nonaqueous Solutions*, Wiley-VCH, 2009.

[108] J. M. Philipps et al., Nanotechnology **24**, 325701 (2013).

[109] H. Obloh et al., J. Cryst. Growth **195**, 270 (1998).

[110] R. Dingle and M. Ilegems, Solid State Commun. **9**, 175 (1971).

[111] W. H. Baumann et al., Sensor. Actuat. B-Chem. **55**, 77 (1999).

[112] K. O. Honikel and C. Fischer, J. Food Sci. **42**, 1633 (1977).

[113] A. Offenhäusser, C. Sprössler, M. Matsuzawa, and W. Knoll, Biosens. Bioelectron. **12**, 819 (1997).

[114] W. Torbicz, D. G. Pijanowska, and M. Dawgul, Front. Med. Biol. Eng. **10**, 139 (2000).

[115] H. Tyagi, A. Kushwaha, A. Kumar, and M. Aslam, Int. J. Nanosci. **10**, 857 (2011).

[116] Y. Lin et al., Chem. Phys. Lett. **507**, 209 (2011).

[117] D. Hofmann, Untersuchung der Funtionalität kovalent immobilisierter Fnzyme auf Halbleiteroberflächen durch optische Extinktionsmessungen, Bachelor's thesis, Justus-Liebig-Universität Gießen, 2011.

[118] C. Heinz, Analysis of enzyme-modified group III–nitiride surfaces, Bachelor's thesis, Justus-Liebig-Universität Gießen, 2011.

[119] S. Koslowski, Optical analysis of enzyme activity after immobilisation on gan layers and structures, Master's thesis, Justus-Liebig-Universität Gießen, 2012.

[120] S. Caras and J. Janata, Anal. Chem. **52**, 1935 (1980).

[121] T. Kehagias et al., Nanotechnology **24**, 435702 (2013).

[122] P. G. Moses and C. G. V. de Walle, Appl. Phys. Lett. **96**, 021908 (2010).

[123] G. Tourbot et al., Nanotechnology **22**, 075601 (2011).

[124] G. Tourbot et al., Nanotechnology **23**, 135703 (2012).

[125] A. Pakes et al., J. Mater. Sci. **38**, 343 (2003).

[126] R. S. Chen, C. Y. Lu, K. H. Chen, and L. C. Chen, Appl. Phys. Lett. **95**, 233119 (2009).

[127] M. Cremer, Z. Biol.-Munich **47**, 562 (1906).

[128] C. Cheng et al., Electrochim. Acta. **56**, 9883 (2011).

[129] Y. Miao, J. Chen, and K. Fang, J. Biochem. Bioph. Meth. **63**, 1 (2005).

[130] P. Bergveld, IEEE T. Bio-Med. Eng. **17**, 70 (1970).

[131] P. Bergveld, Sensor. Actuat. B-Chem. **88**, 1 (2003).

[132] G. Steinhoff et al., Adv. Solid State Phys. **45**, 363 (2005).

[133] K.-S. Song et al., Phys. Rev. E **74**, 041919 (2006).

[134] G. J. Mohr and O. S. Wolfbeis, Anal. Chim. Acta. **292**, 41 (1994).

[135] A. S. Susha, A. M. Javier, W. J. Parak, and A. L. Rogach, Colloid. Surface. A **281**, 40 (2006).

[136] M. F. Frasco and N. Chaniotakis, Sensors-Basel **9**, 7266 (2009).

[137] H.-R. Paur et al., J. Aerosol Sci. **42**, 668 (2011).

Acknowledgements / Danksagung

Auf den letzten Seiten möchte ich mich bei all den lieben Menschen bedanken, die mich mit Rat und Tat bei der Entstehung dieser Arbeit unterstützt haben. Im Besonderen bedanke ich mich bei:

- Prof. Dr. Martin Eickhoff, meinem Doktorvater, für die Gelegenheit, die Arbeitsgruppe mitaufzubauen. Außerdem vielen Dank für deine wertvolle Unterstützung bei Experimenten und während des Schreibprozesses, für deine stets motivierende Haltung sowie für die Möglichkeit, meine Arbeit auch auf internationaler Bühne präsentieren zu können.

- Dr. Jörg Schörmann für die vielen kleinen Hilfestellungen und die Einführung in die Welt der Ultrahochvakuumstechnik. Die MBE in ihren Kindertagen mit dir zu betreuen hat mir sehr großen Spaß bereitet. Insbesondere danke ich dir für die schöne gemeinsame Zeit während und nach der Arbeit.

- Dr. Jörg Teubert für die freundschaftliche Büroatmosphäre, in der immer Zeit war für Gespräche zu wissenschaftlichen und nicht wissenschaftlichen Themen. Außerdem bedanke ich mich für die sehr geduldige Hilfestellung beim Erarbeiten der Veröffentlichungen sowie bei der Korrektur dieser Dissertation.

- Markus Schäfer, Sascha Hoffmann und Pascal Becker, dem Team der ersten Stunde, für eure große Hilfsbereitschaft im Reinraum, im E–chemie Labor, bei PL–Angelegenheiten und beim Russischen. Danke auch für eure Inspiration und Begeisterung für die Dinge rechts und links des Wegesrandes.

- Thomas Wasem für dein Engagement und deine Bereitschaft, dich auf das Abenteuer Elektrochemie einzulassen. Ohne die fruchtbaren Konstruktionsdebatten wären so manche Ideen nicht realisiert worden und keine der gefertigten Messzellen würde so gut funktionieren wie sie es tut.

- Den Master–, Bachelor– und Werksstudenten Daniel Hofmann, Oliver Brusdeilins, Christian Heinz, Sebastian Koslowski und Sara Lippert, die mich durch ihr großes Interesse und Engagement bei meiner Arbeit tatkräftig unterstützt haben. Viele Experimente wären ohne euer Zutun nicht realisierbar gewesen.

- Thomas Nimmerfroh und Rainer Weiss, stellvertretend für die beiden Werkstätten, für die gekonnte Umsetzung der "großen" Konstruktionen sowie für die zahllosen, aber unendlich wichtigen, kleineren, schnell erledigten Arbeiten.

- Helge Höchsmann, Renate Fuchs und Hans Peter Jorde, stellvertretend für alle, die jederzeit dafür sorgen, dass die wichtigen Dinge neben dem physikalischen Betrieb funktionieren und dabei immer auch die Zeit für ein freundliches Gespräch finden.

- Norbert Kurmann, Reinhard Rüdiger und Karl Lautenbach, für die Hilfe bei der Erstellung der verschiedenen Versuchsaufbauten.

- Krista Lein und Bozena Wirsbitzki für die unzähligen Male der spontanen Hilfsbereitschaft, wenn es darum ging, uns Physiker mit Material, Gerätschaften oder Know–How aus dem IFZ zu unterstützen.

- Florian Furtmayr für das Herstellen der Nanodrähte.

- Andreas Rühl und Florian Gather für die spontane Hilfe beim Formulieren eines funktionstüchtigen numerischen Fitalgorithmus zum Fitten der Kalibrationskurven.

- Den aktiven und ehemaligen Mitgliedern der Arbeitsgruppe Eickhoff für das freundschaftliche Arbeitsklima und die immer interessanten Mittagspausengespräche.

- Allen Freunden und Kollegen aus meiner Zeit im I. Physikalischen Institut für die herzliche Aufnahme in eure Reihen und die gute Zusammenarbeit. Außerdem ein großes Dankeschön an alle Mitorganisatoren der PhysikCups (Achim K. , Andreas R. , Benedikt K. , Björn B. , Christian W. , Clemens G. , Jan, Mathias I. , Marcel D. , Markus P. , Max E. , Melanie P. , Sascha H. , Steffanie B. , Tobias E. und Wayne L.).

- Meiner Familie für die vielen Jahre der Unterstützung, wann immer sie nötig war, und die Ablenkung, wenn sonst nichts mehr geholfen hat.

- Friederike für die Aufmunterungen und Anstichelungen zur rechten Zeit und vor allem für die fortwährende Unterstützung während der Promotionszeit.

Erklärung

Ich erkläre:

Ich habe die vorgelegte Dissertation selbständig und ohne unerlaubte fremde Hilfe und nur mit den Hilfen angefertigt, die ich in der Dissertation angegeben habe. Alle Textstellen, die wörtlich oder sinngemäß aus veröffentlichten Schriften entnommen sind, und alle Angaben, die auf mündlichen Auskünften beruhen, sind als solche kenntlich gemacht. Bei den von mir durchgeführten und in der Dissertation erwähnten Untersuchungen habe ich die Grundsätze guter wissenschaftlicher Praxis, wie sie in der Satzung der Justus–Liebig–Universität Gießen zur Sicherung guter wissenschaftlicher Praxis niedergelegt sind, eingehalten.

Jens Wallys

Gießen, den 27.01.2014